A NUMERICAL INVESTIGATION OF BUBBLE-INDUCED LIQUID AGITATION AND BUBBLE DYNAMICS IN STRATIFIED FLOWS

by

Maathangi Ganesh

A Dissertation

Submitted to the Faculty of Purdue University

In Partial Fulfillment of the Requirements for the degree of

Doctor of Philosophy

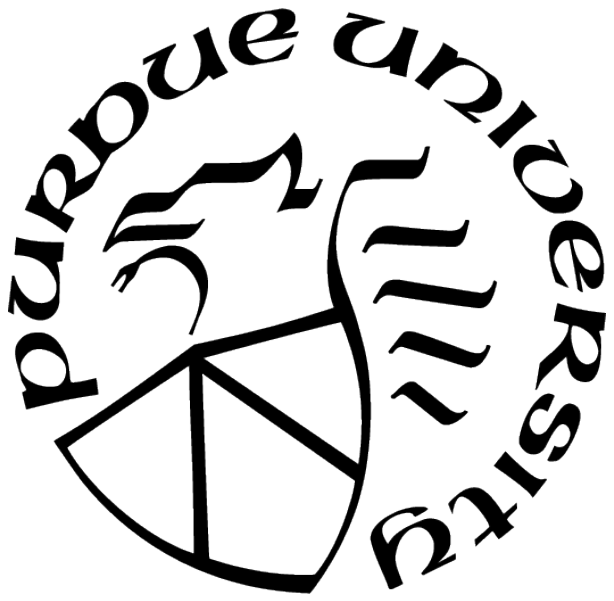

School of Mechanical Engineering

West Lafayette, Indiana

May 2021

THE PURDUE UNIVERSITY GRADUATE SCHOOL
STATEMENT OF COMMITTEE APPROVAL

Dr. Sadegh Dabiri, Chair

Department of Agricultural and Biological Engineering, and School of Mechanical Engineering

Dr. Ivan C. Christov

School of Mechanical Engineering

Dr. Martin A. Lopez-De-Bertodano

School of Nuclear Engineering

Dr. Jun Chen

School of Mechanical Engineering

Approved by:

Dr. Nicole Key

ACKNOWLEDGMENTS

I would like to acknowledge my advisor Dr. Sadegh Dabiri for the important role he plays in my PhD studies. He has been patient through my ups and downs and provides constant support. He has inspired me to think critically and act creatively in the fluid dynamics field.

I would also like to thank my committee members Dr. Ivan Christov, Dr. Jun Chen and Dr. Martin Lopez-De-Bertodano for kindly agreeing to be in my committee and taking time to guide me through my PhD journey. I want to thank all the professors at Purdue whose courses I have been a part of, who have helped expand my knowledge and skills. Special thanks goes to Dr. Carlo Scalo for offering intriguing courses and having an impact on me as a researcher.

I am grateful to all my colleagues and friends for providing constructive feedback and a constant support system through my graduate studies.

Finally I would like to offer my sincerest thanks to my parents, Sudha and Ganesh, my sister, Aishwarya, and my partner, Raghul, for being a pillar of support through my life.

TABLE OF CONTENTS

LIST OF TABLES

LIST OF FIGURES

LIST OF SYMBOLS

ρ	density
v, u	velocity
p	pressure
T	temperature
T_m	temperature perturbation from linearity
d	bubble diameter
μ	dynamic viscosity
ν	kinematic viscosity
g	gravity
σ	interfacial tension coefficient
$\mathbf{n}$	normal to the interface
k	thermal conductivity
C_p	heat capacity
β	density gradient
V_T	total volume of domain
N	buoyancy frequency
N_b	number of bubbles
D	diffusivity of stratifying agent
κ	thermal diffusivity
Re	Reynolds number
Eo	Eotvos number
Ar	Archimedes number
Bo	Bond number
Pr	Prandtl number
Ra	Rayleigh number
Nu	Nusselt number
Fr	Froude number
α	void fraction

γ	thermal expansion coefficient
Φ	color function
C	volume fraction
κ'	twice the mean curvature
δ^b	delta function
w	separation between rigid walls
V_0	rise velocity of isolated bubble
K_ρ	diapycnal eddy diffusivity
COX	Cox number
Γ	mixing efficiency
E	strain rate tensor
ϵ	viscous dissipation
χ	bubble aspect ratio
C_D	drag coefficient
x_b	location of bubble center of mass
C_{AM}	added mass coefficient
$< \cdot >$	Ensemble average
f, l	subscript fluid, liquid
b	subscript bubble
0	subscript initial
h, c	subscript hot, cold
(i)	superscript i$^t h$ bubble
$'$	superscript fluctuation
$*$	superscript non-dimensionalized

ABSTRACT

Mixing of stratified fluids due to motion of bubble swarms can happen through two major mechanisms. The first is the capture and transport of heavier liquid into the lighter layers by the bubble wake. The second is the mixing due to turbulent dispersion. Stratification also affects bubble dynamics in various ways, namely by reducing the horizontal and vertical bubble fluctuations and extent, altering the drag experienced by rising bubbles, and changing the wake dynamics. The objective of this study is to understand these explained phenomena by decoupling their effects from each other and studying them individually. CFD offers powerful capabilities to achieve the decoupling and perform in-depth analysis of the fluid flow.

Firstly, the study of mixing induced in stratified fluids by bubbly flow in a Hele-Shaw Cell will be performed. Simulations are run for a range of void fractions and Froude numbers. The confinement prevents turbulence production, and mixing occurs primarily due to transport of colder liquid into the hotter layers by the bubble wake. Bubbles move in a zigzag motion attributed to the periodic vortex shedding in their wake. We report the formation of horizontal clusters and establish a direct correlation between the size of clusters and the rise velocity of the bubbles. We report an increase in the buoyancy flux across the isopycnals as the void fraction increases. The fraction of energy production due to the buoyancy flux increases with the strength of stratification, giving rise to a higher mixing efficiency. At the same time, cross isopycnal diffusion is higher at weaker stratification strengths.

Subsequently, direct numerical simulations of up to 146 bubbles rising in unbounded stratified fluids are performed. Both the bubble dynamics and destratification effects caused by the bubble motion are analyzed. The importance of bubble deformability and bubble Reynolds numbers on the induced background mixing are studied by varying the *Eötvös* number in the range 1.55 to 4.95 and Reynolds number in the range 25 to 200. Highly deformable, high Reynolds number bubbles undergo path instabilities and give rise to higher levels of mixing. Liquid and bubble velocity fluctuations and pseudo-turbulence caused by the bubble motion in the unconfined setting are examined and are seen to play an important role in mixing statistics. An increase in turbulent kinetic energy (TKE) levels with void

fraction is noted. TKE levels are seen to decrease slightly as the stratification strength is increased, indicating increasing stability and resistance to destratification. Regardless of the stratification strength, a kinetic energy spectrum slope value between $-3 \sim -3.25$ is reported depending on Reynolds number. The dependence of mixing parameters on the void-fraction of bubbles and stratification strength of the liquid is also presented.

Next, the study of buoyancy driven motion of a single air bubble in stratified liquid is undertaken. A range of parameters including Froude number, Reynolds number and Bond number are explored. The Reynolds and Bond numbers will be maintained at values where the bubble motion and wake can be assumed to be axisymmetric. Wake dynamics and drift-volumes associated with the bubble rising in the stratified fluid are analyzed. The presence of secondary and tertiary vortices, which are alternating in direction, in the wake of the bubble due to the negative buoyant force experienced by the isopycnals is reported. The isopycnals oscillate before coming back to their stable state and the frequency of oscillations increases with stratification strength. The dependence of drag coefficient, determined by an unsteady force balance, and steady state bubble velocities, on the above mentioned parameters are studied. Analysis of bubble rise in partial stratification reveals the differences between homogeneous and stratified mediums.

Since most stratified bubbly flows occur near the free surface, an attempt is made at modeling the bubble rise up-to the free surface and subsequent bubble bursting. A brief study of in-line bubble coalescence is also attempted and potential future work for bubbly flows with topological changes is discussed.

1. INTRODUCTION

The rising motion of bubbles occurs ubiquitously in nature. They are commonly found in natural, chemical and biological processes. The fact that the fluctuations created by bubble motion can help in mixing the background fluid without external mechanical agitation has significant applications. Some examples include chemical reactors and heat exchangers consisting of bubble columns, injection of bubbles for homogenization of liquid metal bath in secondary steelmaking process and applications in metallurgy and food processing industry. Rising bubbles are also prone to wake-induced oscillations, which can contribute to efficient mixing. Furthermore, we need to understand how mixing and agitation are affected by temperature or salt stratification in liquids since we encounter stratified fluids like oceans and lakes more often than not in nature. Bubble plume mixers are used for destratification of temperature stratified lakes and reservoirs, in order to preserve freshwater. The destratification also improves the chemical quality of water. Bubble plumes are also used as bubble curtains for containment of oil spills in oceans, which are inherently temperature stratified. Besides the numerous applications of studying mixing in stratified fluids, the bubble dynamics is also influenced by the stratification. The vertical motion of bubbles rising in a stratified environment, with a background density gradient β, depends on a variety of factors including Reynolds number $Re = \rho_l v_b d/\mu$, Eotvos number $Eo = (\rho_l - \rho_g) g d^2/\sigma$ and Froude number, $Fr = v_b/(Nd)$, where $N = \sqrt{\beta g/\rho_\circ}$, d, σ, N_b, V_T are the buoyancy frequency, bubble diameter, surface tension, number of bubbles and total domain volume, respectively. ρ, μ, g, v_b are the density, viscosity, gravity and bubble velocity calculated apriori, respectively. Void fraction $\alpha = N_b \dfrac{\pi d^3/6}{V_T}$, also plays a role through bubble interactions.

Confined bubbly flow is used in the cooling process in microelectronic devices [1]. Gas-liquid flow in narrow channels is also important in nuclear industries for cooling purposes [2]. Many heat exchangers and chemical reactors involve bubble columns [3]. Having bubbly flow is useful in causing liquid agitation and consequently, liquid mixing without the need for any moving mechanical parts and at relatively low Reynolds number.

Although the number of studies involving bubble motion and bubble induced turbulence have gained tremendous significance, we find that there are still not many studies focusing

on characterizing the mixing mechanisms in stratified fluids due to the bubble motion in confined and unconfined settings. The confined case is of importance because we are able to isolate the effects that bubble wake transport has on mixing. This would otherwise be impossible in an unconfined domain where mixing happens both due to transport by bubble wake as well as bubble induced turbulent fluctuations. Although stratified flows are widely encountered in nature, there existed a notion that the scale ($\rho_l/\beta \sim O(m)$) in which stratification varied in lakes and oceans cannot affect bubbles of millimetric and lesser size. This was proved to be incorrect [4], where it was established that the appropriate lengthscale to determine whether motion is affected by stratification is $L_s = (\mu_l D/\beta g)^{1/4}$, where μ_l, D, β and g are the liquid viscosity, diffusivity of stratifying agent, density gradient and gravitational acceleration, respectively. In fact, we not only find that the bubble motion is affected by stratification, but also the background velocity fluctuations, thermal mixing and liquid energetics are affected by the bubble motion through varying degrees of stratification. Apart from mixing properties, we find that there is a lack of comprehensive literature on bubble motion characteristics spanning wide range of Reynolds, Eotvos and Froude numbers in stratified fluids, particularly near the free surface. Valuable information about the bubble dynamics can be obtained by considering a single rising bubble as evidenced by studies of single rising drop [5] and falling sphere [6] in stratified fluids. Topological changes in bubbles could also significantly alter the bubble and liquid dynamics and is an important factor to consider in bubbly flows.

2. OBJECTIVE AND SCOPE

Our objective is to investigate the bubble and liquid dynamics in the rise of bubbles in temperature stratified Newtonian fluids. Computational fluid dynamics is used to construct the different geometries and boundaries in order to solve for the fluid flow. The computational technique allows us to isolate the different coupled effects between stratification and bubble motion, which can then be individually studied. We achieve this by investigating mixing properties when bubbles rise near wall and in unbounded settings. We also study the effect of stratification on the motion of a single bubble. The three studies undertaken to address our objectives are:

1. Induced mixing by rising bubbles in stratified fluids in a Hele-shaw Cell

a. Mixing occurring primarily due to transport by bubble wake is analyzed by looking at liquid fluctuations and mixing parameters like diapycnal eddy diffusivity, mixing efficiency and Cox number.

b. Bubble dynamics will be investigated using various physical parameters including bubble velocity fluctuations and autocorrelation, path instabilities and wake flow.

c. A parametric study in the void fraction - Froude number space is performed.

2. Bubble induced liquid dynamics in unbounded stratified fluids

a. Liquid dynamics including mixing, TKE levels, liquid velocity fluctuations and spatial/ temporal correlations and flow visualization will be analyzed.

b. Bubble dispersion, microstructure and bubble velocity fluctuations will be computed and used to interpret the mixing results.

c. Wide range of parameters will be explored, including void fraction ($3.5\% \sim 8\%$), Froude ($10 \sim 28$), Reynolds ($25 \sim 200$) and Eotvos numbers($1.5 \sim 5$).

3. Transient single bubble dynamics in stably stratified fluids

a. Terminal velocities, bubble shapes and drag estimation on a single air bubble rising in stratified fluids are reported

b. Wake dynamics, including drift volumes and presence of any secondary and tertiary vortices due to negative buoyant force in stratified fluids is studied.

c. A comprehensive parametric study in the $Re - Eo - Fr$ space is performed.

d. Rising bubble in partial stratification is analyzed

4. Topological Changes

a. A preliminary study of bubble rising in a stratified fluid and merging with the free surface is performed.

b. Importance of bubble coalescence/break-up is discussed along with a preliminary simulation to validate in-line bubble coalescence.

3. GOVERNING EQUATIONS

We perform fully resolved direct numerical simulations in stratified fluids. Our problem of interest is solved numerically through the continuity, momentum and energy conservation equations. We use the Boussinesq approximation and ignore density differences due to stratification except in the buoyancy term. The equations are as follows:

$$\rho_\circ \frac{D\mathbf{u}}{Dt} = -\nabla p + \Delta\rho\mathbf{g} + \nabla \cdot \mu(\nabla\mathbf{u} + (\nabla\mathbf{u})^T) + f_\sigma, \tag{3.1}$$

$$\nabla \cdot \mathbf{u} = 0, \tag{3.2}$$

$$\rho_\circ C_p \frac{DT}{Dt} = \nabla \cdot (k\nabla T). \tag{3.3}$$

The viscosity, μ and density, ρ_0, are defined as $\mu = \mu_b(1-\Phi) + \mu_l\Phi$ and $\rho_0 = \rho_b(1-\Phi) + \rho_l\Phi$, respectively. Subscripts b and l refer to the bubble and the liquid phase respectively. Φ, the color function, is defined as 1 in the liquid phase and 0 inside the bubble. The color function is also used to update the thermal conductivity, k and also the value of $\rho_\circ C_p$ similar to how μ, ρ_0 are defined. The second term on the right hand side of equation 3.1 includes the stratification effect. Here ρ is defined as $\rho = \rho_\circ(1-\gamma\Delta T)$, where γ is the thermal expansion coefficient and ΔT is the temperature difference with a reference temperature. A constant linear temperature gradient, $T_0 = \frac{dT}{dx}x$, is imposed at $t = 0$ which translates to a linear density gradient. The density at the bottom of the domain is $\rho = \rho_\circ$ and it decreases linearly upwards initially. In case of periodicity in the vertical direction (as in the case of the confined and unconfined studies), the quantity $\overline{\rho}\mathbf{g}$ is subtracted from $\rho\mathbf{g}$ to so that there is no net flow through the domain and the net force on the domain is 0. This gives $\Delta\rho = (\rho - \overline{\rho})$. This is done to ensure that the domain is not accelerating downward. Here, $\overline{\rho}$ is the mean density of the entire computational volume. If there are walls at the top and the bottom (as in the case of the study of single bubble dynamics), $\Delta\rho$ will simply be

ρ. The term f_σ indicates the surface tension forces between the two phases and its calculation is explained in chapter 4.

4. NUMERICAL FRAMEWORK

4.1 Confined and unconfined studies

The governing equations are solved by a finite volume/front tracking method which was initially introduced by Unverdi and Tryggvason [7] and improved by Tryggvason et. al [8]. This is a one-fluid approach to solve the Navier-Stokes equations where a single set of equations is solved in the dispersed and the continuous phase. The equations are solved on a staggered Eulerian grid. The bubbles are represented by "fronts", which are a set of interconnected points formed by an unstructured mesh. Both the Eulerian and front grid are shown in figure 4.1. The front is translated by interpolating the fluid velocity from the Eulerian onto the front grid. The surface tension and color function are computed on the front and interpolated back on to the structured grid. With this

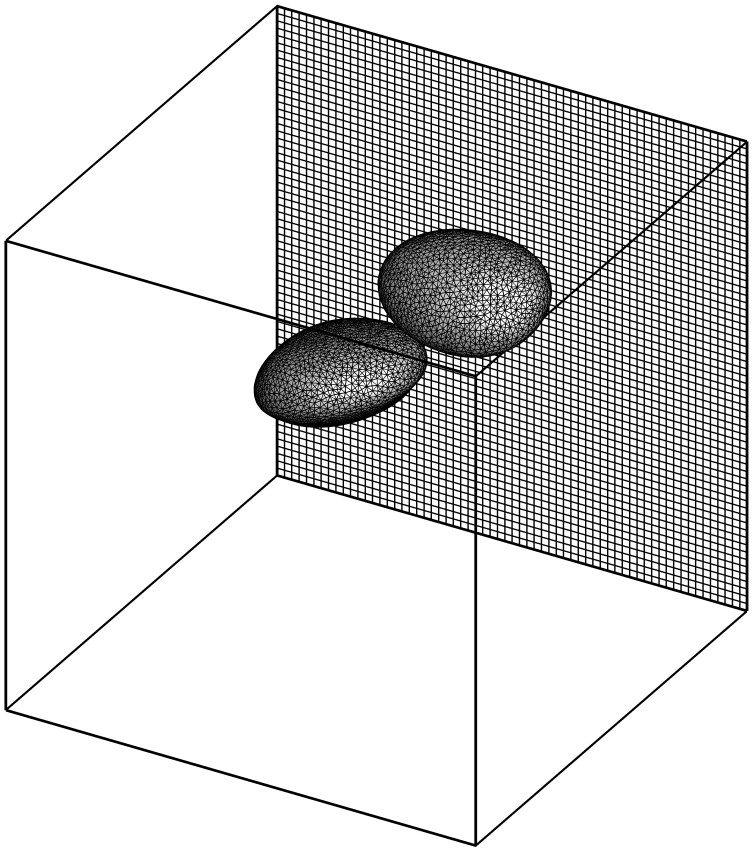

Figure 4.1. Eulerian and front grid

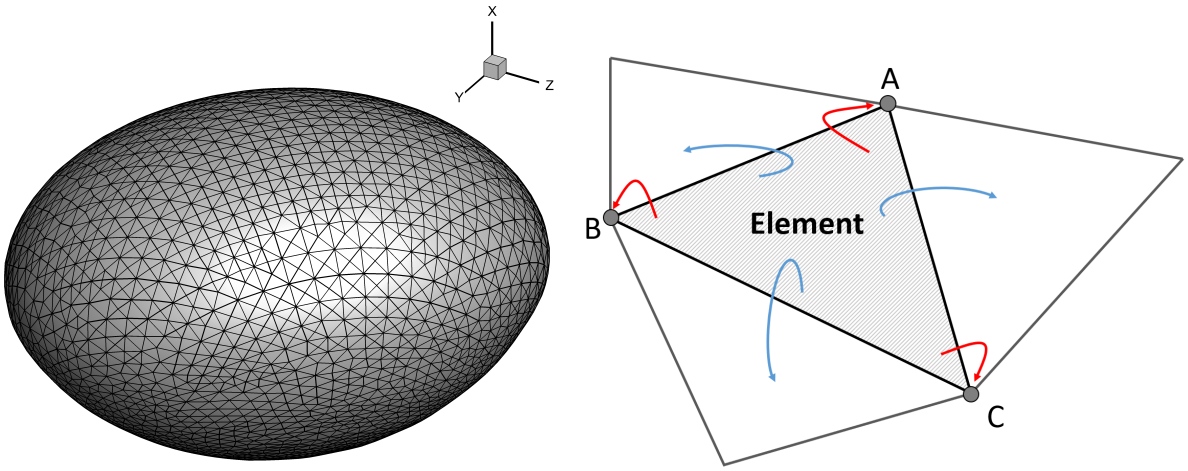

(a) (b)

Figure 4.2. (a) Interface represented as a front (b) Structure of the 3D front.

approach, we are mostly interested in the statistically steady state flow. The range of parameters we would like to study does not include cases of bubble coalescence or breakup.

The projection method [9] is used to enforce continuity. This gives rise to an explicit Poisson Equation for the pressure, which is solved using the HYPRE library [10]. The third order QUICK (Quadratic Upstream Interpolation for Convective Kinetics) [11] scheme is used for the momentum convection terms, while the second-order central differencing scheme is used for diffusive terms. A second-order Runge-Kutta scheme is used for time advancement.

4.1.1 Front Tracking

In the front tracking method, the interface is represented by a set of connected marker points that are moved by the fluid as shown in figure 4.2. In this method, we use two grids: (i) Eulerian grid, where the governing equations of the fluid flow are solved; (ii) Unstructured (front) grid that tracks the interface (figure 4.1). The front grid is used to track the interface accurately and also to apply surface tension forces.

The structure of the three-dimensional front is shown in figure 4.2b. The triangular element on the front, ABC, along with the adjacent elements are shown. Each element carries all the information about the front, including pointers to the corner points (red arrows) and to the adjacent elements sharing an edge (blue arrows).

Since we deal with deformable bubbles, the interface can be stretched, compressed and deformed by the flow. In order to accurately capture this, we will resort to adding and deleting points on the front grid and subsequently reset the connectivity of the marker points. The resulting sharp corners which might arise from the re-griding is then smoothed.

4.1.2 Front-grid communications

It is necessary to transfer information between the Eulerian grid and front grid. For instance, the velocity field with which the front is advected must be communicated from grid to front and the surface tension force, which is computed on the front needs to be transfered to the fixed grid. In order to achieve this, we first identify grid points which are close to a given front point. In one direction of length L_x, if we have N_x points where i = 0 refers to the point $x = 0$, then the nearest grid point to the left of the front point, x_f is given by

$$\mathrm{i} = floor(MOD(x_f, L_x) * N_x/L_x), \tag{4.1}$$

where $floor$ is an operation which rounds the number down to the closest integer. $MOD(A, B)$, which gives the remainder of $A \div B$, is necessary when using periodic boundaries. An identical method can be used to identify the nearest grid points in the other two dimensions as well.

Once the grid points nearest to a front point are located, the grid variables needed on the front, like velocity field, can be obtained by interpolation,

$$\phi_f^l = \sum_{\mathrm{ij}k} w_{\mathrm{ij}k}^l \phi_{\mathrm{ij}k}, \tag{4.2}$$

where ϕ_f^l and ϕ_{ijk} are the variable values on the front at location l and on the grid, respectively. w_{ijk}^l is the weight of each grid point with respect to location l. Summation is done over all the neighboring grid points of the front which are considered for interpolation.

Interpolation of quantities from the front to the grid, such as surface tension, can also be done as,

$$\phi_{\mathrm{ijk}} = \sum_l w_{\mathrm{ijk}}^l \phi_f^l \frac{\Delta s_l}{\Delta x \Delta y \Delta z}, \tag{4.3}$$

where Δs_l is the area of element l and Δx, Δy and Δz are grid spacings in the three directions.

The weighting function w_{ijk}^l is the product of one-dimensional functions, $w_{\mathrm{ijk}}^l(x_f^l) = d(r_x)d(r_y)d(r_z)$. Here, r_x is the scaled distance $r_x = (x_f^l - \mathrm{i}\Delta x)/\Delta x$. r_y and r_z are calculated similarly. The one-dimensional smooth weighting function used was introduced by Peskin [12] and readers are referred to this article for more details. Once the velocity at each point on the front is computed, the new position of the front can be found by advection using the second order Runge Kutta scheme for time integration.

4.1.3 Constructing the color function

In the front-tracking method, the boundary between the two phases, the front, is advected. However, fluid properties such as density and viscosity are not advected directly. We thus construct a color function, Φ, from the front to identify the two phases and update the fluid properties at each time step. This is done by finding the gradient of the color function on the fixed grid from the front grid and then integrating it. The color function is uniform except at the front where it jumps from zero to one. Therefore, the gradient of the color function is zero everywhere except on the front. On the front the direction of gradient vector is normal to the interface pointing outward from the bubble and its magnitude is given by $\nabla\Phi = \int \Delta\Phi \mathbf{n}\delta(\mathbf{x} - \mathbf{x_f})ds$, where $\Delta\Phi$ is the jump in the value of the color function across the interface and δ is the Dirac Delta function. The gradient on the fixed grid is obtained using equation 4.3.

Once $\nabla\Phi$ is obtained, Φ itself can be obtained by discretizing

$$\nabla^2\Phi = \nabla \cdot (\nabla\Phi). \tag{4.4}$$

This equation can be discretized and solved by the Poisson solver.

4.1.4 Surface tension

The surface tension force is calculated as the total force on a small segment of the front, $f_\sigma = \int \sigma\kappa'\mathbf{n}'\delta^b(\mathbf{x}-\mathbf{x}')dA'$. The term is evaluated at point $\mathbf{x}$ while $\mathbf{x}'$ is a point on the interface, leading to the delta function, δ^b, discontinuous at the interface.

The mean curvature of the surface is $\kappa'\mathbf{n}' = (\mathbf{n}' \times \nabla) \times \mathbf{n}'$. The force on a surface segment can be simplified to $\Delta f = \sigma \oint_C \mathbf{P}dl$, where $\mathbf{P}$ is the direction of pull due to the surface tension force and C is the boundary of the surface segment.

Part of the surface segment for the point X is shown in figure 4.3 in the shaded region. X can be connected to arbitrary number of elements with each of these elements containing a part of the surface segment and thus each contributing to the surface tension force at point X. If we consider the element e, X_M, Y_M and Z_M are mid points of the element and G is the centroid. The force on the side connecting X and Y_M is canceled by the equal and opposite force from the other element sharing a border with XZ. Same is true for the force on $X - Z_M$. We are thus left with two contributing forces due to element e on point X which are from sides $Z_M - G$ and $Y_M - G$ in the directions **P2** and **P1**, respectively. The net contribution can thus be simplified to $\mathbf{P1}\Delta s_1 + \mathbf{P2}\Delta s_2 = \frac{1}{2}\mathbf{n} \times \Delta x_{ZY}$, where $\mathbf{n}$ is the normal to element e, Δs_1 and Δs_2 are the lengths of segments $Z_M - G$ and $Y_M - G$, respectively and Δx_{ZY} is the length of YZ. The simplification is done by using the definitions of mid points and centroids. Thus, the contribution of the surface tension force due to element e on each node can be found. At each node the contributions of the elements surrounding it must be added to find the total force.

Once the surface tension force is calculated on the front, it can be smoothed onto the grid by using equation 4.3.

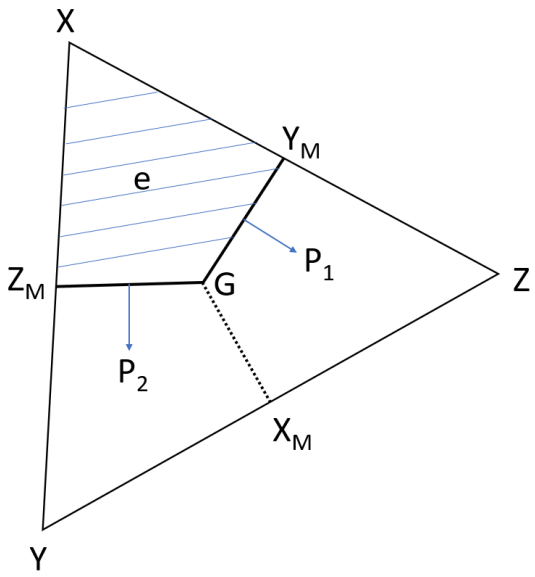

(a)

Figure 4.3. Curvature calculation for front-tracking method

4.2 Single bubble dynamics

For this study, we will use a partial differential equation solver called Basilisk, which is a code that contains second-order accurate finite volume solver for the Navier-Stokes equations. It uses an adaptive mesh refinement techniquie and a second order staggered-in-time discretization, simplified using a time-splitting projection method [9]. The resulting Poisson equation is solved using quadtree-based multilevel solver, described in [13]. An implicit viscosity solver is used. A graded quadtree partitioning is used for spatial discretization. Readers are again referred to [13] for further details. Volume of fluid (VOF) method is used for interface tracking.

4.2.1 Volume of Fluid

In the VOF method, volume fraction C is used to track the interface. C has a value of 0 or 1 depending on the fluid phase in cells which are fully occupied by one phase. At the interface cell C takes values between 0 and 1, which is the volume fraction of

the cell. In this method the solution for the advection equation of the volume fraction is approximated.

$$\frac{\partial C}{\partial t} + \nabla \cdot (C\mathbf{u}) = 0 \tag{4.5}$$

Since we perform an axisymmetric simulation, we will describe the volume of fluid method in two dimensions. There are two major steps involved in the Volume of fluid method:

- Reconstruction of interface shape from the volume fraction
- Advection of the reconstructed interface

The multidimensional VOF scheme is implemented by using dimensional splitting. The fluxes along one direction are computed and an intermediate C is calculated. This is repeated for the other direction.

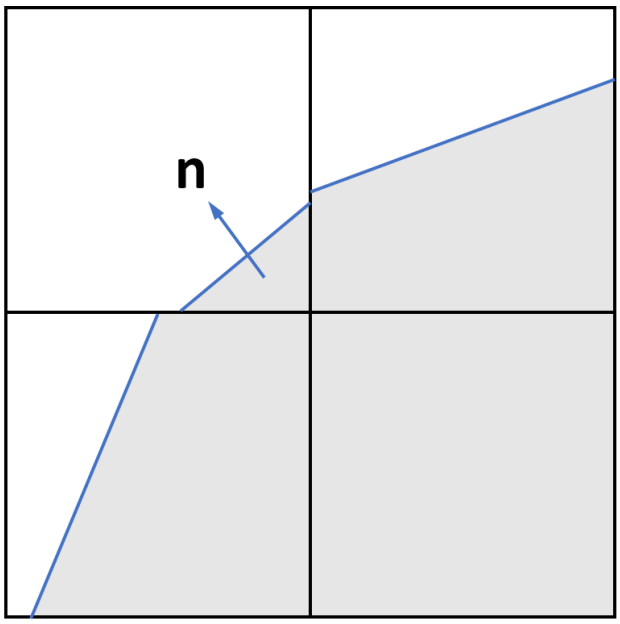

(a)

Figure 4.4. PLIC reconstruction of the interface

In order to reconstruct the interface using the PLIC (Piecewise linear interface calculation) method, we first need to find the normal **n** using the volume fraction values

in the cells. The equation of the interface in the cell is then written, as $n_x x + n_y y = I$, where I is the intercept. Once we know the normal, the line can be moved along the normal direction and the parameter I can be adjusted, so that the area under the interface is $\Delta x \Delta y C_{\mathrm{ij}}$. Schematic of a reconstructed interface using PLIC method is shown in figure 4.4.

The interface normal is calculated by a Mixed-Youngs-Centered method [14], where the best interface is constructed from the Youngs method [15], [16] and the Centered Columns method.

In the Youngs method, the normal $\mathbf{n}$ is evaluated as the gradient $\mathbf{n} = -\nabla_h C$ with finite differences. The normal vector at the four corners of the cell are first calculated. For instance, for the top left corner of cell i, j, the normal components would be

$$n_{x:\mathrm{i}-1/2,\mathrm{j}+1/2} = -\frac{1}{2h}(C_{\mathrm{i,j}} + C_{\mathrm{i,j+1}} - C_{\mathrm{i-1,j}} - C_{\mathrm{i-1,j+1}}),$$

$$n_{y:\mathrm{i}-1/2,\mathrm{j}+1/2} = -\frac{1}{2h}(C_{\mathrm{i-1,j+1}} + C_{\mathrm{i,j+1}} - C_{\mathrm{i,j}} - C_{\mathrm{i-1,j}}).$$

Normal components for the other cell corners can be similarly evaluated and the normal of the cell center is computed as the average of the cell corners.

In the Centered Columns method, the volume fractions can be added columnwise to give a height function $y = f(x)$ or rowwise to give a width function $x = g(y)$ for the same block of cells. For example, the height $y_{\mathrm{i}-1}$ at $x_{\mathrm{i}-1}$ placed in the center of the column is given by $hy_{\mathrm{i}-1} = h^2 \sum_{k=-1}^{1} C_{\mathrm{i}-1,\mathrm{j}+k}$, where h is the length of the side of the cell. The height function in the central block is approximated by the equation $sgn(n_y)y = -n_x x + I'$. The slope n_x is computed using the centered scheme as $n_x = -\frac{1}{2h}(y_{\mathrm{i}+1} - y\mathrm{i} - 1)$. We also need the sign of n_y, since by adding the volume fraction column-wise, we lose information as to which phase is on top or on the bottom of the cell block. n_y is calculated as $n_y = -\partial C/\partial y$ and the sign can be evaluated using finite differences. The interface can also be described by a width function as mentioned previously. Following similar procedure as for the height function, we can construct the interface line using the width function as well.

Thus we obtain slopes using the height and width functions using the Centered Columns method and also the slope using the Youngs method. The best among these slopes is chosen to reconstruct the interface as outlined in [14].

Once the normal is obtained, the intercept can then be computed with the knowledge of C and n_x, n_y. The volume fraction flux is then calculated from the upwind cell volume fraction. Following this, the volume fraction field can be updated according to the advection equation 4.5.

The surface tension force here is evaluated using the Continuous Surface Force (CSF) method. The force f_σ is computed as $\sigma\kappa'\mathbf{n}'\delta^b$. In CSF method, the δ^b distribution is approximated by $|\nabla C|$, since the color function approximates the Heaviside function.

5. INDUCED MIXING IN STRATIFIED FLUIDS BY RISING BUBBLES IN A HELE-SHAW CELL

5.1 Literature Review

Motion of bubbles in confined Hele-Shaw cells has gained tremendous importance in recent times. Confinement of bubbles alters the bubble dynamics. There is a thin liquid film between the bubble and the wall. The bubble wake is subjected to shear stress at the wall, and the wake length is of the order of a few bubble diameters, which is less than in unbounded flows. Mixing in the background liquid can occur either due to the transport by the bubble wake or due to turbulent dispersion [18]. In a configuration where the bubbles are confined in a thin gap, turbulence cannot occur even at high Reynolds numbers (Re) since the vortices have a short lifetime [19], [3]. A flattened bubble has a much larger interfacial area, and hence effective diameter, for a given bubble volume in comparison to an unconfined bubble. Thus, the mixing in the background fluid is mainly caused by the bubble wakes, despite large Reynolds numbers. Bush and Eames [20] showed through experimental and analytical studies that the primary wake advects fluid with the bubble generating an enhanced reflux and promoting longitudinal dispersion. They chose the confined geometry since the effects of drift and reflux are more pronounced in two dimensions with simpler flow visualization. Alméras et. al. [18] experimentally studied the transport and mixing of low-diffusivity dye in a homogeneous swarm of bubbles. They observed that at low void fractions, α, the diffusion coefficient scales as $\alpha^{0.4}$ in unconfined flows. They established that in confined flows, mixing could not be modeled as a diffusion process since it occurs due to the transport by bubble wakes. Bouche et. al. [19] also conducted experiments to study the mixing of a passive scalar with a low diffusivity in a swarm of bubbles. It was shown that mixing is enhanced in the confined geometry due to the

dominant role of the bubble wake in the scalar transport. The Fickian law of diffusion cannot reproduce the mixing since the temporal evolution of the dye concentration in the observation window was seen to decay exponentially.

The differences in confined and unconfined bubbly flows can further be characterized by looking at the rise velocity and velocity fluctuations of the bubbles. It was shown through experiments that for high Reynolds number bubbles rising in a Hele-Shaw cell, the drag coefficient is constant for a wide range of Reynolds numbers, in contrast to the unconfined case [21]. The vorticity is attenuated due to the confinement. The combined numerical and experimental studies by Wang et. al. [22] showed that with an increase in the gap width, the drag coefficient decreases accompanied by an increase in the bubble terminal velocity. They also showed that as the gap width is increased, the wake length becomes larger. Study of rising motion of bubbles near a vertical wall [23] reported an increase in average rise velocity of bubbles with an increase in void fraction between 3.75% and 60% due to the formation of vertical clusters. It was further shown [24] that in confined bubbly flows, velocity fluctuations are due to the disturbances localized near the bubbles, and scale as $\alpha^{0.46}$ in the vertical direction, while in the horizontal direction the fluctuations are mainly due to the vortex shedding. They also reported a slight increase in the vertical rise velocity with an increase in void fraction. This is in contrast with the unconfined case. Thus the classic hindrance effect used to explain the bubble rise velocity trend in the unconfined case is not valid here. The study of agitation in the liquid phase due to rising bubbles in a thin gap further confirms the fact that vertical fluctuations are governed by hydrodynamic interactions [3]. These fluctuations were attributed to the flow disturbances localized in the bubble vicinity.

The rising motion of bubbles and drops in a stably stratified fluid causes de-stratification and mixing of the density layers [25], [26]. The bubble dynamics is also affected by the stratification. Bayareh et. al. [27] studied the dynamics of two drops in a density stratified fluid. They reported the suppression of horizontal and vertical motion for the side-by-side drop configuration. In-line drops are shown to retain their configuration, unlike the non-stratified case. The rise velocity and velocity fluctuation

of a swarm of drops rising in a linearly stratified fluid are suppressed compared to the homogeneous case [25]. Dabiri et. al. [25] also reported enhanced horizontal cluster formation. Ardekani et. al. [26] reported a similar trend in their study of the motion of particles and drops in stratified fluids. Chen and Cardoso [28] studied mixing induced in a two-layer density stratification by a bubble plume. They showed that small bubbles de-stratify the lower layer, while large bubbles increase the density of the upper layer. In the case of large bubbles rising through a stably-stratified sharp interface with a zigzag trajectory, it was seen that the drift volume detaches from the bubble, leaving a trail of heavier fluid in the lighter phase leading to enhanced mixing [29]. In the case of a bubble plume rising through a step density distribution [30], it was shown that the liquid plume impinged on the interface and split. About 20% of the volume flux followed the bubbles into the upper layer, while the larger volume flux entrained the upper layer fluid and fell back onto the top of the lower layer, reducing stratification. They further demonstrated that, in the case of a linear density distribution, three distinct layers are formed. The top and bottom layers are similar to those formed in the step density distribution, while the middle layer preserves the linear stratification. This middle layer reduces in length and ultimately vanishes, leading to the step density configuration. Neto et. al. [31] conducted similar experiments where a bubble plume rising through the ambient fluid with two-layer stratification is negatively buoyant when the mixture reaches the top layer and forms a fountain. The speed of the bubbles exceeds the speed of the fountain due to which the lower layer of the fountain rises a finite distance in the upper layer entraining the upper layer fluid. After a finite time, the entrained liquid collapses, leading to an intermediate mixing layer. Blanchette [32] used numerical simulations to describe the effects of settling particles on a temperature stratified fluid. It was seen that for the settling of a single particle, the time evolution of the height of an isopycnal shows a damped oscillatory motion with a period of the order of $1/N$, where N is the $Brunt - V\ddot{a}is\ddot{a}l\ddot{a}$ frequency. As volume fraction of the particles increases, the stratification is disrupted, giving rise to a well-mixed fluid. Wang and Ardekani [33] studied biogenic mixing of swimmers in stratified fluids. Mixing was quantified in terms of Cox number, diapycnal eddy dif-

fusivity and mixing efficiency. Mixing characteristics were seen to increase with higher volume fractions and higher density stratification.

Despite the above-mentioned studies, the mixing of density stratified fluids due to bubble motion in a confined geometry is poorly understood. The confined case is of importance because we are able to isolate the effects that bubble wake transport has on mixing. In the present numerical study, the effects of density stratification and confinement on the rising motion of bubbles have been tackled. An insight into various physical parameters that describes the flow has been presented, and the mixing induced by the bubble motion has been quantified. Path instability in the confined domain caused by periodic vortex shedding is observed and quantified. It is seen that as void fraction, α, increases, the buoyancy flux across the pycnoclines increases. It is also shown that with an increase in the stratification strength, the fraction of total energy lost to buoyancy increases.

5.2 Problem Description

Our objective is to simulate the rising motion of air bubbles in a narrow gap between two rigid walls in a temperature stratified Newtonian fluid. The distance between the walls is comparable to the effective diameter of the bubbles. The two boundaries in the z-direction are fixed (see figure 5.1a) and have no-slip velocity boundary conditions. The effective bubble diameter, d_{eff}, is dependent on the separation between the two fixed walls, w. In the present simulations, monodisperse distribution of bubbles with $w/d \approx 0.31$, where d is the initial effective bubble diameter, is maintained. A periodic velocity boundary condition is imposed in the x and y directions. Linear temperature stratification is initially imposed in the y-direction (vertical). T is the actual temperature which is given by $T = T_m + \frac{dT}{dy}y$, where $\frac{dT}{dy}$ is the constant background temperature gradient. The second term gives rise to a temperature field linearly varying in y. T_m is the temperature perturbation. Thus, in order to maintain the linear background stratification, a periodic boundary condition is implemented for the temperature perturbation, T_m. The temperature stratification leads to a linear density stratification.

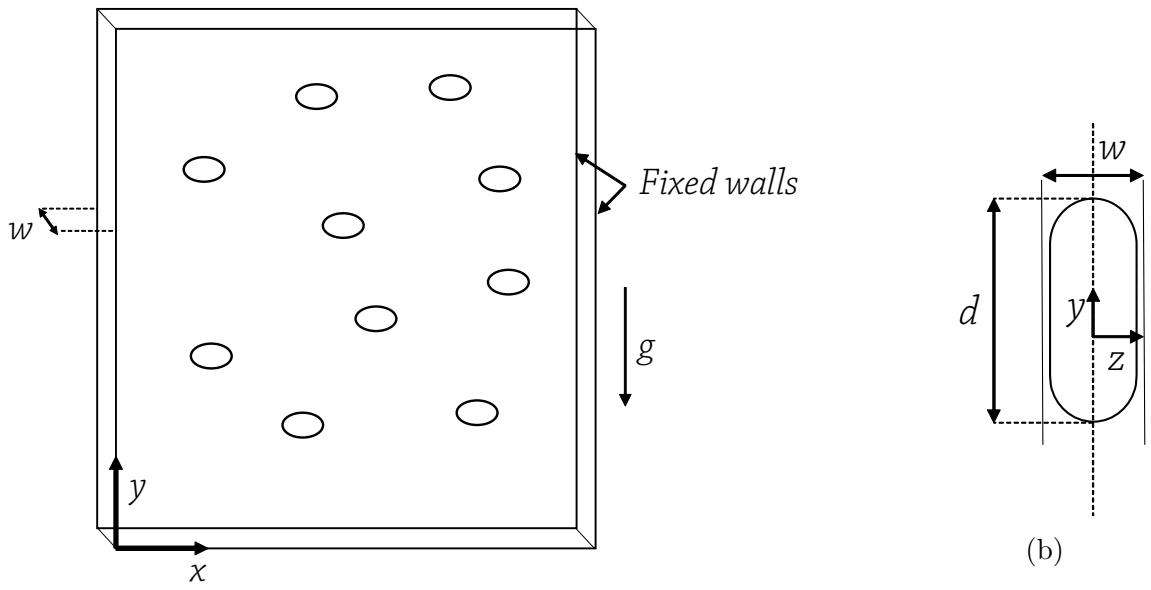

(a) (b)

Figure 5.1. Schematic of the computational set-up (a) view of the bubbles rising in the domain (b) $y-z$ view of a single bubble which is confined between two solid walls

Even though we use temperature as the stratifying agent in our study, the analysis for concentration stratification is similar.

The bubbles are initialized with their z-centers at the midpoint between the two walls. Since the effective bubble diameter is much larger than the gap between the walls, the bubbles are initialized as ellipsoids. The effective two-dimensional diameter of the bubble is calculated as $d_{eff} = \sqrt{4A/\pi}$, where A is the projected area of the bubble in the $x-y$ plane. The given configuration leads to a free rise of bubbles under the effect of buoyancy. As the bubbles rise, they become flattened and confined (fig 5.1b) between the solid walls.

The dimensionless parameters used to characterize the motion of bubbles include the Archimedes number, $Ar = \rho_f \sqrt{gd} d/\mu_f$, Reynolds number, $Re_0 = \rho_f V_0 d/\mu_f$, Bond number, $Bo = \rho_f g d^2/\sigma$ and Weber number, $We = \rho_f V_0^2 d/\sigma$, which is the ratio of inertial to interfacial force. These four quantities are kept fixed throughout this study at $Re = 460$, $Ar = 807$, $Bo = 3.46$ and $We = 1.12$. These values essentially represent air bubbles of diameter 3.8mm in water. Here ρ_f and μ_f are the density and dynamic viscosity of the background fluid, d is the bubble diameter, g is the gravitational acceleration, σ is the interfacial tension and $V_0 = 0.57\sqrt{gd}$ is the mean rise velocity of an isolated bubble at $600 \leq Ar \leq 1500$ [21], [24]. The stratification of the background fluid can be characterized by the Froude number $Fr = V_0/(Nd)$. Here N, the *Brunt-Väisälä* frequency, also known as the buoyancy frequency, is given by $N = (\beta g/\rho_0)^{1/2}$. In the expression for N, β is the vertical density gradient in the background fluid and ρ_0 is the background density without the stratification. The void fraction, α, of N_b number of bubbles in the domain is given by $\alpha = \frac{4}{3} N_b \pi abc/(LBw)$ where a, b and c are the axis lengths of the initially ellipsoidal bubble, w is the gap between the two walls while L and B are the length and breadth of the computational domain. Fr and α are varied in the simulations to achieve different levels of background stratification and different flow configurations. The density and viscosity ratios of the background fluid to the bubbles are maintained at $\rho_f/\rho_d = 100$ and $\mu_f/\mu_d = 10$.

Bubble dynamics is analyzed by studying the average velocity of bubbles at different void fractions and stratification strengths, which is quantified by the Froude

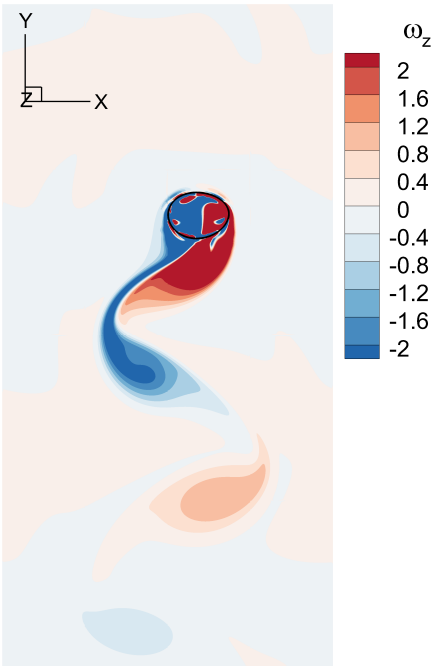

Figure 5.2. Contours of non-dimensional vorticity for a single bubble in computational domain at t=1.57s

number. Bubble dispersion and trajectories are studied. The autocorrelation function of horizontal bubble velocity gives interesting insights into the path and behavior of the bubbles. We also quantify the mixing which takes place in the background fluid, by computing mixing efficiency, diapycnal eddy diffusivity, and the Cox number.

5.3 Results and Discussion

Simulations are run in a doubly periodic domain with a size of $5d \times 10d \times 0.31d$. 4.19 million grid points are used to resolve the flow, with 51 points across the bubble diameter initially. Void fractions of 3.35%, 8.37%, and 13.4% are used. The flow configuration represents air bubbles of diameter 3.8mm in water. Initial Reynolds number of $Re_0 = \frac{\rho_f (0.57\sqrt{gd})d}{\mu_f} \approx 460$ is used for all the simulations.

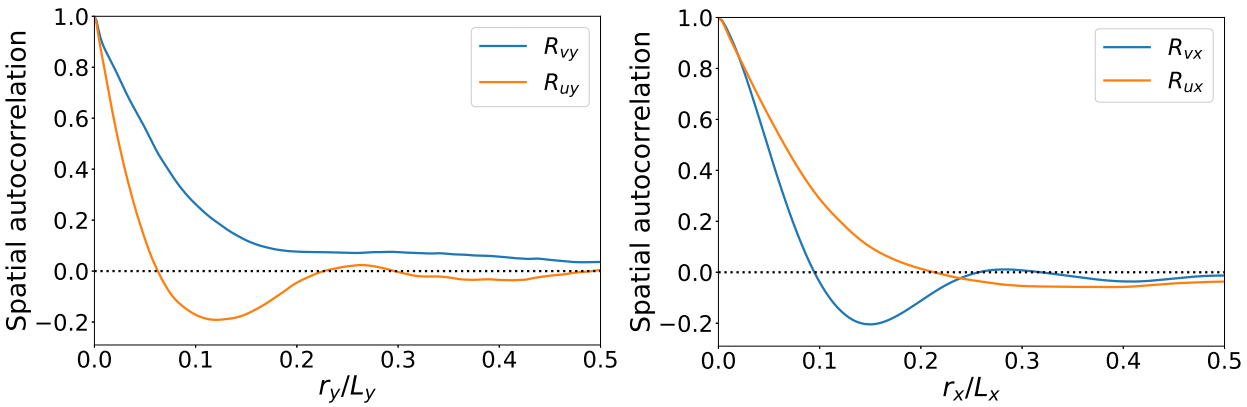

(a) (b)

Figure 5.3. Spatial velocity correlation for the domain in the (a) Vertical direction (b) Horizontal direction for $\alpha = 13.4\%$

5.3.1 Domain size dependence

The computational domain size is tested for domain size dependency. The length of the domain in the vertical direction is the most important one due to the wake of the bubble. It must be made sure that any bubble does not interact with its own wake once it crosses the boundary of the periodic domain and re-enters on the other side. This implies that the length of the domain must be greater than the length of the wake. The length of the wake behind the bubble decreases as the void fraction increases due to the interaction between the bubbles [3]. Thus looking at the wake for a single bubble is appropriate when testing for domain size dependency.

Simulations are run with a single bubble in the computational domain at an $\alpha = 0.84\%$ with $L_y = 10d$. The non-dimensional vorticity contours are plotted (figure 5.2). Non-dimensionalization is done by dividing vorticity by $v_{b,avg}/d$, where $v_{b,avg}$ is the average rise velocity of the bubbles. Periodic vortex shedding consisting of counter-rotating vortices can be seen behind the bubble. The vortices which are detached from behind the bubble die out rapidly. Simulations are also run with $L_y = 20d$, and the bubble Reynolds numbers in the vertical direction are compared. It was found that the difference in average Reynolds number between the two cases is 0.8%. Hence, $L_y = 10d$ is used for the rest of the results.

We further look at the spatial autocorrelations of both vertical (v) and horizontal (u) velocities with spacing in the vertical (r_y) (figure 5.3a) and horizontal(r_x) (figure 5.3b) directions for $\alpha = 13.4\%$. Both r_x and r_y have been non-dimensionalized by L_x and L_y, respectively, and the autocorrelation has been time-averaged after the flow has reached a statistically steady state. Figure 5.3 shows that as the spacing is increased both in the horizontal and vertical directions, the autocorrelation dies to 0 as r_x and r_y approach $L_x/2$ and $L_y/2$, respectively. Thus we can conclude that for the periodic boundaries, the domain size is sufficiently large.

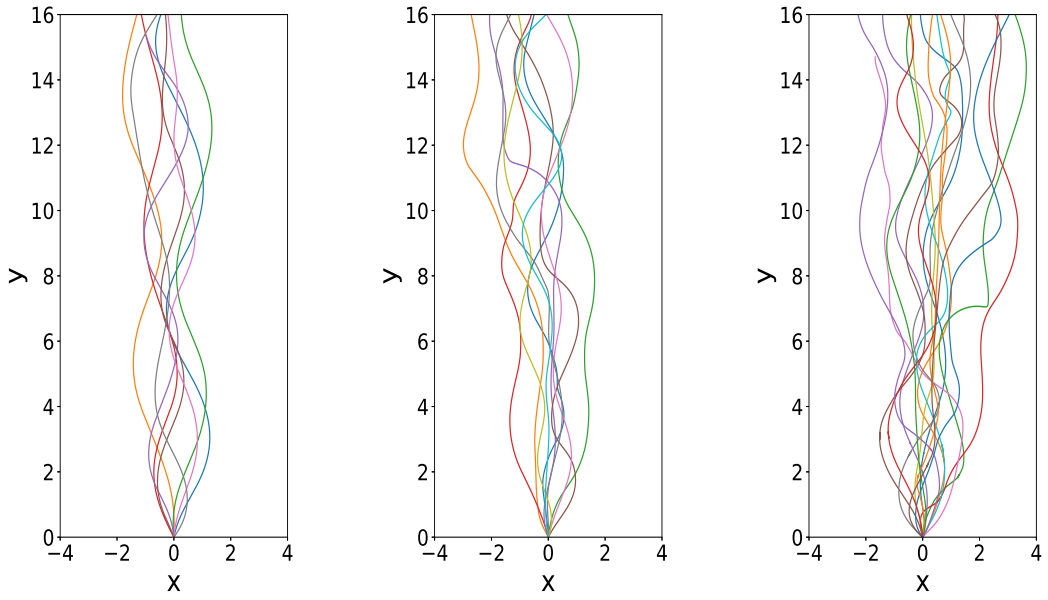

(a) (b) (c)

Figure 5.4. Bubble center displacements for α = (a) 3.35%, (b) 8.37% and (c) 13.4% at $Fr = 6.37$

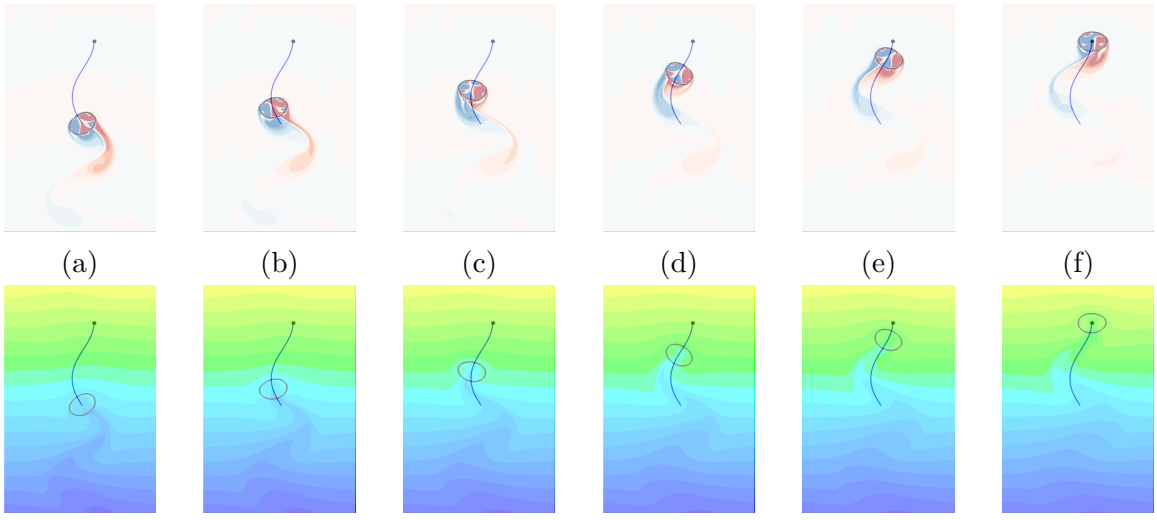

(a) (b) (c) (d) (e) (f)

(g) (h) (i) (j) (k) (l)

Figure 5.5. (a-f)Vorticity (g-l) temperature contours superimposed on bubble trajectory for rise of a single bubble upto t=1.57s

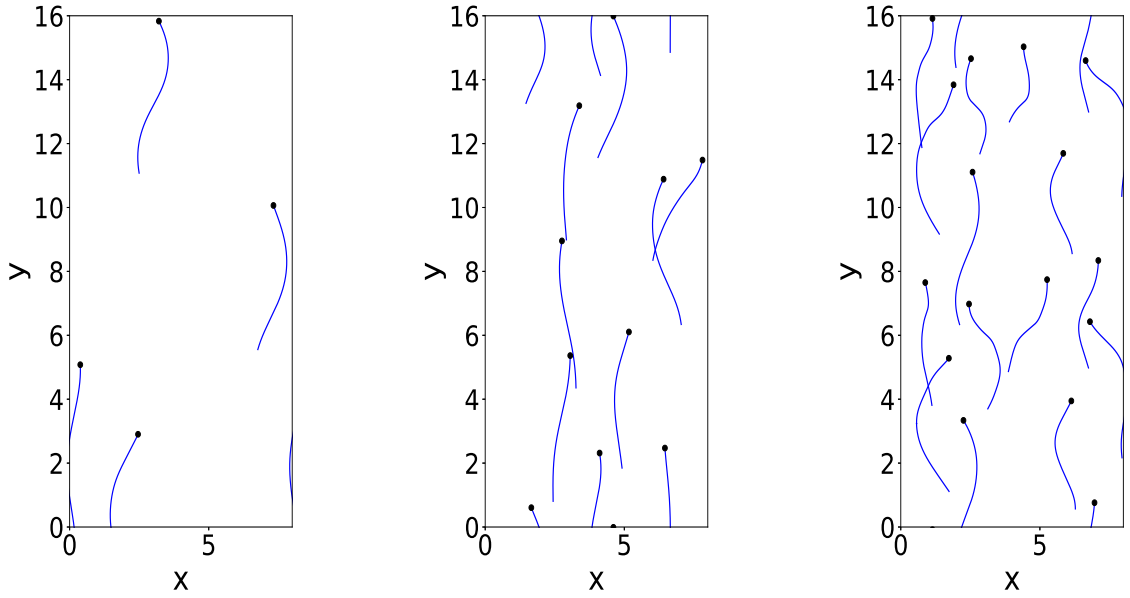

(a) (b) (c)

Figure 5.6. Bubble trajectories for $\alpha =$ (a) 3.35%, (b) 8.37% and (c) 13.4% at $Fr = 6.37$

5.3.2 Bubble trajectories

The dispersion of bubbles in the horizontal direction can be observed by superimposing the displacements of each bubble center with respect to its own location. Figure 5.4 shows that the dispersion increases with an increase in α. For a void fraction of 3.35%, a regular oscillation of bubbles about the center is seen. As α increases, the interactions between the bubbles also increase, and the motion of the bubbles becomes more chaotic, causing more dispersion.

The evolution of the bubble wake vortical and stratification structures with time, when the bubble is moving in a zigzag pattern, is shown in figure 5.5 for a single bubble. The trajectories of bubbles at different void fractions are plotted in figure 5.6 to capture their zigzag motion. It has been experimentally shown [34] that bubbles rise in a zigzag fashion in a Hele-Shaw cell and it was established that it is due to the periodic vortex shedding. This was observed in our simulations, where the counter-rotating nature of the vortices is seen for the case of a single bubble (figure 5.5).

5.3.3 Flow field

Looking at the flow field around the bubbles gives interesting insights into their behavior. Figure 5.7a shows the flow field on the $y - x$ plane with a contour plot of vorticity at a particular time instant. As before, periodic vortex shedding can be observed. At this void fraction ($\alpha = 8.37\%$), the wake of the bubbles interact with each other causing the wake length to be even shorter than the single bubble case. Figure 5.7b shows the temperature contours which are non-dimensionalized by the highest temperature value at t=0. The linearity of the temperature profile in the y-direction has been disrupted by the bubbles. The transport of lower, denser layers of fluid into the upper layers by the bubble wake can be clearly seen.

The flow pattern inside the bubble is realized by plotting the planar streamlines in a frame of reference moving with the bubbles (figure 5.8). Figures 5.8a,b show the streamlines on the $y - x$ plane at $z = z_c$, while figure 5.8c shows the same on the $y - z$ plane at $x = x_c$, where z_c and x_c are the z and x coordinates of the volumetric centroid of the bubble respectively. The streamlines in the $y - z$ plane show the two major toroidal vortices along with recirculation zones at the top and bottom within the bubble. The secondary vortices rotate in a direction opposite to the primary vortices. The recirculation zones appear in the $y - z$ planes to the right of x_c when the bubble has a positive u-velocity and vice versa. This shows that the flow is highly three-dimensional within the bubble. This asymmetry can also be observed in figure 5.8a, where the bubble is moving to the right and 5.8b, where it is moving to the left. The presence of toroidal vortices along with recirculation zones was previously reported by [35], where they analyzed the flow phenomena in a laminar Taylor bubble flow in square mini-channel. In their study, they analyzed the motion of a slug bubble which is confined in two directions as opposed to confinement in a single direction in our case.

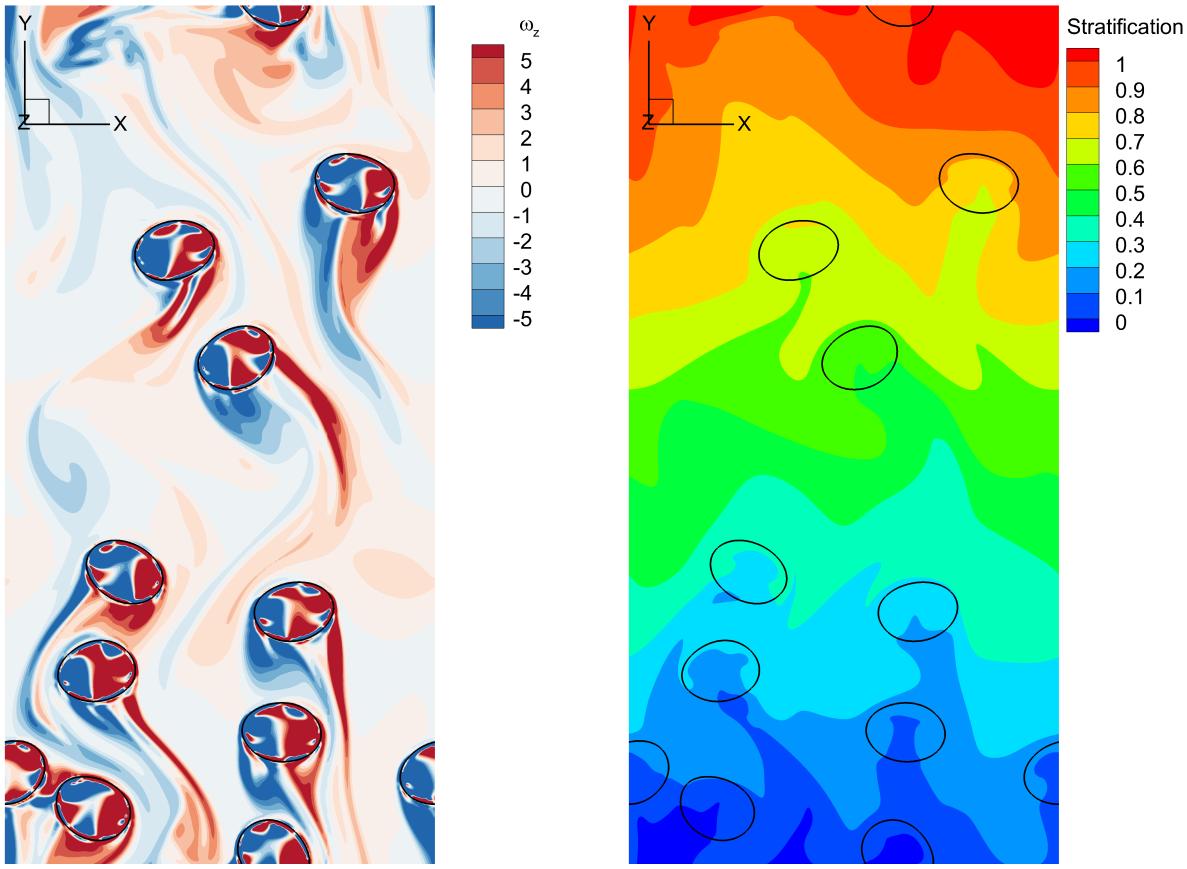

(a) (b)

Figure 5.7. Flow field for $\alpha = 8.37\%$ at $Fr = 6.37$ (a) Non-dimensional z-vorticity contours (b) Temperature contours normalized by its highest value at t=0

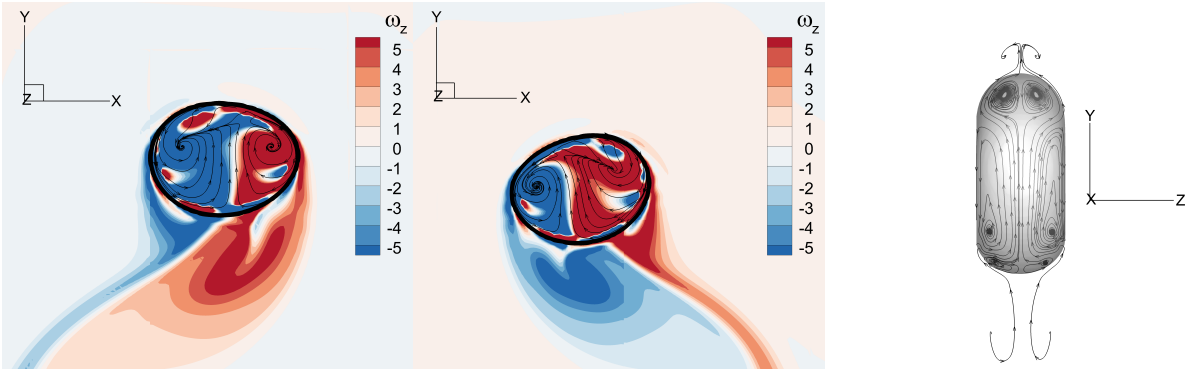

(a) (b) (c)

Figure 5.8. Streamlines within the bubble (a) $y - x$ view at t = 1.57s (b) $y - x$ view t=1.79s and (c) $y - z$ view at t = 1.57s

5.3.4 Rise Velocity

The slip velocity of the bubble swarm is calculated as

$$v_b(t) = \frac{1}{N_b}\sum_{\mathrm{i}=1}^{N_b} v_{b,\mathrm{i}}(t) - \frac{1}{V_f}\int_{V_f} v(x,y,z,t)dV, \tag{5.1}$$

where $v_{b,\mathrm{i}}(t)$ stands for the instantaneous vertical velocity of the i^{th} bubble. The second term in equation 5.1 is the volume-averaged velocity of the background fluid, where V_f is the volume of the background fluid and $v(x,y,z,t)$ is the vertical liquid velocity field of the domain. The steady-state average rise velocity of the bubble swarm is obtained by

$$v_{b,avg} = \frac{1}{T-t_0}\int_{t_0}^{T} v_b(t)dt, \tag{5.2}$$

where the time interval $T - t_0$ is chosen such that the slip velocity of the swarm has crossed the transient stage and is at a statistical steady state.

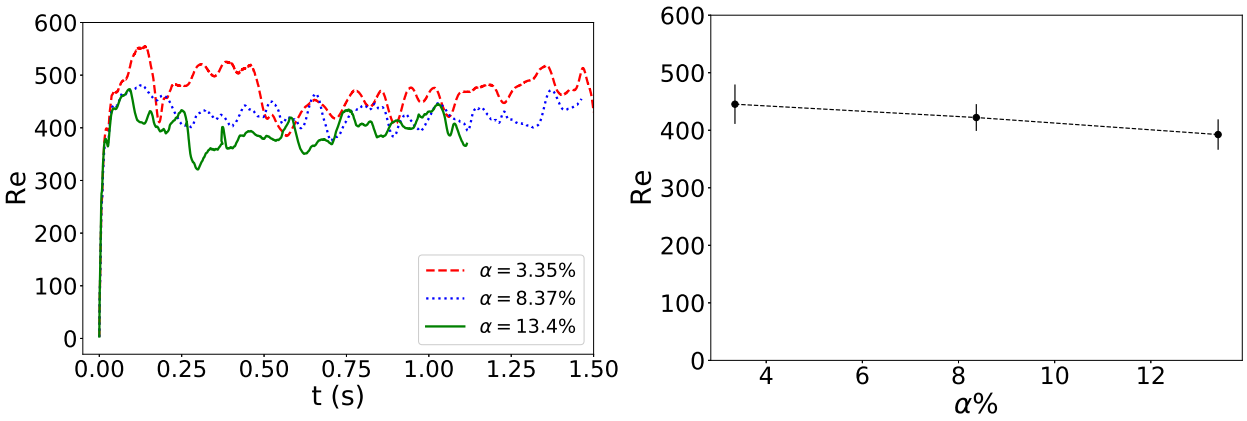

(a) (b)

Figure 5.9. Bubble Reynolds number for different void fraction at Fr=6.37 (a)Instantaneous vs time (b)Time averaged vs void fraction

Figure 5.9a gives the time variation of Reynolds number of the bubbles for different void fractions at $Fr = 6.37$. We see a slight drop in velocity from $\alpha = 3.35\%$ to $\alpha = 13.4\%$ (a 11% decrease). This is more apparent from the plot of time-averaged Reynolds number against void fraction (figure 5.9b). Several simulations with slightly

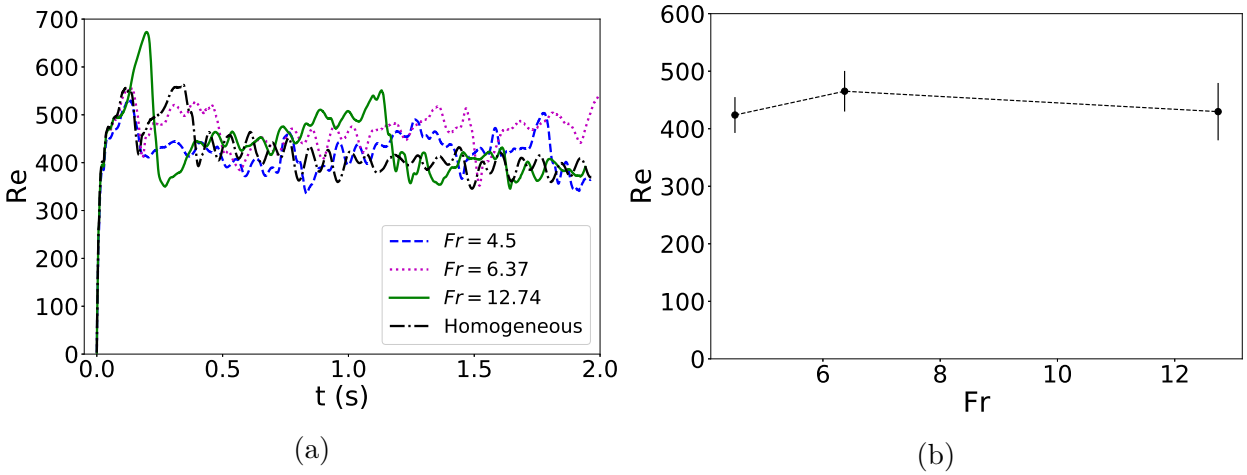

(a) (b)

Figure 5.10. Bubble Reynolds number for different Froude numbers at $\alpha = 3.35\%$ (a)Instantaneous vs time (b)Time averaged vs void fraction

different initial conditions are used to calculate the time-averaged bubble rise velocity with error bars corresponding to the lowest and highest average velocity obtained from these simulations. The error bars show that the variations of velocity for different void fractions overlap, and thus we cannot infer a clear trend. In the unconfined case, a steady and more pronounced (a 30% decrease) drop in rising velocity is observed with an increase in void fraction [36]. This can be explained by the hindrance effect, where there is a downward liquid velocity between the bubbles, which increases as the void fraction increases. We see in the confined domain that the hindrance effect is counteracted by a phenomenon where the bubbles get caught in the wake of neighboring bubbles and are accelerated. This phenomenon happens because, in a confined domain, the number of degrees of freedom of the bubbles is less than an unconfined case leading to more wake interactions.

Figure 5.10a gives the time variation of the Reynolds number of the bubbles for different Froude numbers at $\alpha = 3.35\%$. The time-averaged Reynolds number (figure 5.10b) again does not show a clear trend, and there is almost no change in the fluctuating bubble velocities as the Froude number increases. This is in contrast to the trend observed for drops rising in water [25]. This is because the density difference between the background fluid and air bubbles is large. The change in density in the

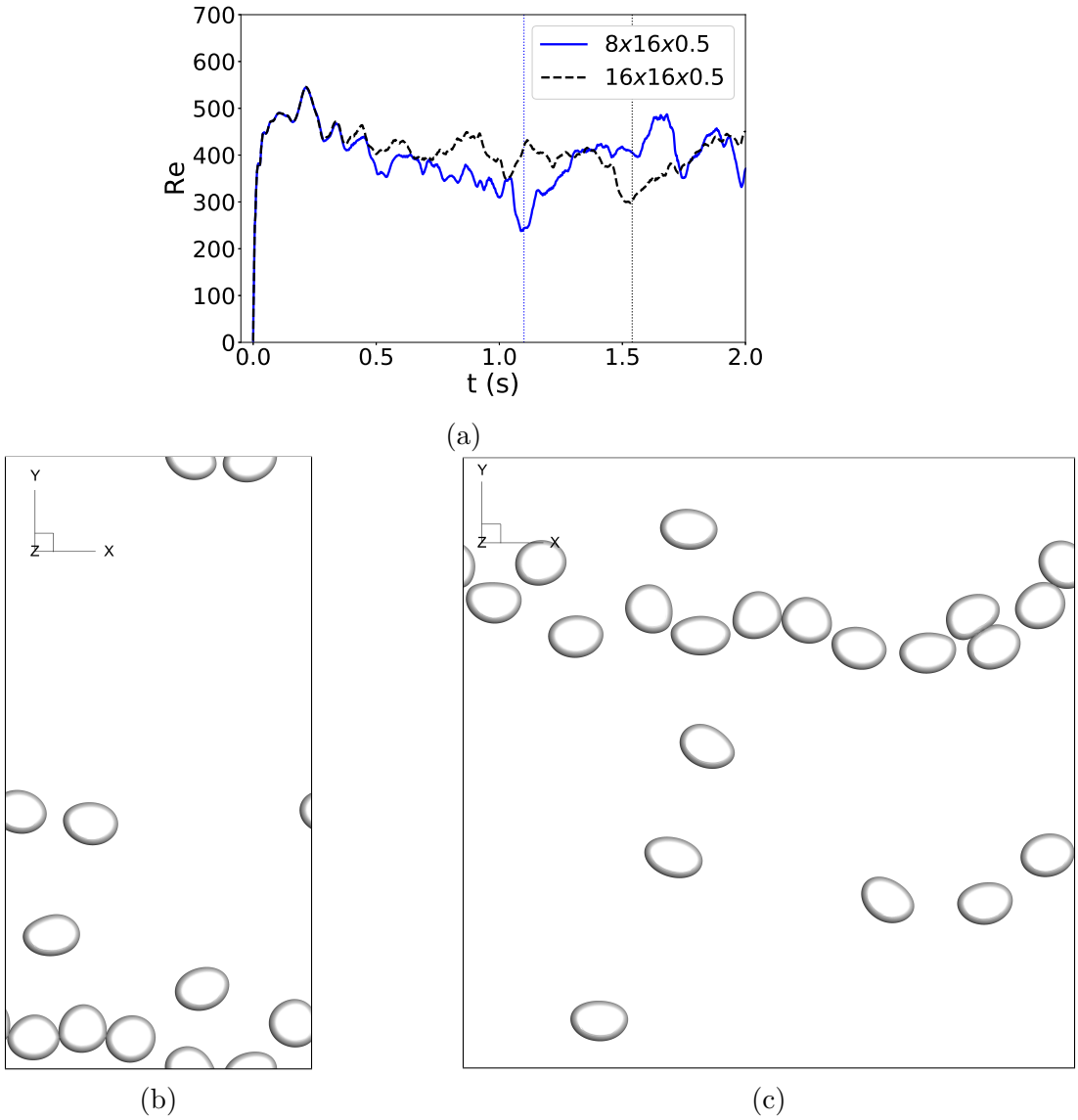

Figure 5.11. (a) Instantaneous bubble Reynolds number over time for different domain sizes. Cluster Formation shown in (b) 8×16 domain at t = 1.1s and (c) 16×16 domain at t = 1.54s.

fluid created by the stratification is small compared to the density difference between the bubbles and the non-stratified fluid. Since buoyancy force causes the bubbles to rise, the rise velocity of the bubbles does not change significantly with stratification at a constant void fraction.

We see from figure 5.9a and 5.10a that the rise velocity shows large fluctuations and drastic dips at isolated times. This happens due to the brief formation of horizontal

clusters. Horizontal clusters have been reported in unconfined bubbly flows in homogeneous density fluids [37],[38] and stratified background fluid [25]. They block the flow and hence cause a drop in the average rise velocity of the bubbles. The velocity dip can happen even when just two bubbles come in close contact in a side-by-side configuration [39].

Figure 5.11a shows the bubble Reynolds number for two different domain sizes $8 \times 16 \times 0.5$ and $16 \times 16 \times 0.5$ (where lengths are non-dimensionalized by $0.625d$). In the second case the domain has been doubled in the horizontal direction, which is the direction in which bubble clusters were observed. This is done in order to see whether the formation of clusters is related to the horizontal size of the periodic domain. The large fluctuations and sudden dips in velocity are observed even in the bigger domain. Figure 5.11b and 5.11c show the formation of horizontal clusters in both the $8 \times 16 \times 0.5$ and $16 \times 16 \times 0.5$ domains at t = 1.1s and t = 1.54s, respectively. At t = 1.1 s, we see a horizontal cluster in the 8×16 domain in figure 5.11b and a corresponding dip at 1.1s is observed in the Reynolds number (see figure 5.11a at the blue dotted line). Similarly, for the 16×16 domain at t = 1.54s, a horizontal cluster (figure 5.11c) and corresponding velocity dip (see figure 5.11a at the black dotted line) can be seen.

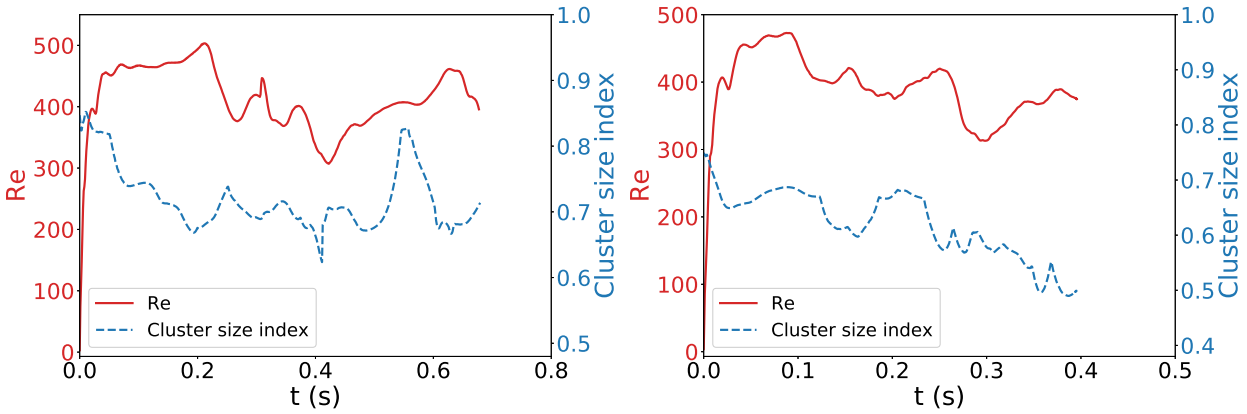

(a) (b)

Figure 5.12. Cluster size index with corresponding Reynolds number for $\alpha =$ (a) 8.37% and (b) 13.4% at Fr=6.37

The formation of horizontal clusters can be quantified by the cluster size index. The marker function is defined as $\phi = 0$ in the dispersed phase and $\phi = 1$ in the continuous liquid phase. We define a cluster size index as follows. Across any horizontal line, the marker function is averaged over the $x - z$ plane, and the minimum through all y locations is taken at each time step. At any time step, a lower value of the cluster size index would imply a higher presence of the gas phase on the horizontal line corresponding to the biggest cluster. This means a larger cluster size. Figure 5.12 shows a plot of the cluster size index and the corresponding Reynolds number (Re) for different void fractions. We see that whenever there is a drop in the cluster size index, there is also a corresponding drop in Re at a slightly later time. This is because the cluster is first formed and then the drop in Re happens (see $t \approx 0.4\text{s}-0.5\text{s}$ in figure 5.12a and $t \approx 0.1\text{s}-0.2\text{s}$ in figure 5.12b). A similar cluster formation and immediate breakup have also been observed in literature in the context of bubbly flow in Hele-Shaw cells by [40].

5.3.5 Velocity Autocorrelation

Autocorrelation of horizontal velocity is defined as follows

$$C_{xx}(t) = \frac{\langle v'_{bx}(T) v'_{bx}(T+t) \rangle}{\langle v'^2_{bx} \rangle}, \tag{5.3}$$

where v_{bx} refers to the horizontal bubble velocity, and primed quantities refer to fluctuations. The autocorrelation function determines the behavior of bubbles in the vertical and horizontal directions, gives a measure of whether there are enough bubbles in the domain, and is used to ensure that the statistics calculated are independent of the number of bubbles initialized.

To calculate the autocorrelation function, we need to determine the Lagrangian time scale. To determine this, we look at the bubble center displacements.

$$x'(t) = x^{(\mathrm{i})}(t) - \left\langle x^{(\mathrm{i})}(t) \right\rangle, \tag{5.4}$$

where superscript i refers to the ith bubble. From analysis by [41] we have

$$\frac{1}{2}\frac{d\left\langle x'^2(t)\right\rangle}{dt} = \left\langle v_{bx}'^2\right\rangle T_x, \tag{5.5}$$

where $\langle\rangle$ refers to averaging over N_b bubbles, and the variances of bubble center displacements are considered for a significant amount of time. Equation 5.5 is used to find the Lagrangian time scale so that all statistics are calculated for time intervals much greater than T_x.

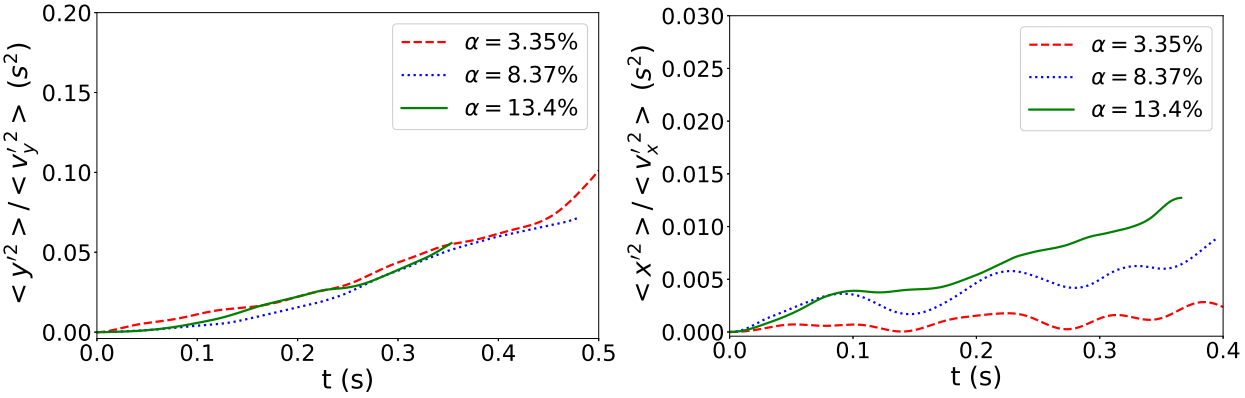

(a) (b)

Figure 5.13. Variance of bubble center displacements with time; (a) and (b) correspond to vertical and horizontal variance at different void fractions at Fr=6.37 respectively

T_x is thus obtained by plotting $\langle x'^2(t)\rangle$ normalized by $\langle v_{bx}'^2\rangle$ vs time and obtaining the slope of the graph (figure 5.13). We see that the vertical timescale, calculated to be $T_y = 0.17$s, is approximately the same for different void fractions (figure 5.13a), a trend also observed by Bouche et. al. [24]. The horizontal timescale increases as void fraction increases (figure 5.13b), and at the highest void fraction, we have $T_x = 0.04$s. Similar values for the horizontal and vertical Lagrangian timescale were also obtained by Bouche et. al. [24]. They have shown that the horizontal Lagrangian integral timescale varies with α as $T_x = 0.33\alpha$s. Thus, for the highest α of 13.4% in our simulations, we have $T_x = 0.045$s, which is very close to the value obtained from our calculations. We also see that the horizontal variance shows oscillations at lower void

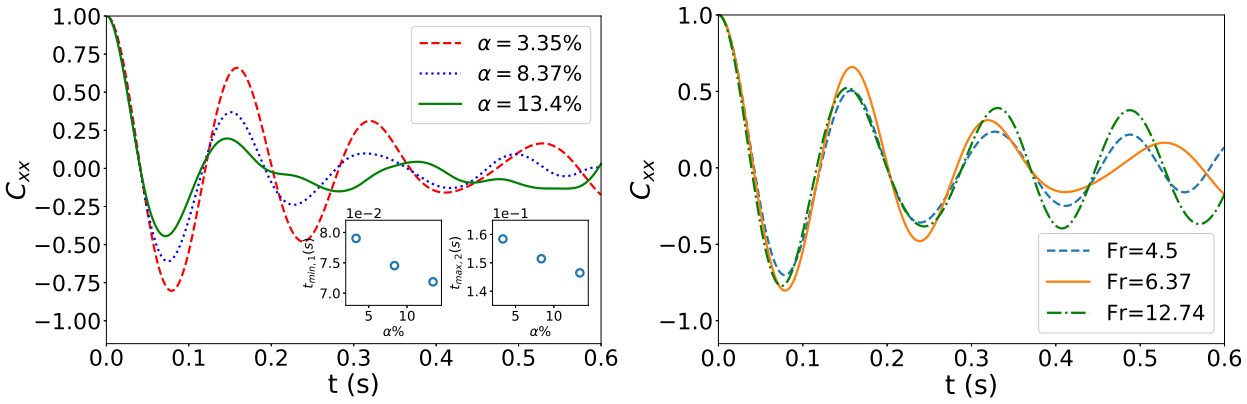

(a) (b)

Figure 5.14. Autocorrelation functions at (a) different void fractions for $Fr = 6.37$ (b) different stratification strengths at $\alpha = 3.35\%$. The inset figures in (a) show the time of minimum amplitude in the first oscillation ($t_{min,1}$) and the time of maximum amplitude in the second oscillation ($t_{max,2}$) as a function of α

fractions similar to what was observed by Bouche et. al. [24]. C_{xx} is obtained for time intervals larger than T_x. We thus plot the horizontal correlations till $t = 0.6$s. Figure 5.14a shows the plot of C_{xx} for different void fractions. It can be seen that for all void fractions, the autocorrelation function gradually dies down with time, which helps in deducing that the domain size is large enough so that the velocities become uncorrelated after a finite amount of time. The behavior of C_{xx} is also similar to a damped sine wave, which helps to reiterate the fact that the bubbles are moving in a zigzag motion. In fact, in their numerical study of bubbly flow in a Hele-Shaw cell, Wang et. al. [42] quantified this horizontal vibration of bubbles using a sine function and investigated the relation between the shape and size of the bubbles and the period of vibration.

It is also seen from figure 5.14a that, as void fraction increases, the autocorrelation function dies to zero more rapidly. The periodic vortex shedding drives the zigzag bubble path. As void fraction increases, bubbles interact with the wake of neighboring bubbles, leading to suppression of the orderliness exhibited in the low void fraction region. This, in turn, results in the x-velocities of the bubbles being uncorrelated at a smaller time interval as α increases. The frequency of oscillation increases mildly with

void fraction. From the insets of figure 5.14a, the first minimum and second maximum amplitude occurs at lower times as α increases. The zigzagging of the bubbles occur at higher frequency at higher void fractions.

A comparison of C_{xx} for different stratification cases is presented in figure 5.14b. The time periods of oscillation for all the cases are almost the same with a value of approximately 0.15s. The amplitudes of C_{xx} for the cases also do not vary significantly. This is again attributed to the fact that the density difference between air bubbles and the background liquid is large, because of which the stratification does not have a significant effect on the bubble dynamics.

5.3.6 Mixing

The vortex shedding behind the bubbles, which gives them the zigzag trajectory, also induces mixing in the background fluid. It has been shown [29] that a bubble moving in a zigzag path causes instability and enhances mixing compared to a bubble moving in a rectilinear path. As they move up, the bubbles entrain the background fluid, and the isopycnals get displaced. Once disturbed, the displacement of the isopycnals can be modeled as a damped oscillation with a frequency N, and the time taken for the isopycnals to come back to their stable state is of the order of $1/N$. Mixing occurs when the isopycnals get disturbed repeatedly before they come back to their stable state. Osborn [43] defined the mixing efficiency and related measurements of energy dissipation to the rate of cross-isopycnal turbulent mixing. In order to quantify the strength of mixing in the background fluid, the following physical parameters are used.

Diapycnal eddy diffusivity gives the vertical mass flux (it represents the cross isopycnal diffusion) and is defined [43] as

$$K_\rho = -\frac{g\overline{\rho' v'}}{\rho_0 N^2}, \tag{5.6}$$

where the overbar represents an ensemble average. This term helps quantify the amount of work done by the buoyancy force.

Cox Number gives the variance of the temperature gradient in the background fluid [44], [45] and is defined as

$$COX = \frac{\overline{(\nabla T')^2}}{(\partial \overline{T}/\partial y)^2}, \tag{5.7}$$

where $\nabla T'$ gives the gradient of the temperature fluctuation or deviation from the linear temperature distribution, and is normalized by the uniform vertical gradient in the mean temperature imposed due to stratification.

Mixing efficiency gives the ratio of the buoyancy flux to the total energy available for mixing [46],[47] and is defined as [43], [48]

$$\Gamma = \frac{-g\overline{\rho' v'}}{-g\overline{\rho' v'} + 2\mu\overline{E : E}}, \tag{5.8}$$

where E represents the strain rate tensor term. The denominator denotes the sum of the viscous dissipation and the loss to buoyancy. There is viscous dissipation in every direction but a loss to buoyancy only in the vertical component, due to which we have very low values of the mixing efficiency.

Even though we do not have turbulence in our domain, we have velocity fluctuations induced by the bubbles. As we have already shown, the motion of the bubbles produces counter-rotating vortices. The bubble wakes also interact with each other. Through the calculation of the diapycnal eddy diffusivity, we are effectively looking at the transport and diffusion of density layers due to bubble induced velocity fluctuations in the background fluid. The capture and transport of fluid in the bubble wake is responsible for the mixing process, and hence looking at these mixing quantities is relevant here.

Effect of void fraction

Figure 5.15 shows the semi-log plot of mixing parameters as a function of time at different void fractions at a Froude number of 6.37. The normalized viscous dissipation is also plotted in figure 5.15c. The diapycnal eddy diffusivity, Cox number and viscous

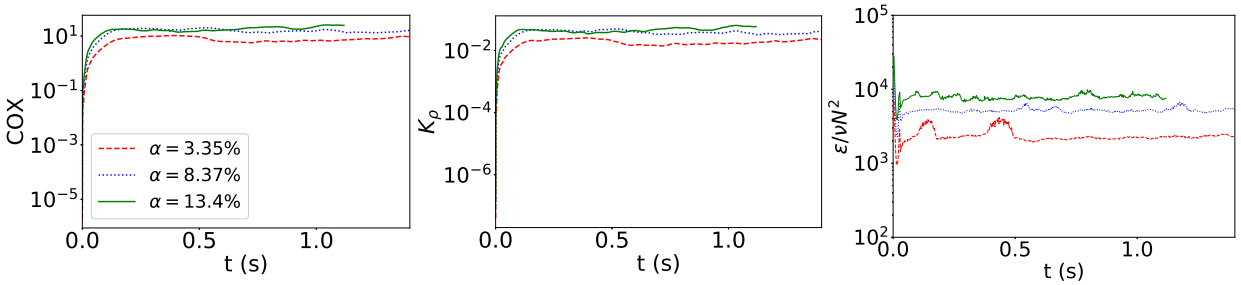

(a) (b) (c)

Figure 5.15. Semi-log plot of mixing parameters for varying α at $Fr = 6.37$ (a) COX number (b) Diapycnal eddy diffusivity (non-dimensionalized by $15cm^2/s$) (c) Normalized viscous dissipation

dissipation reach a steady state with time. We can thus obtain an ensemble average for these parameters. This can also be done for the mixing efficiency, where we get the ensemble averages separately for the numerator and denominator.

Figures 5.17a-c show the variation of the time-averaged mixing quantities with α for two different Froude numbers. The time averaging is done after omitting the initial transient phase. It can be seen that as the void fraction increases, the COX number and eddy diffusivity increase while mixing efficiency decreases slightly. Thus, it can be concluded that as void fraction increases, the buoyancy flux across the pycnoclines increases. However, the viscous dissipation also increases proportionally (figure 5.15c). The competing effects of the viscous dissipation and the vertical mass flux lead to a slightly decreasing trend in Γ. The trends observed for the COX number and the eddy diffusivity are similar. The change in the mixing efficiency with the void fraction is orders of magnitude less than the change in COX number and eddy diffusivity.

The trend in eddy diffusivity, being the measure of cross isopycnal diffusion, can be compared to the diffusion coefficient of a low diffusive dye calculated at different void fractions by Alméras et. al. [49]. They performed experiments to study the mixing induced by bubbles in a Hele-shaw cell. They reported the existence of asymmetry in the concentration profiles, even though the concentration distribution tends towards a normal distribution. They attributed this to the fact that the mixing mechanism in a two-dimensional column is mainly due to capture and transport by bubble wakes, and

turbulent fluctuations are virtually absent. They also observed that an increase in α to 10% resulted in an increase in the diffusion coefficient. Any further increase in α resulted in plateauing of the diffusion coefficient. We also obtain a similar trend in the diapycnal eddy diffusivity where the increase from $\alpha = 3.35\%$ to $\alpha = 8.37\%$ is more pronounced than from $\alpha = 8.37\%$ to $\alpha = 13.4\%$ (see figures 5.15b and 5.17a).

Effect of Froude Number

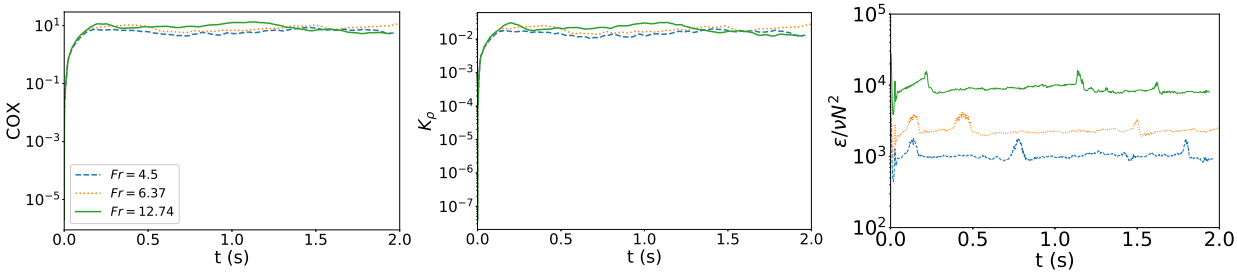

(a) (b) (c)

Figure 5.16. Semi-log plot of mixing parameters for varying Fr at $\alpha = 3.35\%$ (a) COX number (b) Diapycnal eddy diffusivity (non-dimensionalized by $15cm^2/s$) (c) Normalized viscous dissipation

Figure 5.16 shows that, as Froude number increases (i.e., the strength of stratification decreases), the mixing quantities once again reach a statistically steady state with time. The time-averaged quantities are plotted in figures 5.17d-f. In this study, the stratification is controlled by the thermal expansion coefficient, γ, while the background temperature gradient is not changed. Since the COX number quantifies the temperature gradient in the liquid, it does not change much with a change in the Froude number when we retain the same initial temperature profile. The only change we see is due to the turbulent transport of temperature due to fluctuations, which increases as we weaken the stratification. In the case of the eddy diffusivity, a change in γ produces a linear change in N^2 and also a linear change in the density perturbation in the background fluid. This leads to an increase in the eddy diffusivity with an increase in Fr. The increase in eddy diffusivity as the strength of the stratification decreases happens because, at high stratifications, the isopycnals come back to their stable state

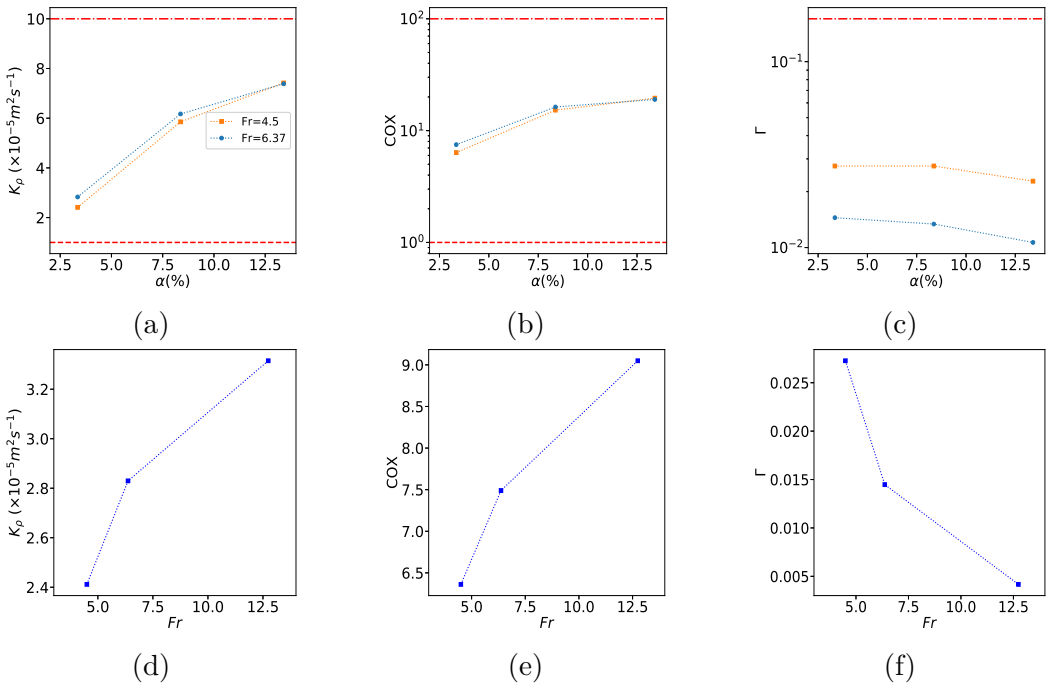

Figure 5.17. Time averaged (a,d) Diapycnal eddy diffusivity (b,e) COX number (c,f) Mixing efficiency, plotted against α for two different Froude numbers and plotted against Fr for $\alpha = 3.35\%$ respectively. Red $--$ and $-\cdot-$ correspond to lower and upper bounds respectively predicted by [45] in (a), [48] in (b) and (c)

before thermal diffusion can take place. This is because the force pulling the disturbed isopycnal back to its stable state is high, which is also reflected in a high buoyancy frequency. As the strength of stratification decreases, time taken to come back to the original state increases (since the buoyancy frequency is lower), and this facilitates thermal diffusion, enhancing mixing. Since the mixing efficiency increases with an increase in the stratification strength, it can be inferred that the percentage of the total energy lost to buoyancy increases as stratification increases. In a nearly homogeneous fluid, mixing efficiency is almost zero. This is because the fluctuations mix fluids of the same density [46]. Even though the vertical mass flux at higher Froude numbers is more leading to more thermal diffusion, the stratification is weak to begin with. Thus, the extent of homogeneity compared to the original state is less, since we start with a more mixed fluid. Mathematically, we can see that the mixing efficiency is governed by the competing effect of the buoyancy flux and the viscous dissipation. Even though

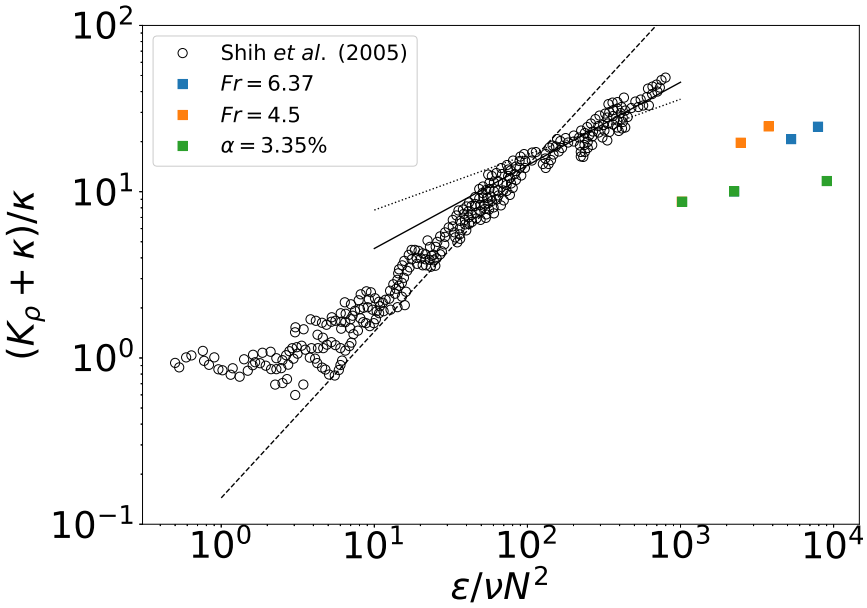

Figure 5.18. Total scalar diffusivity normalized by molecular diffusivity versus the normalized viscous dissipation. Fit to data taken from [48]: $--$, $(K_\rho + \kappa)/\kappa = 0.2Pr\epsilon/\nu N^2$; $\cdot\ \cdot\ \cdot$, $(K_\rho + \kappa)/\kappa = 5Pr(\epsilon/\nu N^2)^{1/3}$; —, $(K_\rho + \kappa)/\kappa = 2Pr(\epsilon/\nu N^2)^{1/2}$

the eddy diffusivity is increasing as we weaken the stratification, the buoyancy frequency is decreasing. Since the numerator of Γ is simply $K_\rho N^2$, the competing effects explained previously cancel out. The increase in viscous dissipation (figure 5.16c) is, thus, directly translated into a decrease in Γ.

Discussion and Scaling

Eddy diffusivity due to turbulent activities in the ocean was estimated by Moum and Osborn [50]. They observe that for depths $\approx$ 900m, $K_\rho < 10^{-5}\ m^2 s^{-1}$, for depths less than 2000m, $K_\rho < 5 \times 10^{-5}\ m^2 s^{-1}$ and the deep estimate for K_ρ approaches a value of $10^{-4}\ m^2 s^{-1}$. The lower and upper bounds of the diapycnal eddy diffusivity have been plotted in figure 5.17a. Similarly, the range of COX numbers in the central North Pacific region were found to vary between 10^0 and 2×10^2 by Gregg [45]. They also found that the most intense activity occurs above and below the main thermocline. Once again, we plot the upper and lower bounds in figure 5.17b and find that our values

lie within these bounds. Mixing efficiency in oceanography is of the order of 0.17-0.2 [48]. We have plotted the lower bound in figure 5.17c. Mixing efficiency levels present in the ocean scales due to turbulence is not achieved here. The COX number and mixing efficiency variation with α are plotted on a semi-log scale (figure 5.17b,c) so that the upper and lower bounds can be incorporated in the same plot.

Experiments on stably stratified grid turbulence have suggested that K_ρ can be expressed in terms of $\epsilon/\nu N^2$, where ϵ is the viscous dissipation [48]. Shih et. al. [48] examined these results for homogeneous shear stratified turbulence and find the scaling between K_ρ and $\epsilon/\nu N^2$. They found that the calculated K_ρ values collapsed very well over the entire range of $\epsilon/\nu N^2$. A plot of K_ρ versus $\epsilon/\nu N^2$ is shown in figure 5.18 where we collapse all our data along with the data from [48]. We find that we are able to achieve similar levels of eddy diffusivity as shear induced turbulence, although it is important to note that we use stronger levels of stratification ($N \approx O(10^0)$). The mixing due to motion of confined bubbles can generate eddy diffusivities as strong as turbulent mixing, but it occurs at much larger values of energy dissipation compared to turbulent mixing. The eddy diffusivity values could be higher for unbounded cases. From figure 5.18, we can see clearly that the scaling of eddy diffusivity obtained for turbulent mixing is not applicable for our data.

In order to further quantify mixing and how it is affected by the bubble dynamics, we look the scaling of the diapycnal eddy diffusivity with average bubble velocity fluctuations, $v_b'^2$, which is defined as

$$\overline{v_b'^2} = \overline{\left(v_b^{(\mathrm{i})} - \left\langle v_b^{(\mathrm{i})} \right\rangle\right)^2} \tag{5.9}$$

where the overbar refers to averaging over time and also over the bubbles. We collapse all the cases of void fractions and Froude numbers, as shown in figure 5.19.

We see that as the vertical bubble velocity fluctuations increase, the diapycnal mixing also increases, while at high values of fluctuations, it starts to plateau. Another interesting observation from this figure is that at the two lower void fractions, an increase in Fr leads to an increase in both the bubble fluctuations and the eddy

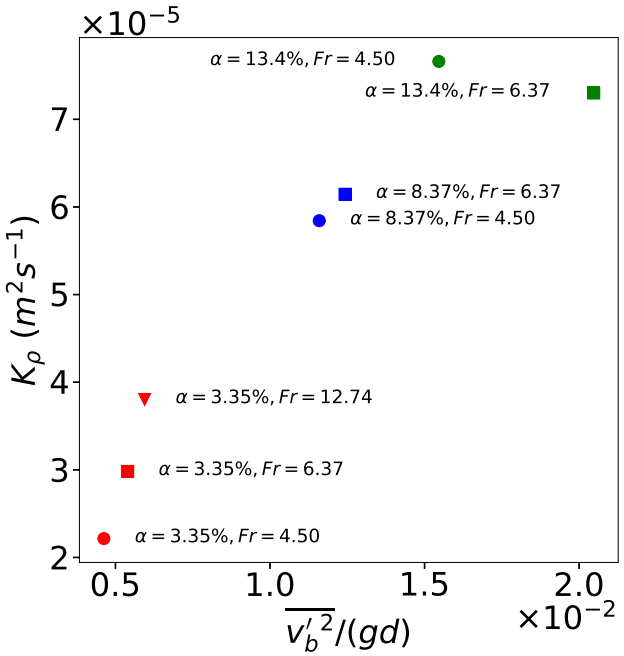

Figure 5.19. Variation of K_ρ with bubble velocity fluctuations. Same colors correspond to same α. Same shapes correspond to same Fr

diffusivity. At the highest void fraction, we see that the fluctuation increases with Fr, but K_ρ has attained a plateau. We also see that at a constant Fr, increasing α increases the fluctuation and the mixing monotonically.

Another way to visually observe mixing is to look at stratification levels once the bubble plume has repeatedly passed through the domain (5.20b). The unique vortical wake structures can also be visualized by studying the diffusion of a passive scalar with low molecular diffusivity (5.20a). This is done by introducing a circular patch of the passive scalar at a time when the flow has reached steady state and letting the bubbles pass through the dye. The concentrations are characterized by thin, stretched structures, which are curved by the velocity field near the bubbles.

5.4 Summary

The bubble dynamics and mixing induced in stratified fluids by the bubble motion in a Hele-Shaw cell have been studied. The confinement keeps turbulence at bay, and thus the mixing produced primarily due to transport by the bubble wake is studied.

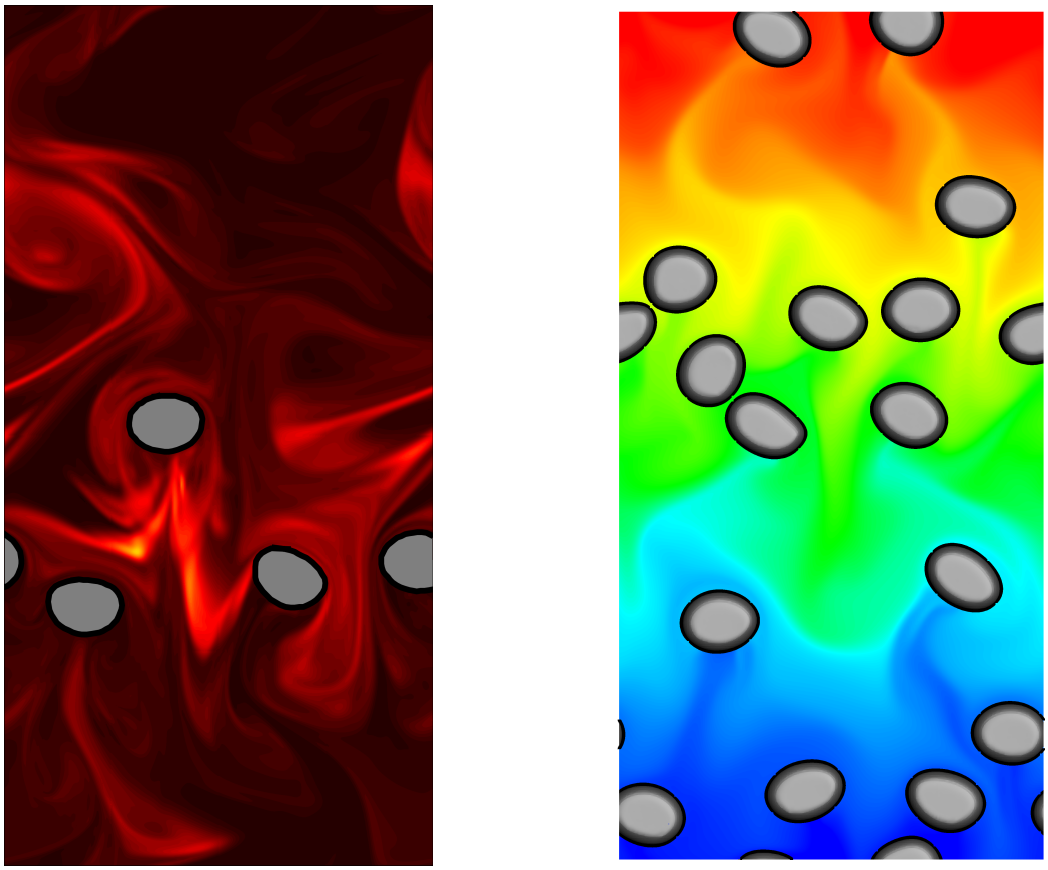

(a) (b)

Figure 5.20. (a) Contours of concentration of low-diffusive passive scalar for $\alpha = 3.35\%$.(b) Temperature contours for $\alpha = 8.37\%$

The trends observed in the rise velocity for different void fractions are different in the confined environment compared to the unconfined case. The bubbles are seen to follow a zigzag motion due to the periodic vortex shedding. The zigzag motion has been quantified by looking at the trajectories and autocorrelation of the horizontal bubble velocity. Formation and subsequent breakup of clusters are observed. The size of these clusters has been quantified by the cluster size index, and this index is directly correlated to the instantaneous Reynolds number of the bubbles. An increase in the cluster size results in an instantaneous rise in the bubble Reynolds number. Mixing induced by the bubbles in stratified fluids is quantified through the COX number, diapycnal eddy diffusivity, and mixing efficiency. It is seen that as α increases, the buoyancy flux across the pycnoclines also increases, giving rise to a better mixed fluid. When the stratification strength is increased, the fraction of total energy lost to buoyancy increases while the cross isopycnal diffusion decreases. Dependence of diapycnal eddy diffusivity on the bubble velocity fluctuations is also studied.

6. BUBBLE INDUCED LIQUID DYNAMICS IN UNBOUNDED STRATIFIED FLUIDS

6.1 Literature Review

A comprehensive study of bubble motion and resulting liquid agitation has been made in literature [39], [51], [36]. However, in order to study mixing characteristics in stratified fluids, we also need an understanding of how stratification affects the bubble dynamics and vice versa. It has been observed that stratification suppresses the vertical and horizontal velocities and velocity fluctuations of drops, which in turn lead to formation of horizontal clusters [27], [25], [26]. Drop deformation is also suppressed by strong stratification [5], [27]. Bayareh et. al. [5] observed that a single drop rising in a stratified medium experiences drag enhancement compared to a homogeneous fluid and thus the travel time of a drop of crude oil increases by 7% in moderate stratification. They also report the formation of secondary vortex and resulting buoyant jet. In the study of rise of two drops in a linearly stratified fluid [27], drop configuration is retained for the in-line configuration in contrast to the drafting-kissing-tumbling behavior in a homogeneous fluid. Díaz-Damacillo et. al. [29] experimentally investigated the rising motion of a single bubble across two different-density liquids. They report that for larger bubbles, the drift volume becomes unstable and detaches from the bubble due to path instabilities of bubble. This results in dense fluid patches in the lighter fluid, leading to mixing between the two layers.

Although bubble induced mixing can happen either due to transport by bubble wake or due to turbulent dispersion, it is seen that in homogeneous unbounded systems, the latter plays a major role [18]. The pseudoturbulence generated by bubble motion has been quantified previously in various studies [52], [53], [54], [55], [56]. Lance and Bataille [57] have extensively studied the turbulence in the liquid phase of a bubbly air-water flow experimentally. They observe that for $\alpha < 1\%$, the turbulent kinetic energy (TKE) of the liquid is a linear sum of TKE due to grid generated turbulence and bubble-induced turbulence. When $\alpha > 1\%$, TKE is amplified even more due to hydrodynamic interactions between bubbles. They report that the classical -5/3 power

law of the 1D spectra is replaced by another power law of exponent -8/3 when bubble void fraction increases. Martínez-Mercado et. al. [52] have shown that the pseudoturbulence intensity increases almost linearly as α increases, while bubble velocity fluctuation stagnates for $\alpha > 0.02$. Riboux et. al. [58] have decomposed the liquid fluctuation in bubbly flows into a spatial part and a temporal part and have shown that the temporal part increases faster than the spatial part at higher α values. This results in the reduction of asymmetry in the probability density function of velocity fluctuation as α increases, since the asymmetry arises from the spatial fluctuation (wake contribution). The liquid fluctuations are also dependent on the deformability of the bubbles. The vertical velocity variance is higher for the deformable system than the nearly spherical system, with the anisotropy also following the same trend [53]. In their study of bubble motion in a periodic box, Smereka [59] have shown that bubbles tend to form horizontal clusters when the bubble velocity variance is low. However, this tendency reduces if the bubble velocity and consequently the liquid velocity variance is large [59], [37].

Although the number of studies involving bubble motion and bubble induced turbulence are aplenty, we find that there is still a dearth of studies focusing on characterizing the mixing mechanisms in stratified fluids due to the pseudo-turbulence. In this study, we will attempt to characterize the motion of bubble in unbounded stratified liquids and study the induced mixing due to bubble-induced turbulence. We explore a wide range of parameters including void fraction, Froude number, Reynolds and Eötvös numbers. Bubble dynamics including bubble dispersion, microstructure and bubble velocity fluctuations and correlations will be studied. Mixing induced will be analyzed through TKE levels, liquid fluctuations, flow visualizations and mixing efficiencies.

6.2 Problem Description

We perform fully resolved direct numerical simulations of up to 146 bubbles in the unbounded stratified domain. Our problem of interest is solved numerically through the continuity, momentum and energy conservation equations.

The velocity in the domain is periodic in all directions. Temperature on the other hand, is periodic only in the two horizontal directions. In order to maintain the linear temperature gradient in the vertical direction, we apply the periodic boundary condition on temperature perturbation, T_m. T_m is the perturbation from linearity given by $T_m = T - \frac{dT}{dx}x$, where $\frac{dT}{dx}$ is the constant, imposed temperature gradient.

The important non-dimensional numbers for the study and their ranges are given here. Reynolds number based on the bubble velocity, $Re = \rho\sqrt{gd}d/\mu_l$ varies between 25 and 200 and *Eötvös* number, $Eo = (\rho_l - \rho_b)gd^2/\sigma$ ranges from 1.55 to 4.95. The variation of Re and Eo lead to bubble path instabilities leading to different levels of mixing. Here ρ_l and ρ_b are the densities of liquid and bubble, respectively and d is the bubble diameter. The other dimensionless parameters include the Froude number, $Fr = V_0/(Nd)$ varied between 9.96 and 28 and void fraction $\alpha = \frac{1}{6}N_b\pi d^3/(LBW)$ varied in the range 3.66% to 7.64%. $N = \sqrt{\beta g/\rho_\circ}$ is the buoyancy frequency which gives the frequency of oscillation of a disturbed isopycnal, where β is the density gradient in the domain. L, B, W are the dimensions of the domain. The density and viscosity ratios are kept constant at $\rho_l/\rho_b = 100$ and $\mu_l/\mu_b = 10$.

Our objective is to investigate the bubble and liquid dynamics in the rise of bubbles in temperature stratified Newtonian fluids. We explore a wide range of parameters, to find the physical conditions under which background mixing is enhanced. We analyze the bubble dynamics by studying the rise velocity and velocity fluctuations of the bubbles. We quantify both the temporal and spatial fluctuations and interpret their significance. We characterize bubble dispersion through the dispersion coefficient, and visualize the flow. Likewise, we quantify the liquid agitation and background mixing by looking at turbulent kinetic energy levels and also the mixing parameters.

6.3 Results and Discussion

The results are organized as follows. First, we will look at domain size independence and discuss the meshing of the computational domain. Subsequently, we will discuss the mixing induced in the liquid by looking at parameters including diapycnal eddy

diffusivity, mixing efficiency and Cox number. We then discuss the bubble dynamics by studying bubble rise velocities, velocity fluctuations, temporal bubble velocity correlations, bubble dispersion and pair probability distributions. The bubble dynamics are used to explain trends and anomalies in thermal mixing behaviors. We also visualize the flow field and study the flow pattern around bubbles in order to explain the mixing results. This is followed by a discussion on liquid agitation, including liquid velocity fluctuations and turbulent kinetic energy spectra, to give a comprehensive analysis of bubble and liquid dynamics. In this study we will be varying several parameters to study their impact, namely, the void fraction, α, Froude number, Fr, initial Reynolds number, Re, and *Eötvös* number, Eo. List of simulated cases is given in table 6.1. In the study of void fraction variation, Fr, Re and Eo are kept constant at $14.1, 44$ and 1.55, respectively. In the Froude number study, α, Re and Eo are kept constant at $5.86\%, 44$ and 1.55, respectively. When Re and Eo are varied, α and Fr are fixed at 3.66% and 14.1, respectively.

6.3.1 Computational Domain and Mesh size

In order to establish that the chosen domain size is long enough, we look at the spatial liquid velocity autocorrelation in the vertical and the two horizontal directions. The autocorrelation is defined as

$$R_{ux}(r_x) = \frac{\langle u_l'(x,y,z)u_l'(x+r_x,y,z)\rangle}{\langle (u_l'^2(x,y,z))\rangle}, \tag{6.1}$$

where u_l' is the vertical velocity of the liquid and $\langle\rangle$ refers to ensemble averaging. This has been used in many turbulence simulations to determine the optimal length of the domain. Since we have a periodic domain in all directions, we expect the spatial autocorrelation to die out at the the mid-point in every direction. In a periodic domain, the first and last points are 100% correlated. Beyond the mid-point, we expect the correlation to increase back up. We thus look at the correlations only till the mid-point in all directions. We plot the spatial autocorrelation of each velocity component (u, v, w) in directions (x, y) in figure 6.1. The two horizontal directions y and z are

Table 6.1. List of cases simulated

$\alpha\%$	Fr	Re	Eo
3.66	14.1	44	1.55
5.86	14.1	44	1.55
7.64	14.1	44	1.55
5.86	9.96	44	1.55
5.86	28.17	44	1.55
3.66	14.1	25	1.55
3.66	14.1	74	1.55
3.66	14.1	100	1.55
3.66	14.1	200	1.55
3.66	14.1	25	2.48
3.66	14.1	44	2.48
3.66	14.1	74	2.48
3.66	14.1	100	2.48
3.66	14.1	200	2.48
3.66	14.1	25	3.3
3.66	14.1	44	3.3
3.66	14.1	74	3.3
3.66	14.1	100	3.3
3.66	14.1	200	3.3
3.66	14.1	25	4.95
3.66	14.1	44	4.95
3.66	14.1	74	4.95
3.66	14.1	100	4.95
3.66	14.1	200	4.95

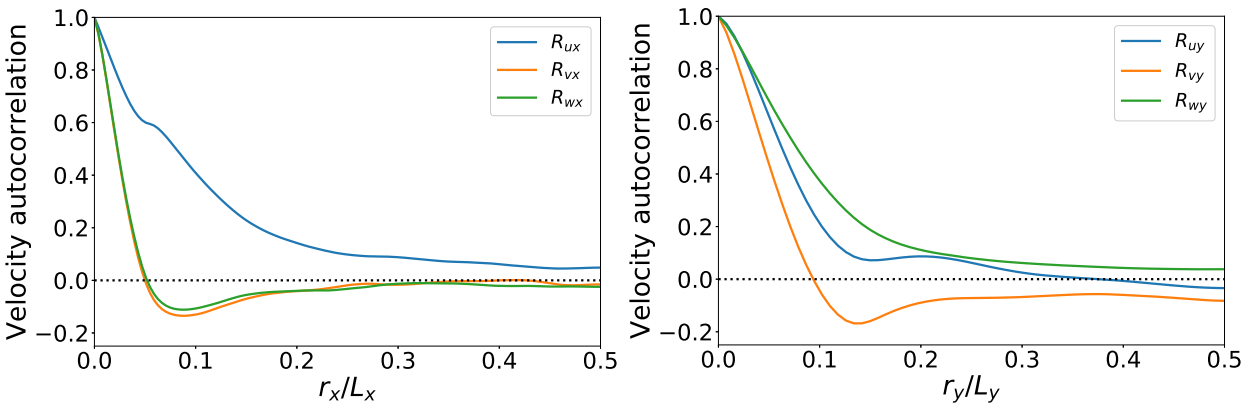

(a) (b)

Figure 6.1. Spatial velocity autocorrelation for the domain in the Vertical (a) and horizontal (b) directions for $\alpha = 5.86\%, Fr = 14.1$

isotropic. For the domain length we consider, the velocities get uncorrelated at the mid-point of the domain in each direction as expected. We thus conclude that the domain length ($16d \times 8d \times 8d$) is long enough.

We use a uniform mesh, $256 \times 128 \times 128$ for Re up to 100 and we double the points in every direction for $Re = 200$. For these cases we have 16 and 32 points across the bubble diameter, respectively. We find that the grid size is sufficient to resolve the momentum (δ_m) and thermal (δ_t) boundary layers on the bubble. The thickness can also be numerically estimated as $\delta_m \sim \mathcal{O}(d/\sqrt{Re})$ and $\delta_t \sim \mathcal{O}(d/\sqrt{Re \cdot Pr})$ [60]. Both the boundary layers are resolved if we use this definition as well.

6.3.2 Mixing

The liquid velocity fluctuations caused due to bubble motion are responsible for irreversible mixing in the background liquid. In the stratified liquid, when two different density liquids are stirred due to the bubble motion, thermal diffusion takes place leading to thermal mixing. The motion of bubbles through the isopycnals causes displacement of the density line from its stable state. The displaced isopycnal experiences a negative buoyancy force back towards its stable state. This restoring force causes the isopycnal to oscillate about the stable state with a frequency of N. The time taken for these oscillations to die out scales as $1/N$. Repeated motion of bubbles through the liquid causes the isopycnals to take longer to come back to the stable level, facilitating thermal mixing. There are two important mechanisms of mixing due to bubble motion. The first is the transport of liquid by capture within bubble wakes and the second is due to bubble induced turbulent dispersion. It has been shown that whereas in a confined geometry, mixing happens through the former way [19], [17], in an unbounded domain, the main mixing mechanism is the latter [18]. We characterize the background mixing with three parameters, namely the mixing efficiency (Γ), the diapycnal eddy diffusivity (K_ρ) and the Cox number.

The fundamental definition of mixing efficiency [61] is given by

$$\Gamma = \frac{\text{Change in background potential energy}}{\text{Total expended energy}}. \tag{6.2}$$

This is also known as the flux Richardson number. In a stratified fluid, if we can find the buoyancy flux and viscous dissipation in the flow we can define Γ as [48], [46]

$$\Gamma = \frac{-g\langle\rho' u'\rangle}{-g\langle\rho' u'\rangle + 2\mu\langle E : E\rangle}, \tag{6.3}$$

where E represents the strain rate tensor term. The denominator denotes the sum of the viscous dissipation and the loss to buoyancy. In a general sense the denominator represents the net supply of TKE to sustain turbulent motions in a statistically steady state. Thus, Γ essentially gives the efficiency with which the energy input is converted to buoyancy flux [47]. The energy input in this case is the disturbance induced by the motion of bubbles. In order to draw a parallel with a truly turbulent case, we can think of a parallel shear flow case where there is a balance between production ($\overline{u_i' u_j'}\frac{\partial \overline{u}_i}{\partial x_j}$), the dissipation ($2\nu\overline{E_{ij}E_{ij}}$) and the work against buoyancy ($\frac{\overline{u'\rho' g}}{\bar{\rho}}$) as was done in [43]. There is viscous dissipation in every direction but a loss to buoyancy only in the vertical component, due to which we have very low values of the mixing efficiency. Typical value of mixing efficiency in the ocean scale in a turbulent mixing event is approximately $\Gamma \sim 0.17$ [43].

Diapycnal eddy diffusivity gives the vertical mass flux or the cross isopycnal diffusion, and was defined by [43] as

$$K_\rho = -\frac{g\langle\rho' u'\rangle}{\rho_\circ N^2}, \tag{6.4}$$

where the $\langle\cdot\rangle$ represents an ensemble average. This is obtained much similar to eddy viscosity, by assuming $\langle\rho' u'\rangle = K_\rho \frac{d\langle\rho\rangle}{dx}$. This term helps quantify the amount of work done by the buoyancy force. It gives a measure of vertical transport and diffusion of density layers due to the bubble induced velocity fluctuations. Since the diapycnal eddy

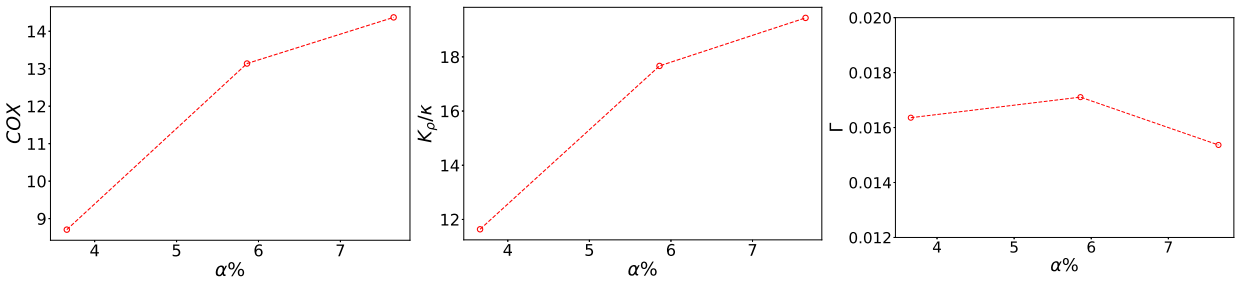

(a) (b) (c)

Figure 6.2. Mixing parameters (a) COX number (b) Diapycnal eddy diffusivity (c) Mixing efficiency as a function of α for $Fr = 14.1, Re = 44, Eo = 1.55$

diffusivity is a dimensional quantity, we normalize it with the molecular diffusivity in our results.

In order to quantify the temperature microstructure at the thermocline, we use the Cox number defined as [44], [45], [62]

$$COX = \frac{\langle (\frac{\partial T'}{\partial x})^2 + (\frac{\partial T'}{\partial y})^2 + (\frac{\partial T'}{\partial z})^2 \rangle}{\left(\frac{\partial \langle T \rangle}{\partial x}\right)^2}, \tag{6.5}$$

which gives the variance of the temperature gradient averaged over all directions normalized by the mean temperature gradient in the vertical direction due to the stratification. The vertical stratification is linear and thus the denominator of the Cox number just remains a constant in this case. We are thus effectively looking at the average variation of temperature from linear stratification due to background fluctuations.The temperature microstructure is mainly caused due to the motion of bubbles and subsequent disturbance of thermoclines followed by thermal diffusion.

Effect of void fraction

For the given computational domain size, we test the effect of void fraction on mixing by changing the number of bubbles in the domain, while keeping the size of the bubbles constant. Figure 6.2 shows the variation of time averaged mixing quantities at a constant Froude number of 14.1. The time averaging is performed once the flow

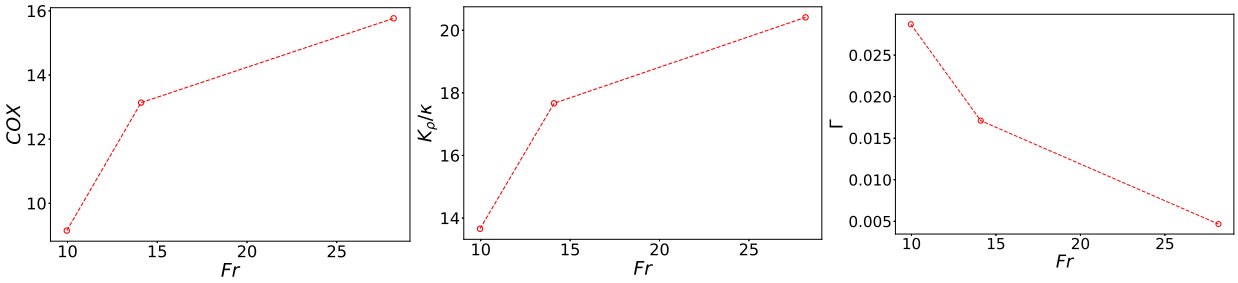

(a) (b) (c)

Figure 6.3. Mixing parameters (a) COX number (b) Diapycnal eddy diffusivity (c) Mixing efficiency as a function of Fr for $\alpha = 5.86\%$, $Re = 44$, $Eo = 1.55$

reaches a quasi steady state, by omitting the initial transient phase. Figure 6.2a, b show that the Cox number and the diapycnal eddy diffusivity show a similar increasing trend with an increase in α. An increase in α increases the variation of temperature gradient improving the thermal homogeneity of the liquid. This is because a higher number of bubbles leads to a higher vertical buoyancy flux. On the other hand, the mixing efficiency stays more or less constant for a change in α (figure 6.2c). The increase in the number of bubbles leads to a higher vertical mass transport, but simultaneously gives rise to a higher input of energy into the system. From the definition of Γ, this leads to an increase of both the numerator and denominator with an increase in α, thus nullifying their effects. It should be noted that [18] did a similar study for non-stratified liquid where they study mixing by calculating the diffusion of a low-diffusivity dye. They observe a similar rise in vertical diffusion coefficient for the range of α considered here. The trend in the vertical diffusion coefficient that they observe can be compared to the evolution of the diapycnal eddy diffusivity. They also conclude that at void fractions higher than 7%, the diffusion coefficient starts to stagnate. We note that even though the liquid fluctuations in our domain are steadily increasing with α (figure 6.15a), the increase of K_ρ between $\alpha = 5.68\%$ to $\alpha = 7.64\%$ is not as sharp as the rise between $\alpha = 3.66\%$ and $\alpha = 5.68\%$.

Effect of Stratification

Stratification in the liquid is controlled by the Froude number. An increase in Froude number signifies a decrease in the buoyancy frequency and a corresponding decrease in stratification strength. We change the stratification by changing the thermal expansion coefficient of the liquid while the temperature gradient is kept constant. Thus, the variance in temperature gradient or the Cox number is a good way to measure the background mixing. We see in figure 6.3a that a decrease in stratification leads to an increase in Cox number. The buoyancy flux also increases as we relax the stratification as can be seen in the diapycnal eddy diffusivity plot in figure 6.3b. This can be explained by noting that at strong stratifications, the resistance of the isopycnals to disturbances is higher because of which vertical mass transport is lower. The negative buoyancy experienced by the displaced isopycnal is higher in magnitude at these low Froude numbers. As Fr increases, the buoyancy frequency reduces, which gives more time for thermal mixing to take place. The mixing efficiency decreases as stratification decreases (figure 6.3c). This happens because, as explained previously, the energy input to the system is increasing with Fr due to more liquid fluctuations. We can also interpret the mixing efficiency as a measure of liquid homogeneity compared to the initial state. At large Froude numbers the liquid is quite homogeneous to begin with and thus mixing efficiency is low and will go to zero for a non-stratified liquid, by definition.

Effect of *Eötvös* and Reynolds numbers

An increase in Eo indicates higher bubble deformability. The bubbles have a spheroidal shape and are flattened in the direction of motion. This leads to path instabilities in the bubble motion, which has the potential to increase the background mixing. We see an almost monotonic increase in the Cox number and diapycnal eddy diffusivity with increase in Eo at different constant Reynolds numbers (see figure 6.4a, b). For $Re = 25$, the mixing parameters seem to stagnate at high Eo. Mixing efficiency also increases with an increase in Eo (see figure 6.4c) and the trend is similar to the

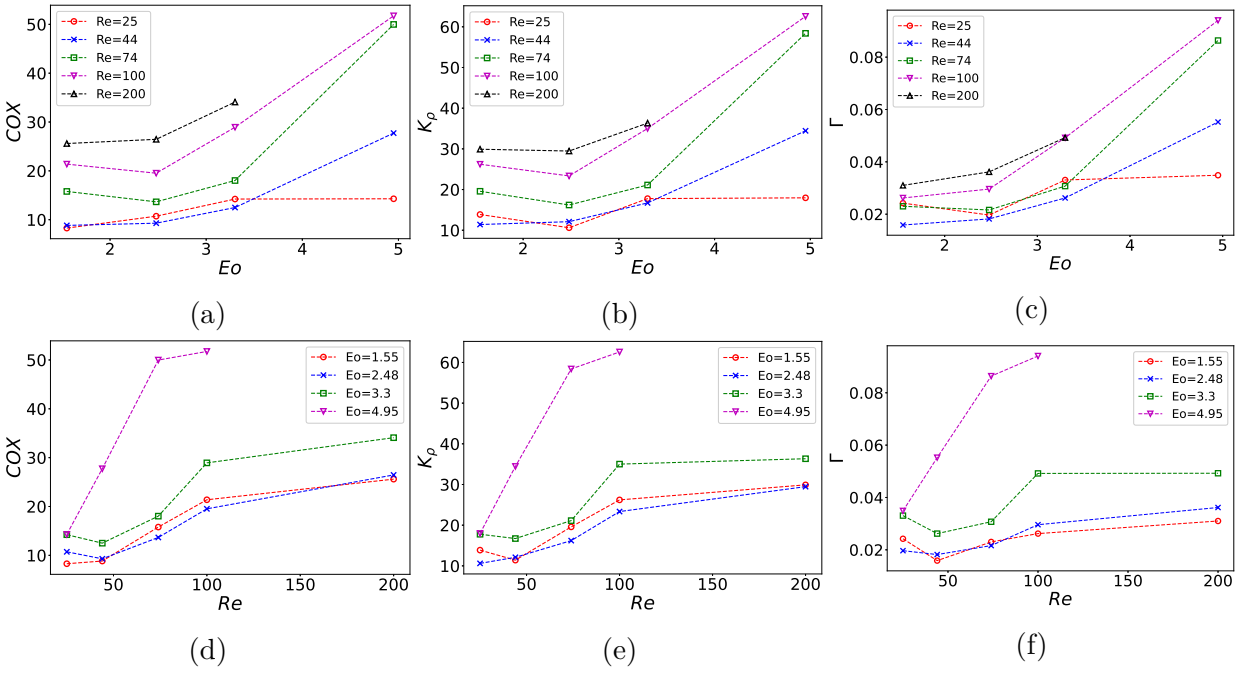

Figure 6.4. Mixing parameters (a,d) COX number (b,e) Diapycnal eddy diffusivity (c,f) Mixing efficiency as a function of (a,b,c) Eo and (d,e,f) Re at constant $\alpha = 3.66\%$ and $Fr = 14.1$

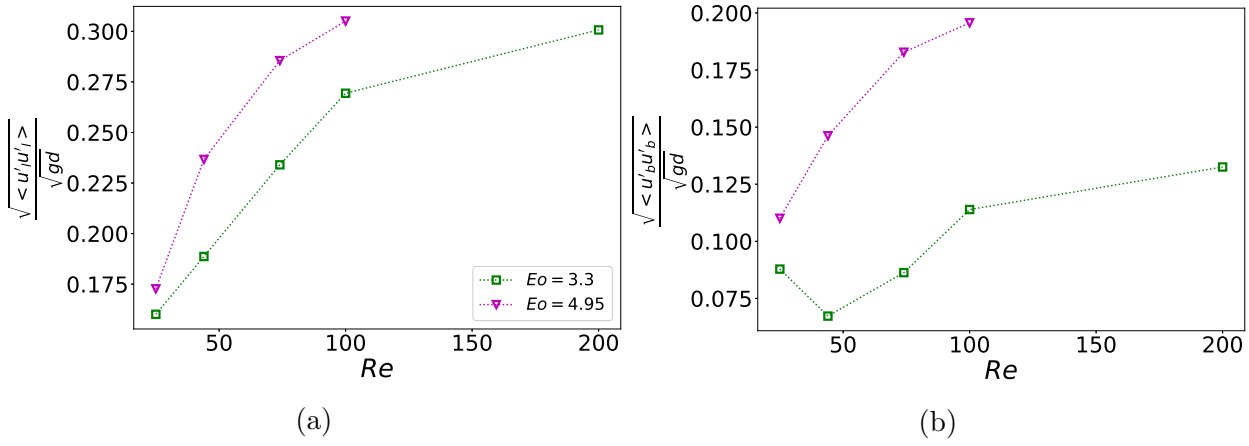

Figure 6.5. (a) Liquid velocity fluctuations (b) Bubble velocity fluctuations at constant $\alpha = 3.66\%$ and $Fr = 14.1$

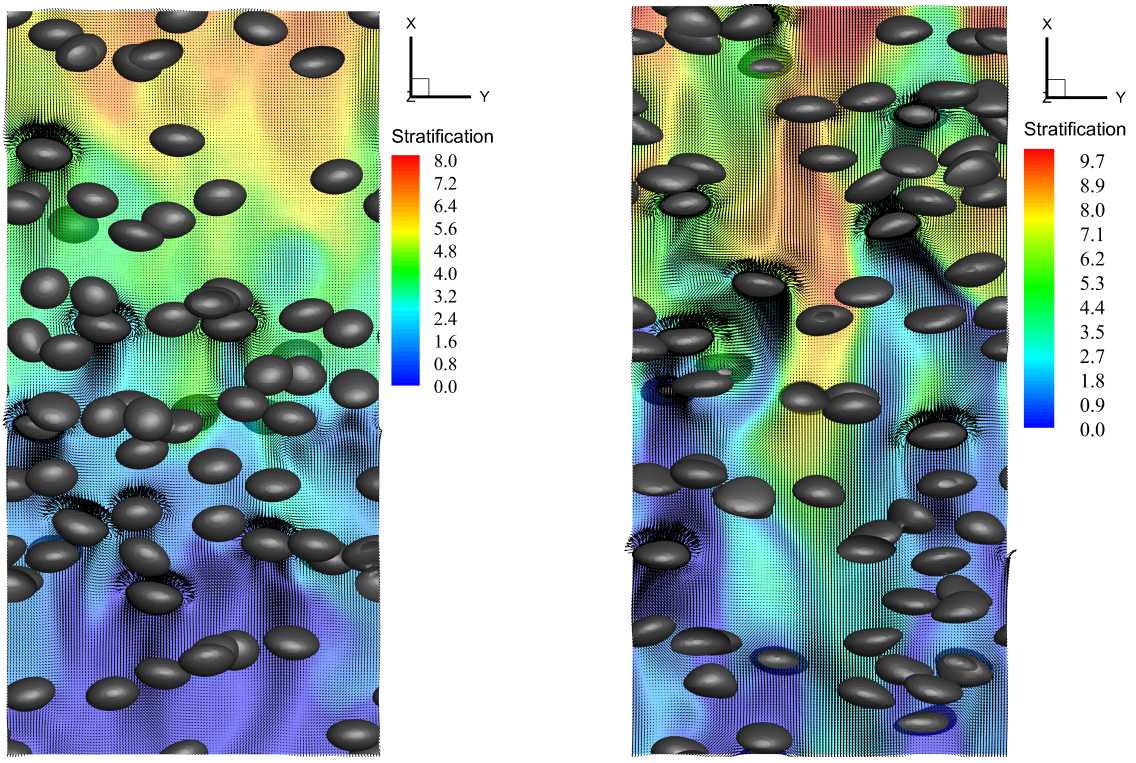

(a) (b)

Figure 6.6. Temperature stratification at $alpha = 3.66\%, Fr = 14.1, \mathrm{Re} = 100$ and $Eo =$ (a) 1.55, (b) 4.95 at $t^* = 50$

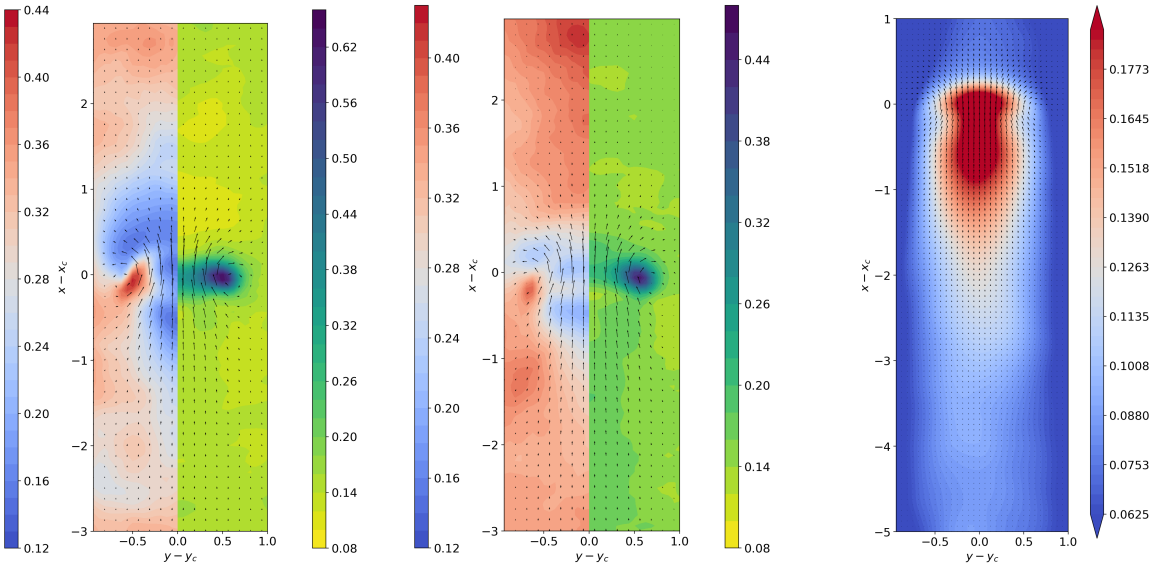

Figure 6.7. Velocity fluctuations normalized by $(gd)^{1/2}$ (left:u and right:v) near bubbles at $\alpha = 3.66\%, Fr = 14.1, Re = 100$ and $Eo =$ (a) 1.55, (b) 4.95. (c): Temperature perturbation near bubble averaged over all bubbles normalized by T_{max} for $Eo = 4.95$. Vectors show average velocity field

trend in K_ρ. This leads to the conclusion that the change in Eo is not producing a change in the energy production in the system. One interesting observation we can make from figure 6.4c is that the curves of constant Re are close together at low Eo while at the highest $Eo = 4.95$, the curves diverge to very different values.

Comparing our results with the ones obtained for the rise of bubbles in a thin gap [17], we see that the unbounded domain gives rise to much larger values K_ρ (figure 6.4b) for a much lesser Reynolds number of 200. The effect of bubble induced turbulent dispersion, which is absent in a Hele-Shaw cell, is seen to produce more thermal mixing than transport in the wake. This was an expected result, since the bubble wake is highly attenuated and the liquid fluctuations are limited to the bubble vicinity in case of a confined domain. The unconfined domain also gives rise to a free, unrestricted rise of bubbles, while the motion in the wall normal direction is restricted in the confined case.

An increase in Re leads to increase in the Cox number, K_ρ as well as Γ (figure 6.4). This trend is most pronounced for the highest Eo of 4.95. This could possibly be attributed to the much higher levels of bubble dispersion in the vertical direction for $Eo = 4.95$ compared to $Eo = 3.3$, which we will discuss in a later section. Higher vertical dispersion can be related to a more asynchronous relative bubble motion leading to more thermal diffusion in the liquid. The mixing parameters are sensitive to Eo especially nearer to bubble breakup values of Eo. Even at a low $Re = 44$, the value of $\Gamma \sim 0.058$ for $Eo = 4.95$. The trend in mixing efficiency and eddy diffusivity can also be explained by looking at averaged liquid and bubble velocity fluctuations normalized by $\sqrt{gd}$ (figure 6.5). The bubble and liquid fluctuations are increasing monotonically for $Eo = 4.95$. For $Eo = 3.3$, we see a drop in $< u_b' u_b' >$ from $Re = 25$ to $Re = 44$. There is then a steady rise and finally saturation near $Re = 200$. This trend could explain the stark difference in variation in mixing as a function of Re at these two Eo. This shows that bubble fluctuations and bubble interactions play a huge role in liquid mixing.

Figure 6.6 shows the flow field at $t^* = 50$. A single slice with the temperature contours and velocity field is portrayed, along with the bubble locations at $Re = 100$ for $Eo = 1.55$ and $Eo = 4.95$. A noticeable difference between the two cases is seen in the bubble wake by observing the velocity field around the bubbles. For the lower Eo (figure 6.6a), we see that the path of the bubbles is mostly rectilinear which is evident from the wake of the bubble shown by both the velocity vector and the pattern of stratification. For a higher Eo, the bubbles show path instabilities causing the pycnoclines to be disrupted in a zigzag manner. This behavior promotes mixing properties, reflected in the trend in mixing parameters (see figure 6.4). The temperature stratification shows more homogeneity at $Eo = 4.95$ indicating higher mixing levels.

The difference in flow around bubbles is better depicted by plotting the average domain velocity vector and contour of vertical and horizontal fluctuation velocity (see figure 6.7). The velocity field around the bubbles is averaged over time and all bubbles by assuming the relative location of all bubbles to be at the origin. The fluctuation is obtained by calculating the root mean squared value of velocity fluctuation around each

bubble and then averaging over time in steady state. Vertical velocity shows higher fluctuations around the bubble for $Eo = 4.95$, which plays a key role in determining the mixing rate. The average temperature perturbation around bubbles is also shown in figure 6.7c. The maximum perturbation occurs around the bubble and in its wake.

6.3.3 Bubble rise velocities

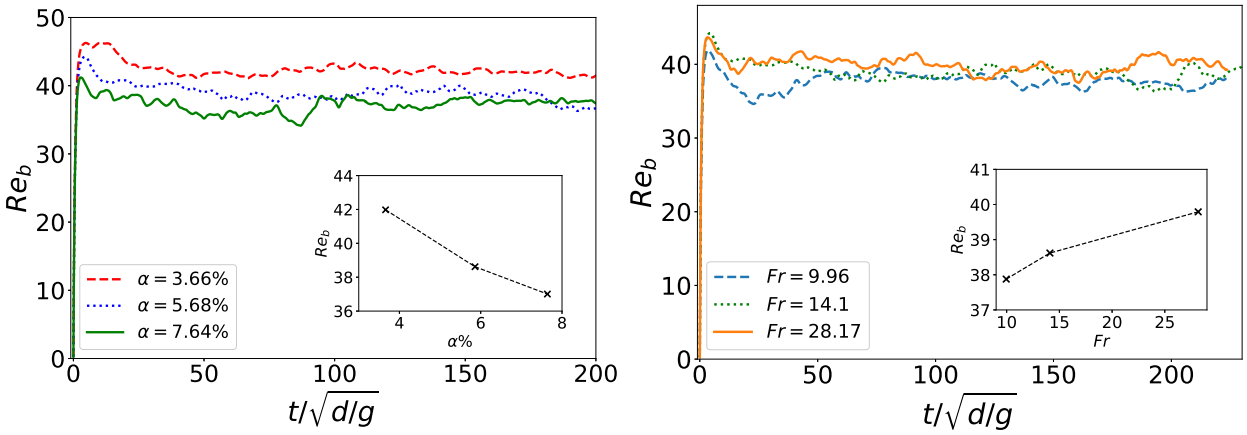

(a) (b)

Figure 6.8. Bubble rise Reynolds number at constant $Re = 44$ and $Eo = 1.55$ as a function of (a) void fraction at $Fr = 14.1$ and (b) Froude number at $\alpha = 5.86\%$

The slip velocity of the bubble swarm is calculated as

$$u_b(t) = \frac{1}{N_b}\sum_{i=1}^{N_b} u_{b,i}(t) - u_f(t), \tag{6.6}$$

where $u_{b,i}(t)$ stands for the instantaneous vertical velocity of the ith bubble and $u_f(t)$ is the average liquid velocity. The steady-state average rise velocity of the bubble swarm is obtained by

$$u_{b,avg} = \frac{1}{T - t_0}\int_{t_0}^{T} u_b(t)dt, \tag{6.7}$$

where the time interval $T - t_0$ is chosen such that the velocity of the swarm has crossed the transient stage and is at a statistically steady state. The bubble rise Reynolds numbers are calculated as $Re_b = \rho_l u_b d/\mu_l$. Figures 6.8 and 6.9 show both the time

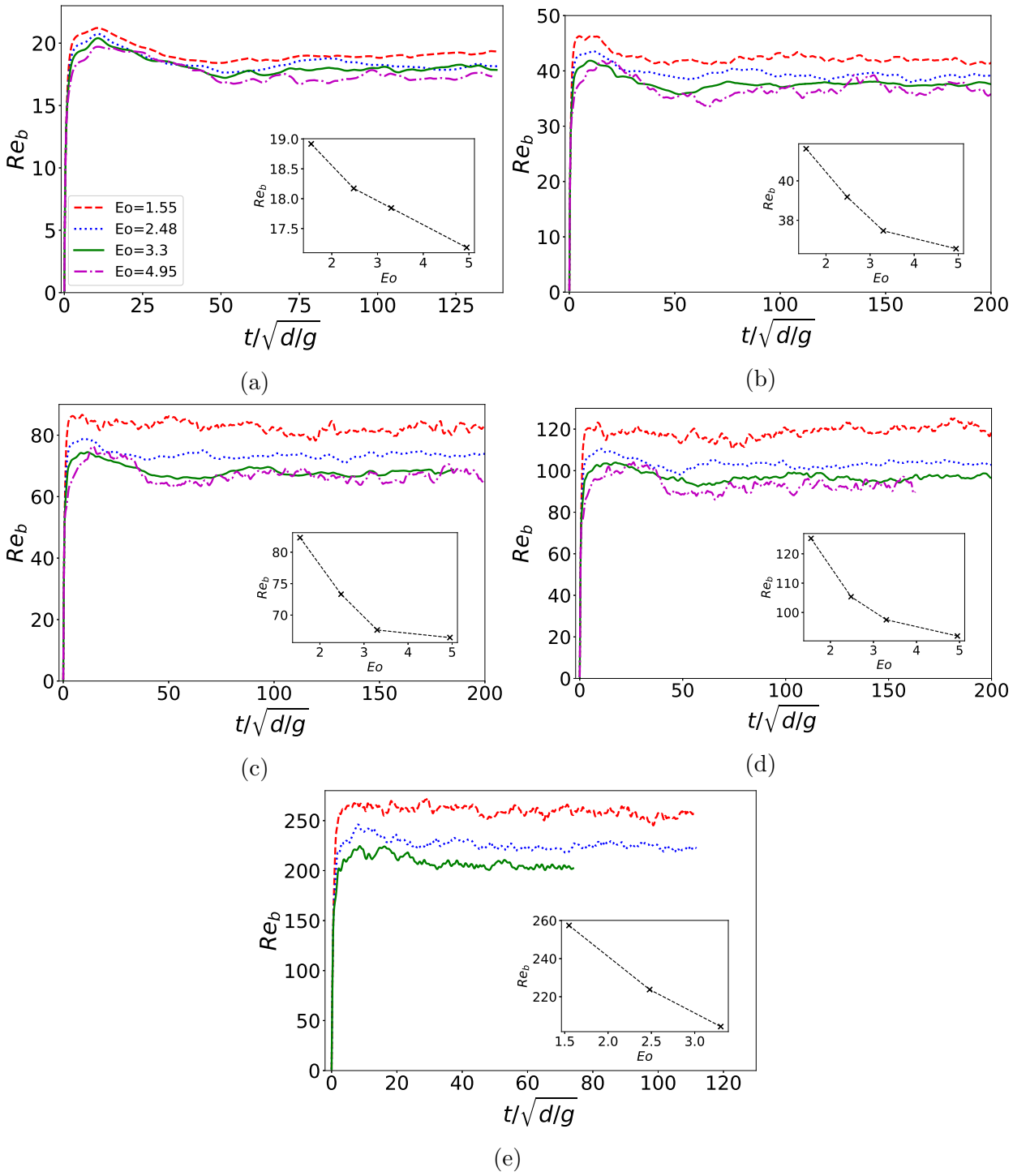

Figure 6.9. Bubble rise Reynolds number for initial Reynolds numbers of (a)Re = 25 (b)Re = 44 (c)Re = 74 (d)Re = 100 (e)Re = 200 for varying Eötvös numbers at $\alpha = 3.66\%$ and $Fr = 14.1$. Inset figures show the bubble Reynolds numbers as a function of Eötvös number for the respective Re

evolution of Re_b as well as the time averaged values as an inline plot. We see from figure 6.8a that the bubble velocity decreases with an increase in the void fraction. This is a trend also observed in several past studies [36], [55], [52]. It is attributed to the hindrance effect, which is the counterflow liquid velocity generated between the bubbles to balance the flow entrained by the bubbles.

Figure 6.8b shows the variation of bubble velocity with Fr. We note that a stronger stratification suppresses the rise velocity as seen on the inline figure in figure 6.8b. One possible explanation for this phenomenon could be that a counter-current is generated in the liquid due to bubble motion. The displaced isopycnals try to revert back to their neutrally buoyant levels creating a force on the bubble competing with the buoyancy force. This competing force is higher for higher stratification since the isopycnals are more resistant to deflections, leading to a decrease in the rise velocity of the bubbles.

Next, we look at the average bubble velocities as a function of Re and Eo (see figure 6.9). We work with a range of Re between 25 and 200 and Eo between 1.55 and 4.95. The first trend we observe is that an increase in deformability of the bubble leads to a decrease in the rise velocity. This can be explained by the higher drag experienced by more deformable bubbles [63], [64]. This trend is uniform regardless of the Reynolds number. This can be seen from the inline figures in figure 6.9, which depict the time averaged bubble Reynolds number as a function of Eo number. For $Re = 25$, we see that this decrease is almost linear upto an Eo of 4.95 (see figure 6.9a). As we increase Re, the decrease is pronounced upto $Eo = 3.3$. Between $Eo = 3.3$ and $Eo = 4.95$, the decrease in rise velocity is much less pronounced (figures 6.9b-d). Bubble shapes greatly influence the rise velocity. At low Reynolds number, for instance at Re=25, the shape change from nearly spherical to deformable bubbles, reduces Re_b by 10% from $Eo = 1.55 to Eo = 4.95$. For the same Eo range, for an Re of 74, Re_b reduces by 20%. This is because at higher Re, the shape change is more drastic in the considered Eo range [65]. If we increase Eo, for $Re = 25$, we expect that Re_b will not show a very linear trend anymore, since Re_b cannot indefinitely decrease with Eo. The shape alterations in the bubble will lead to more complex flow features (including breakup/coalescence) which will affect the bubble Re. For the case of $Re = 200$ and $Eo = 4.95$, we need

higher computational power since we believe that bubble break-up might occur. For a single rising bubble, bubble break-up regime is described in previous studies [66]. It has also been reported that the presence of high liquid shear and liquid turbulence can accelerate the break-up process [67], [68]. Due to the presence of bubble-induced turbulence, for $Re = 200$, the highest Eo we consider is 3.3 to avoid break-up, since we are focusing on a mono-disperse swarm of bubbles.

We also observe that the plot of Re_b shows a transient part where the bubbles are initially accelerating. The transient part reaches a peak value after which the velocity settles to a statistically steady state. The rise of the bubbles in unison causes the existence of the peak in the average bubble rise Reynolds number. Beyond the peak the initial configuration of the bubble breaks up, the bubble wakes are fully developed, bubble interactions are enhanced and the flow is more randomized. This behavior is especially pronounced at low Re (figure 6.9a,6.9b). An interesting thing to note here is that this transient peak occurs at a later time for highly deformable bubbles compared to low-deformability bubbles. The transient phase, where the bubble array retains its original configuration, exists for a longer time for the high Eo cases. This observation was also made by [54] and was attributed to the longer time taken for the development of the larger wake of deformable bubbles. Another observation we make from here is by looking at the velocity fluctuations from the statistical mean with increasing Reynolds number. For example, if we look at the red-dashed curve corresponding to $Eo = 1.55$ in figures 6.9a-e, we see that the bubble velocity fluctuations are higher and more rapid as Re increases. This can be explained by the path instabilities experienced by the bubbles with increasing Reynolds number. We will look at the bubble paths in more detail in the following sections.

6.3.4 Temporal bubble velocity correlations and bubble dispersion

Temporal bubble velocity autocorrelation is defined as

$$C_{xx}(t) = \frac{\langle v'_{bx}(T) v'_{bx}(T+t) \rangle}{\langle v'^2_{bx} \rangle}, \tag{6.8}$$

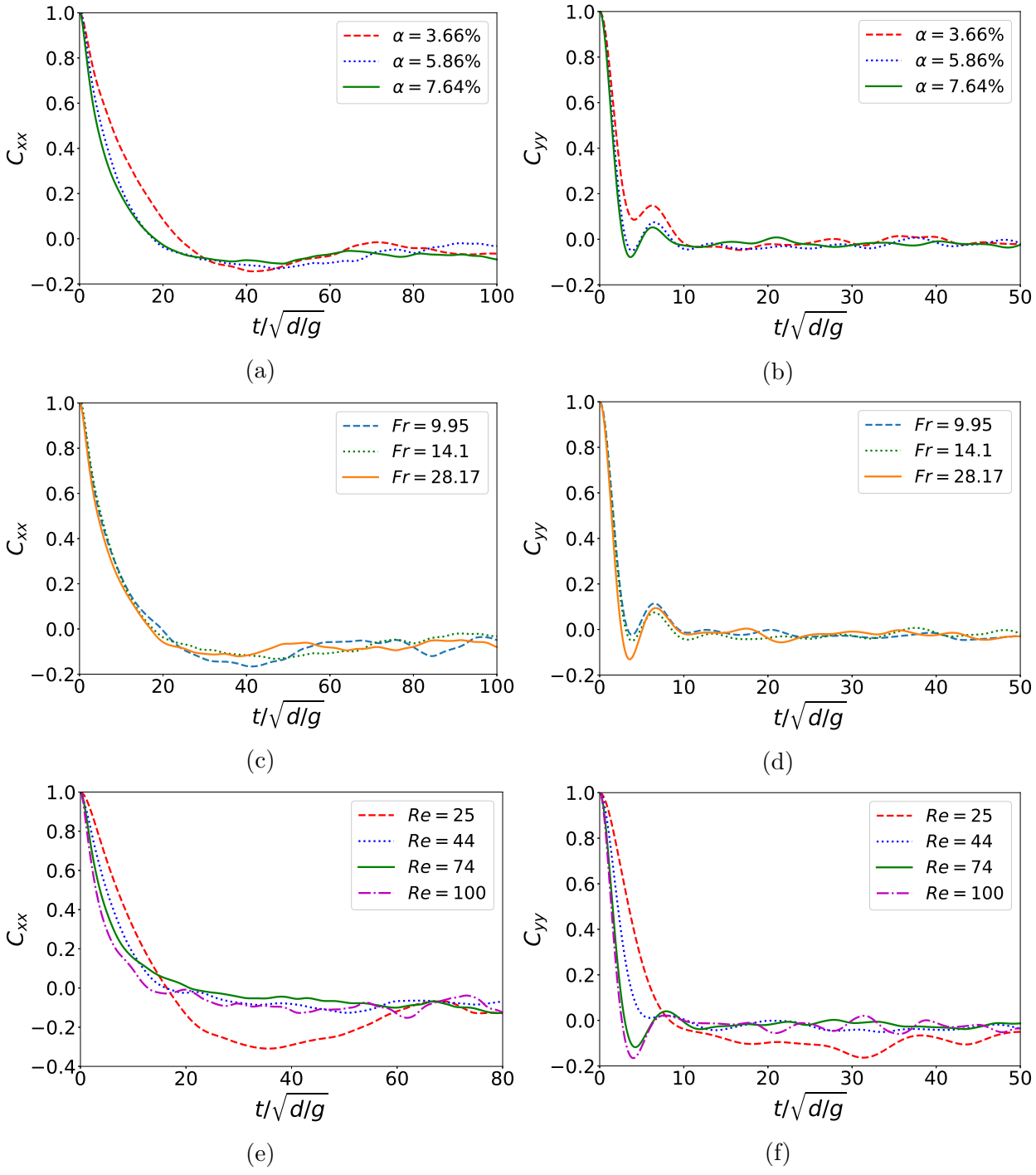

Figure 6.10. Temporal bubble velocity auto-correlation at a constant for varying α at $Fr = 14.1, Re = 44, Eo = 1.55$ (a,b), varying Fr for $\alpha = 5.86\%, Re = 44, Eo = 1.55$ (c,d) varying Re at $\alpha = 3.66\%, Fr = 14.1, Eo = 4.95$ (e,f) in the vertical (a,c,e) and horizontal (b,d,f) directions

$$C_{yy}(t) = \frac{\langle v'_{yy}(T) v'_{by}(T+t) \rangle}{\langle v'^2_{by} \rangle}, \tag{6.9}$$

where v_{bx} and v_{by} refer to the vertical and horizontal bubble velocity respectively, and the primed quantities refer to fluctuations. The temporal velocity autocorrelation is an important tool in studying the bubble paths and interaction between bubbles. It is also helpful in determining the differences in bubble behavior in the horizontal and vertical directions. The autocorrelation functions of horizontal and vertical velocities are shown in figure 6.10. For zero separation in time the velocities are perfectly correlated as expected by definition and the correlation dies down as the time separation increases due to bubble dispersion. We see that there are always some residual oscillations about 0 even after the velocities become uncorrelated. This can be attributed to the small number of samples we have as we approach the end time step, which leads to an increased uncertainty. Besides this, the system size is also seen to have an impact on the temporal velocity correlations [51]. A few general observations are made from the results.

Firstly, we see that the vertical velocity is correlated for longer than the horizontal velocity. This can be explained by the fact the vertical motion is predominant in a buoyancy driven bubble rise flow and the velocities tend to remain correlated for longer unless there are bubble or wake interactions. There is no driving force in the horizontal direction and thus the bubble velocities get uncorrelated faster in this direction. We also notice small oscillations in C_{yy} before dying to 0, whereas C_{xx} shows a steady, exponential decay. The small oscillations in the measurement of C_{yy} can be attributed to horizontal path instabilities and zigzag/spiralling motion of the bubbles as they rise. We note that these initial small scale oscillations are absent when bubbles rise in a mostly rectilinear fashion at $Re = 25$ (figure 6.10f).

Second, we notice that C_{xx} becomes negative and approaches zero from below. This has been attributed to the "correlation effect" which happens due to the back-flow of liquid as the bubbles rise [51], [25]. This type of back-flow was observed in measurements of particle velocity autocorrelation functions in turbulent flows [69]. If

we look closely, we see in figure 6.10c that the maximum negative correlation is higher for more strongly stratified fluids (lower Fr). This is because a highly stratified fluid will experience a more drastic back-flow due to the negative buoyancy experienced by the displaced isopycnal. This in-turn leads to a more negative temporal autocorrelation of velocity. Figure 6.10e shows that the correlation effect is more pronounced in lower $Re = 25$. It has been shown in literature that at low Re, the vertical correlation becomes negative and approaches zero from below [51], while this is not seen for high Reynolds numbers close to 100 [53]. Even with low Re (nearly spherical bubbles), but higher void fraction, [51] observe that the correlation effect is less pronounced compared to low void fraction cases.

We can also characterize the trends in the correlation times when we vary α, Fr and Re. We see that both C_{xx} and C_{yy} get uncorrelated faster for higher void fractions. This can be attributed to the increase in bubble-bubble interactions, leading to more randomness. The correlation time also decreases when we increase Fr, although this trend is mild. This is because the bubble fluctuations increase at higher Froude numbers causing more interactions. The flow is stabilized at high stratifications, a phenomenon also observed in [25] and [26]. At high stratification, the natural buoyancy frequency of the isopycnals is high. This is because the negative buoyant force experienced by the displaced isopycnals is larger in case of higher stratifications. The frequency of oscillation of isopycnals is high. However, due to the strong restorative force, the amplitude of oscillation is low and subsequently the time taken for the isopycnal to revert back to its stable state is low. Higher restorative force inherently increases the stability of the flow. For the same level of perturbations the highest stratification will stabilize and go back to the original configuration faster.

The correlation time also decreases as we increase Re. At low Reynolds numbers the bubbles are nearly spherical and follow rectilinear paths leading to longer correlation times. The bubble interactions are almost absent at low Re.

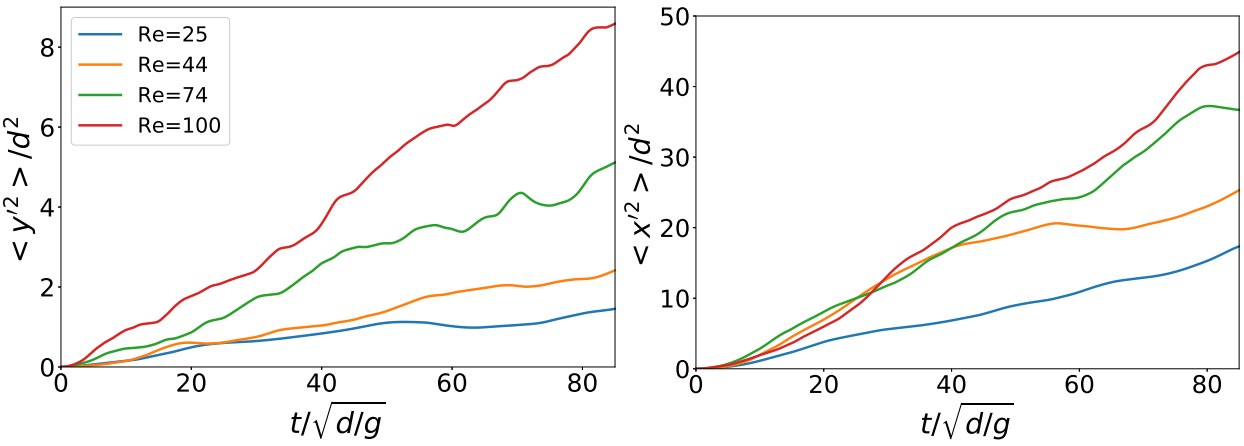

(a) (b)

Figure 6.11. Variance of bubble center displacements in the (a) Horizontal and (b) Vertical directions at $\alpha = 3.66\%, Fr = 14.1, Eo = 4.95$

Variance of bubble center displacements is calculated as

$$\langle x'^2(t)\rangle = \left\langle \left(x^{(\mathrm{i})}(t) - \overline{x(t)}\right)^2 \right\rangle, \tag{6.10}$$

$$\langle y'^2(t)\rangle = \left\langle \left(y^{(\mathrm{i})}(t) - \overline{y(t)}\right)^2 \right\rangle, \tag{6.11}$$

where superscript i refers to the ith bubble, angle brackets imply an average over the bubbles and $\left(\overline{x(t)}, \overline{y(t)}\right) = \left(1/N_b \Sigma_{\mathrm{i}=1}^{N_b} x^{(\mathrm{i})}(t), 1/N_b \Sigma_{\mathrm{i}=1}^{N_b} y^{(\mathrm{i})}(t)\right)$ is the mean position of all bubbles at any given time. The bubble center displacements for $Eo = 4.95$ and varying Re are shown in the horizontal (figure 6.11a) and vertical (figure 6.11b) directions. $t = 0$ here refers to the time when the flow reaches a statistically steady state. A steady increase in $\langle x'^2(t)\rangle$ and $\langle y'^2(t)\rangle$ implies that the bubbles become more scattered with time. We see that in this quasi-steady state, $\langle x'^2(t)\rangle$ and $\langle y'^2(t)\rangle$ have a linear trend with time.

The bubble dispersion process can be approximated as a diffusion process and an estimate for the dispersion coefficients can be found by performing a linear fit to

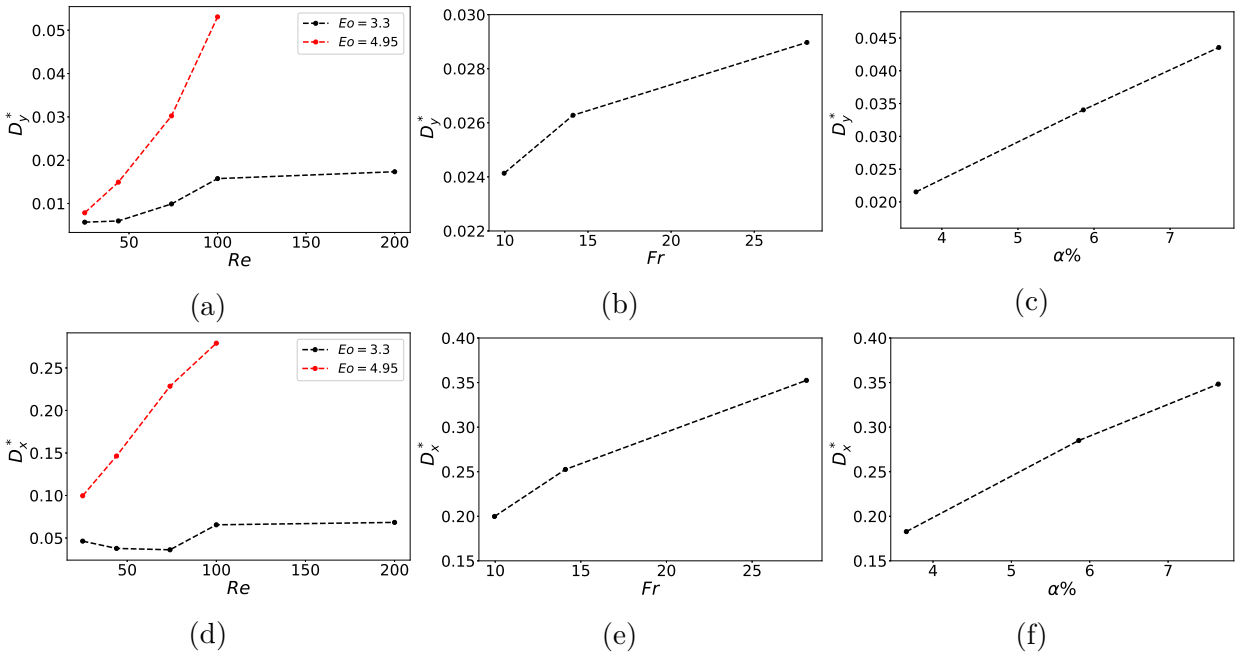

Figure 6.12. Horizontal (a,b,c) and Vertical (d,e,f) Diffusion coefficients for $\alpha = 3.66\%$, $Fr = 14.1$ as a function of Re (a,d), $\alpha = 5.86\%$, $Re = 44$, $Eo = 1.55$ as a function of Fr (b,e) and $Fr = 14.1$, $Re = 44$, $Eo = 1.55$ as a function of α, non-dimensionalized by $gd^{3/2}$

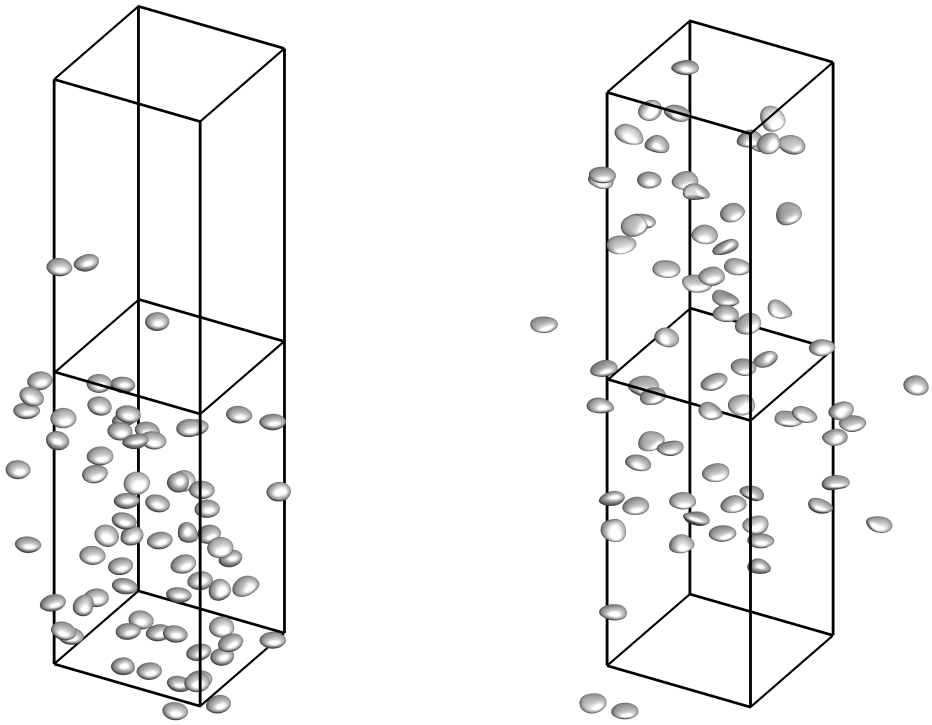

(a) (b)

Figure 6.13. Bubble dispersion for $\alpha = 3.66\%, Fr = 14.1, Re = 100$ and $Eo =$ (a) 1.55 (b) 4.95 at $t^* = 112$

the bubble center displacements and finding their slopes. The non-dimensionalized dispersion coefficient is thus given by

$$D_x^* = \frac{1}{2}\frac{d\langle x'^2(t)\rangle^*}{dt^*}, \tag{6.12}$$

$$D_y^* = \frac{1}{2}\frac{d\langle y'^2(t)\rangle^*}{dt^*}, \tag{6.13}$$

where a superscript * refers to a non-dimensional quantity. D_x and D_y are both non-dimensionalized by $gd^{3/2}$. D_x^* and D_y^* give a measure of how dispersed the bubbles are with respect to each other or the rate at which the mean-square displacements of the bubbles increases in a quasi-steady state. We see from figure 6.12 that the dispersion in the vertical direction is much higher than the horizontal direction (roughly 5 times). Figure 6.12a and 6.12d shows that the dispersion increases as Re increases

for $Eo = 4.95$. The variation in vertical dispersion with Re is much lesser for $Eo = 3.3$, which can have an effect on mixing levels. We can explain this based on the bubble shapes and formation of horizontal rafts. It has been established in previous studies that bubbles closer to sphericity (lower Eo) have more tendency to form horizontal clusters which reduces vertical and horizontal dispersion [53]. The bubble shape and path instability variation as Re is changed for lower Eo is less dramatic than the variation for the higher Eo (=4.95). This results in a more drastic variation in bubble dispersion for Eo 4.95. We also plot the bubble locations for $Re = 100$ for two Eo in figure 6.13. We see that for $Eo = 1.55$, the bubbles are confined to a single periodic box, while for $Eo = 4.95$, the vertical extent of the bubbles is close to two periodic boxes.

An increase in bubble dispersion is seen when we decrease stratification (figure 6.12b,d). This happens because an increase in stratification leads to a suppression of bubble fluctuations in both directions. A similar observation was made for drops in [25], where the vertical and horizontal extend of a swarm of drops were hampered by density stratification. Increasing the void fraction leads to an almost linear increase in the dispersion coefficient in both directions. It was seen in [51], that the dispersion coefficient in the vertical direction increases with α and reaches a maximum value. Beyond this, it starts to decrease. In our simulations, we have not reached the maximum dispersion to start seeing the decreasing trend.

6.3.5 Pair Distribution functions

At lower Reynolds numbers, from $Re = 25$ to $Re = 44$, we see a dip in the mixing parameters for all except the highest Eo. We explain this behavior by considering the microstructure of the bubble swarm. The relative bubble locations and clustering can be understood by looking at the radial and angular pair probability distributions. The radial distribution is an indicator of the probability that the centroids of any two bubbles are at a distance r apart. It is computed by counting and normalizing the

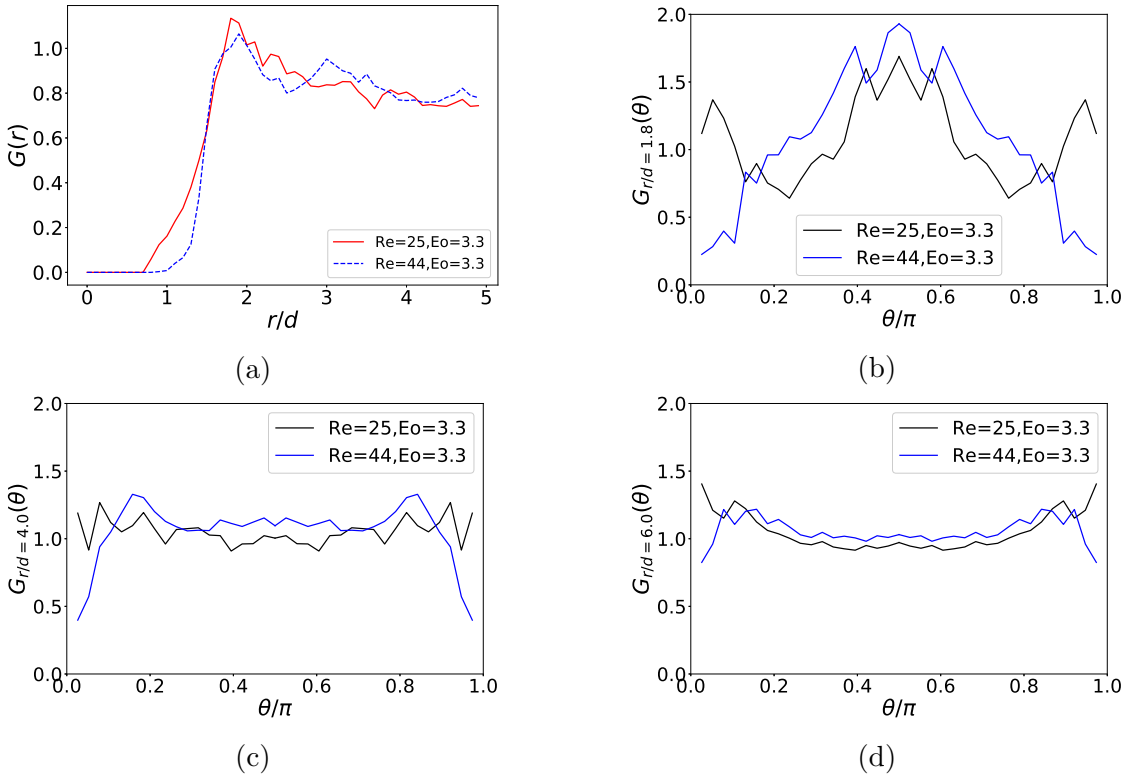

Figure 6.14. (a) Radial and (b,c) Angular pair probability distribution at (b) $r = 1.8d$, (c) $r = 4.0d$ (d) $r = 6.0d$ for $\alpha = 3.66\%, Fr = 14.1$

number of bubbles present at a distance r from the reference bubble in a spherical shell of thickness Δr. It is defined as

$$G(r) = \frac{V_T}{\Delta V(r)} \frac{1}{N_b(N_b-1)} \sum_{\substack{i=1}}^{N_b} \sum_{\substack{j=1 \\ j\neq i}}^{N_b} \delta(r - \Delta r/2 \leq R_{ij} < r + \Delta r/2), \tag{6.14}$$

where V_T is the total volume of the domain, $\Delta V(r)$ is the volume of the spherical shell and R_{ij} is the distance between the two considered bubbles.

The angular pair distribution indicates the probability that the angle between the line joining the bubble centroids and the vertical axis is θ at a particular r. It is

computed by counting the number of bubbles present at an angle θ from the reference bubble in a spherical sector of angle $\Delta\theta$. It is defined as

$$G_r(\theta) = \frac{V_T}{\Delta V(\theta)} \frac{1}{N_b(N_b-1)} \sum_{\mathrm{i}=1}^{N_b} \sum_{\substack{\mathrm{j}=1 \\ \mathrm{j}\neq\mathrm{i}}}^{N_b} \delta(\theta - \Delta\theta/2 \leq \Theta_{\mathrm{ij}} < \theta + \Delta\theta/2; R_{\mathrm{ij}} < r), \tag{6.15}$$

where $\Delta V(\theta) = 2/3\pi r^3 \left(cos(\theta - \Delta\theta/2) - cos(\theta + \Delta\theta/2)\right)$ is the volume of the sector, Θ_{ij} is the angle between the line joining the centroids of the two considered bubbles. We normalize $G_r(\theta)$ such that $\int_0^1 G_r(\theta^*)d\theta^* = 1$, where $\theta^* = \theta/\pi$.

Both the radial and angular pair probability distributions are averaged over time during steady using 250 time steps. Doubling and halving the time-steps showed almost no change in the pair probability distribution plots. We use 50 bins for the radial and 40 bins for the angular pair probabilities. We checked that changing the bin size does not have a significant impact either.

$G(r)$ calculated for the two Reynolds numbers at $Eo = 3.3$ is shown in figure 6.14a. We note a few differences here. Firstly, $G(r)$ increases to a non-zero value at lower r value (for $r/d < 1$) for $Re = 25$. The peak is also higher for $Re = 25$, indicating more bubbles at a short range compared to $Re = 44$. The differences are more apparent in the angular pair distributions. At a short range, $r = 1.8d$, (see figure 6.14b) we see that the probability of finding horizontal bubbles streams is almost the same as the probability of finding vertical ones for $Re = 25$, since we see peaks at $\theta = 0, \pi/2, \pi$. Coexistence of vertical and horizontal clusters could mean that a subset of the bubbles is moving faster due to vertical streaming while another subset is moving slower owing to horizontal rafts. This potentially leads to high bubble velocity fluctuations, which in turn influences mixing characteristics. On the other hand, for $Re = 44$, we see a peak only at $\theta = \pi/2$. Presence of only horizontal rafts gives rise to lower bubble fluctuations. At long range, $r = 4d$, (see figure 6.14c), $G_r(\theta)$ approaches a uniform value of 1.0 for both the cases as expected [39], [25], [54]. The uniformity is better for $r = 6.0d$ (figure 6.14d). Apart from time over which the solution is averaged and bin

size, the number of bubbles also plays a role in the smoothness of the plot. Averaging spatially over more number of bubbles would give smoother results.

6.3.6 Velocity fluctuations: Liquid and bubbles

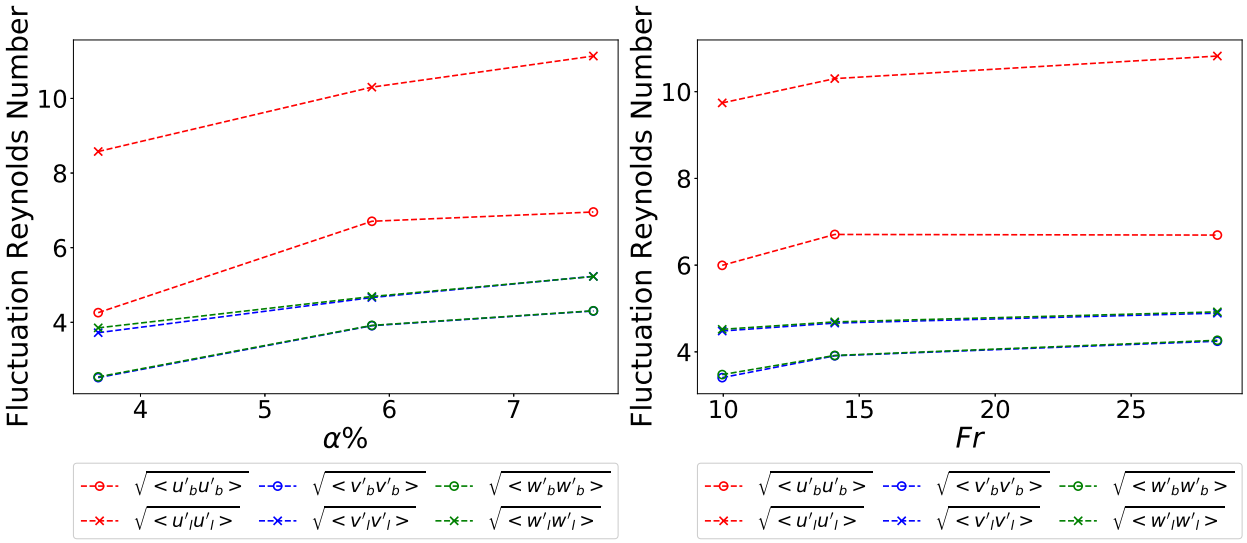

(a) (b)

Figure 6.15. Non-dimensional liquid and bubble velocity fluctuations for (a) varying α at $Fr = 14.1, Re = 44, Eo = 1.55$ and (b) varying Fr for $\alpha = 5.86\%, Re = 44, Eo = 1.55$

The velocity fluctuations in the domain are characterized by the fluctuation Reynolds number in this study. Fluctuation Reynolds number is defined as $Re_{u'u'} = \rho_l \sqrt{< u'u' >} d/\mu_l$, where the averaging operator, $<>$, denotes spatial as well as temporal averaging in the statistically steady state of flow. In figure 6.15, we calculate this quantity for both the liquid as well as bubbles to show a comparison. The motion of the bubbles causes pseudo-turbulence in the liquid phase. One observation we note here is that the fluctuations in y and z, that is the horizontal directions, are almost coincident for both liquid and the bubbles. This suggests that the flow is isotropic in the two horizontal directions for both the liquid as well as bubble motion. The fluctuations in the vertical direction are larger than in the horizontal plane as expected due to the inherent anisotropy of the

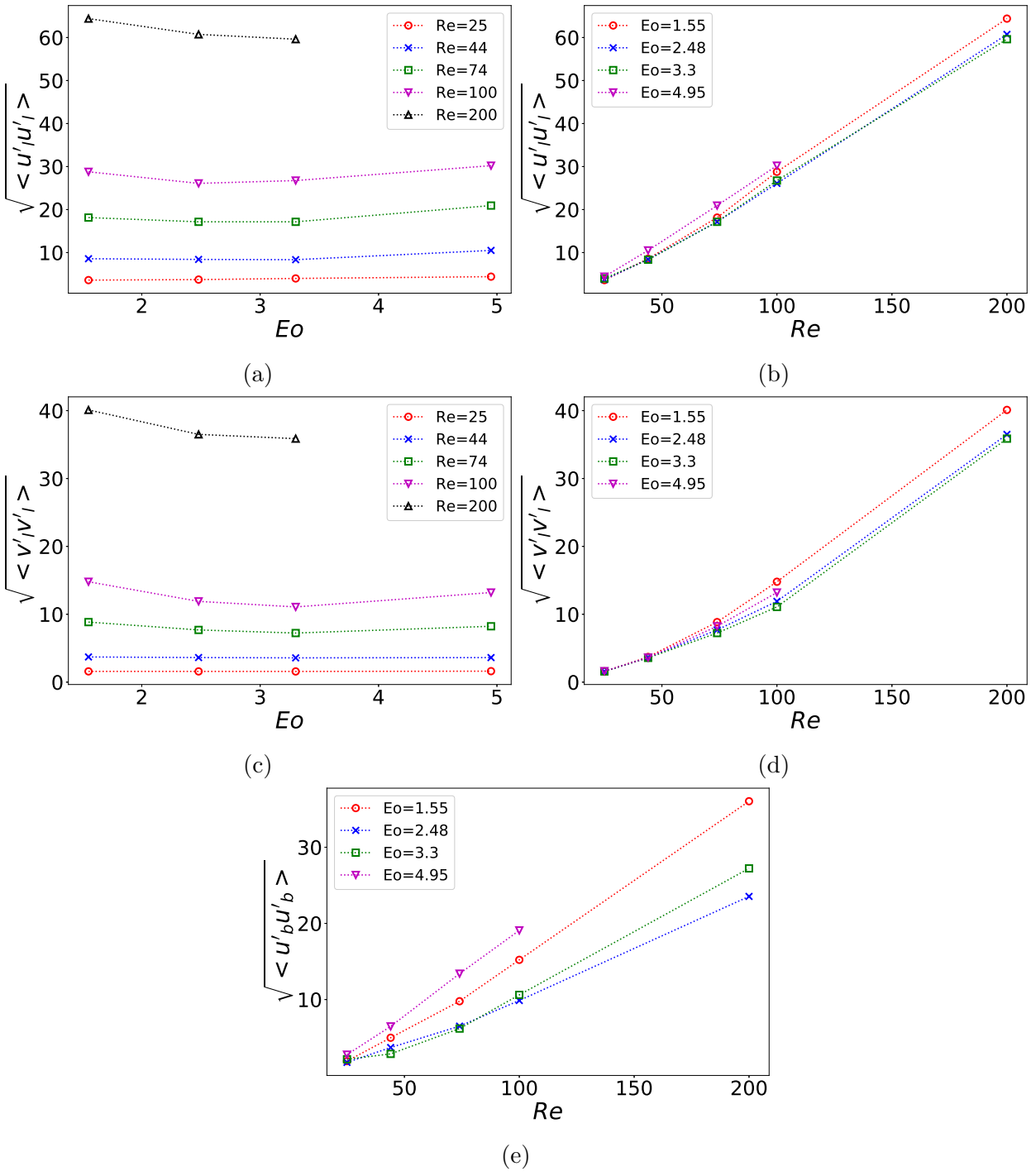

Figure 6.16. Non-dimensional liquid velocity fluctuations in vertical (a,b) and horizontal (c,d) directions. (e): Non-dimensional bubble velocity fluctuations in vertical direction for $\alpha = 3.66\%, Fr = 14.1$

bubble motion in the vertical direction. We expect the cross-correlation components of liquid velocity fluctuations to be zero due to symmetry.

An increase in α leads to an expected increase in bubble velocity fluctuations due to the increased probability of interactions (figure 6.15a). We also see that these fluctuations are likewise transferred to the liquid, where we see a similar rising trend in liquid fluctuations with α. As explained earlier, an increase in stratification strength suppresses bubble velocity fluctuations and this can be seen in figure 6.15b. The liquid velocity fluctuations are also suppressed due to the high buoyancy frequency and resistance to disturbances by the isopycnals.

The non-dimensionalized liquid velocity fluctuations for a variation in Re and Eo are shown in figure 6.16. Figures 6.16a,c show the variation of fluctuations as a function of Eo in the vertical and horizontal directions respectively. For the lower $Re = 25, 44$ and 74, the liquid fluctuations are almost constant between $Eo = 1.55 - 3.3$ and show a rise at $Eo = 4.95$. At higher $Re = 100$ and 200, we in fact see a decreasing trend in the fluctuations till $Eo = 3.3$ and a similar jump at $Eo = 4.95$. This could be attributed to the fact that at the Reynolds numbers considered, the bubble deformation is very high for $Eo = 4.95$, which causes drastic liquid fluctuations. Another observation we make from these plots is that a change in Re has a higher impact on the vertical fluctuations than the horizontal fluctuations. This trend is clearly visible in figures 6.16b,d. Plotting the fluctuations against Re shows a remarkable collapse of all the data points and an almost linear increase in the fluctuations with Re can be seen. The slope of the curve is higher for the vertical than the horizontal fluctuations. Bubble velocity fluctuations monotonically increase with Reynolds number, showing a trend similar to the liquid fluctuations (6.16e). An increase in the Re causes the formation of larger turbulent structures thereby increasing the velocity fluctuations.

The bubble and liquid velocity fluctuations for a high $Fr = 44.5, Re = 80$ and $Eo = 4$ are compared with previous work on homogeneous bubbly flows. We first look at the normalized bubble velocity fluctuations, $T_b = \langle u_b' u_b' \rangle / u_{b,avg}^2$. The average bubble fluctuations match quite well with the experimental results from [52] carried out at Re between $400 - 535$ and Eo between $0.229 - 0.78$ (see table 6.2). Next, we also

Table 6.2. Comparison of velocity fluctuations with previous experimental and numerical work

	Present simulation at $Fr = 44.5$	**Experimental results** [52]
T_b	0.047	0.045
	Present simulation at $Fr = 44.5$	**Numerical results** [53]
$\widetilde{\tau_{11}}$	2.774	2.868
$\widetilde{\tau_{22}}$	0.522	0.6016
$\widetilde{\tau_{33}}$	0.533	0.6023

compare three components of liquid Reynolds stresses, $\widetilde{\tau_{11}} = \dfrac{\langle u_l' u_l' \rangle}{u_{b,avg}^2 \alpha}$, $\widetilde{\tau_{22}} = \dfrac{\langle v_l' v_l' \rangle}{u_{b,avg}^2 \alpha}$ and $\widetilde{\tau_{33}} = \dfrac{\langle w_l' w_l' \rangle}{u_{b,avg}^2 \alpha}$ with results from [53] simulated at $Re \approx 90, Eo = 4, \alpha = 5.83\%$. Again, a good match is seen for all three components. The slightly higher values obtained by [53] can be attributed to the slightly higher Re that they used. It could also be due to the small stratification we have as opposed to a fully homogeneous fluid used in the simulations by [53]. We also observe that τ_{22} and τ_{33} are approximately equal, since the flow is isotropic in the horizontal directions.

The bubble induced turbulence can also be characterized by looking at the isotropic turbulent kinetic energy spectrum at steady state where the production of energy by bubbles is balanced by dissipation by the liquid. The energy spectrum is calculated by first taking a discrete three dimensional Fourier transform of the liquid velocity fluctuations over space. The spectrum is then calculated as $U\widehat{U} + V\widehat{V} + W\widehat{W}$, where U, V, W are the Fourier transforms of the liquid velocity fluctuations and $\widehat{.}$ stands for the complex conjugate. Energy is then summed in spherical shells of width δk and normalized as $\Sigma_k E(k)\delta k = \frac{1}{2}\int_{V_l} \rho ||\mathbf{u}||^2 dV$, where V_l is the volume of liquid alone. This is done for multiple time-steps and we found that the spectrum does not change in the statistically steady regime. The kinetic energy spectrum at one particular time instant is shown in figure 6.17. We calculate the slope of the energy cascade by fitting a line to the linear portion of the log-log graph. The energy cascade shows a slope close to -3. We see a slightly higher slope of -3.25 for low Reynolds number cases while $Re = 100$, shows a slope of -3 (figure 6.17c). Various experimental [36], [70] and numerical [71]

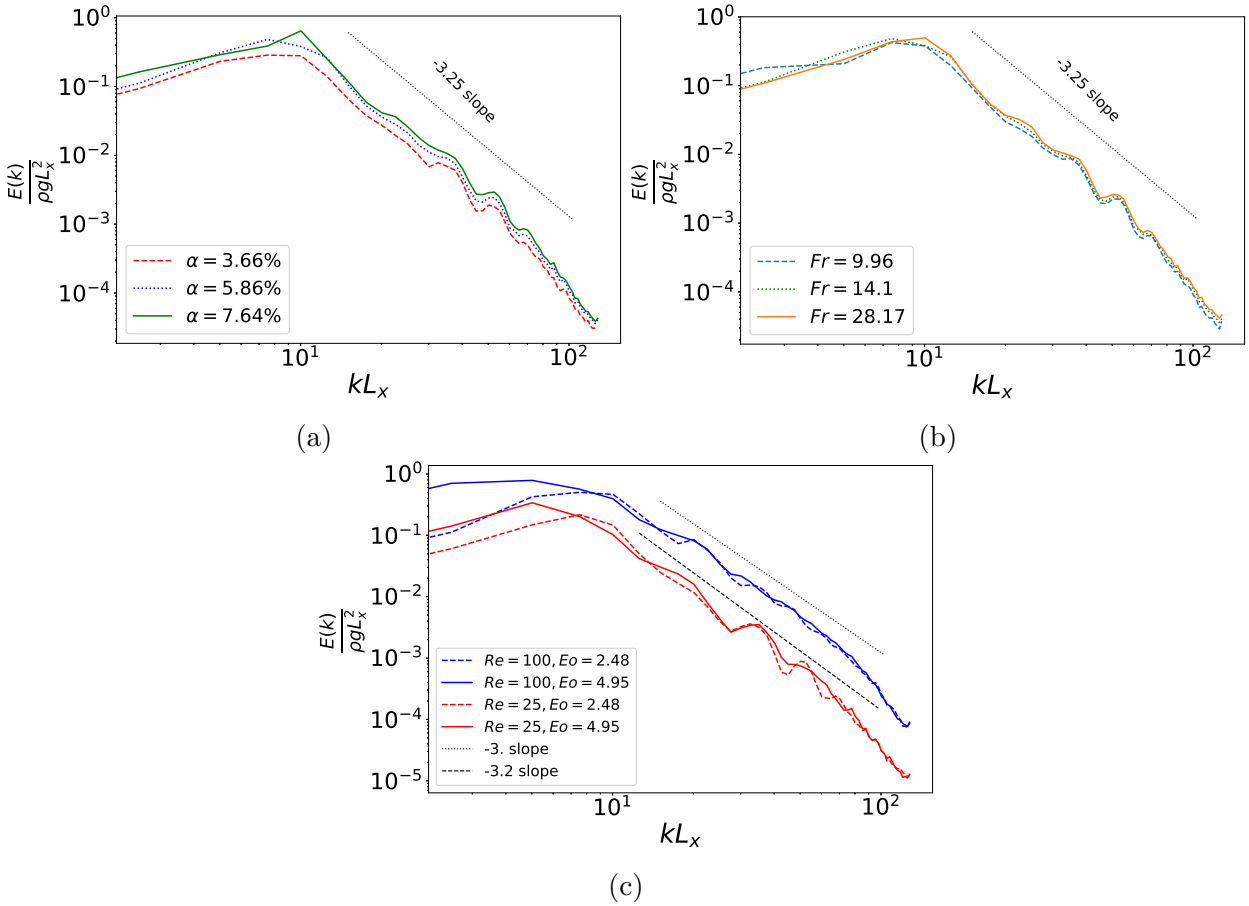

Figure 6.17. Turbulent kinetic energy spectrum for (a) varying α at $Fr = 14.1, Re = 44, Eo = 1.55$ (b) varying Fr for $\alpha = 5.86\%, Re = 44, Eo = 1.55$ and (c) varying Eo and Re at $\alpha = 3.66\%, Fr = 14.1$

investigations of high Reynolds number bubbly flows report a kinetic energy spectrum slope of -3. [72] report a slope of -3.2 at $Re = 1000$ and $3 < Eo < 4$. On the other hand, [51] study low Reynolds number bubbles (≈ 36) with low deformability ($Eo \approx 1$) and report the energy spectrum slope of -3.6, suggesting that the spectrum slope can vary slightly depending on Reynolds numbers and bubble deformabilities. In figure 6.17a, we see that the curves of lower α are shifted downward compared to the higher α due to a decrease in kinetic energy of the liquid. We also visualize the effect of stratification on the energy spectrum in figure 6.17b. We find that the weakly stratified liquid has more energy overall, since the bubble motion through the isopycnals causes more velocity fluctuations. The energy spectrum for $Re = 25$ and $Re = 100$ for two different Eo

are plotted in figure 6.17c. We note that for a constant Re, an increase in Eo, i.e, higher deformability, leads to higher energy levels at low wavenumbers. At higher wavenumbers, the curves of constant Re collapse due to the fluctuation lengthscale being very small compared to bubble size as noted before. When comparing the two different Re, we see that the curve is shifted significantly up for the higher Re due to higher energy levels.

6.4 Modeling using Gaussian Process regression

We also try to come up with a preliminary model for the data by means of using Gaussian Processes (GP). The obtained model could also be useful in constructing surrogate models for the data which can be used for uncertainty analyses using MC simulations. Presently, we have data for a range of bubble Reynolds numbers, $Re = \rho_N \sqrt{gd} d/\mu_l$ and Eötvös number, $Eo = (\rho_l - \rho_b) g d^2/S$ which controls the bubble deformability. We try to generate a response surface in these 2 dimensions using Gaussian Processes.

We assume a GP prior on the function approximating the data ,i.e, $f(\cdot) \sim \text{GP}\left(m(\cdot), k(\cdot,\cdot)\right)$ with mean vector: $\mathbf{m}(\mathbf{x}_{1:n}) = \left(m(\mathbf{x}_1), \ldots, m(\mathbf{x}_n)\right)$, and covariance matrix:

$$\mathbf{K}(\mathbf{x}_{1:n}, \mathbf{x}_{1:n}) = \begin{pmatrix} k(\mathbf{x}_1, \mathbf{x}_1) & \ldots & k(\mathbf{x}_1, \mathbf{x}_n) \\ \vdots & \ddots & \vdots \\ k(\mathbf{x}_n, \mathbf{x}_1) & \ldots & k(\mathbf{x}_n, \mathbf{x}_n) \end{pmatrix}.$$

We also assume a Normal likelihood for the data with mean $f(\mathbf{x}_\text{i})$ and variance σ^2. By applying Baye's rule we get the posterior $\mathbf{f}^*$, which is also a GP, at inputs $\mathbf{x}^*$ as

$$p(\mathbf{f}^*_{1:n^*} | \mathbf{x}^*_{1:n^*}, \mathcal{D}) = \mathcal{N}\left(\mathbf{f}^*_{1:n^*} | \mathbf{m}_n(\mathbf{x}^*_{1:n^*}), \mathbf{K}_n(\mathbf{x}^*_{1:n^*}, \mathbf{x}^*_{1:n^*})\right), \tag{6.16}$$

where posterior mean function and the posterior covariance function respectively are ,

$$m_n(x) = m(x) + \mathbf{k}(x, \mathbf{x}_{1:n}) \left(\mathbf{K}(\mathbf{x}_{1:n}, \mathbf{x}_{1:n}) + \sigma^2 I_n\right)^{-1} \left(\mathbf{y}_{1:n} - \mathbf{m}(\mathbf{x}_{1:n})\right), \tag{6.17a}$$

$$k_n(x, x') = k(x, x') - \mathbf{k}(x, \mathbf{x}_{1:n}) \left(\mathbf{K}(\mathbf{x}_{1:n}, \mathbf{x}_{1:n}) + \sigma^2 I_n\right)^{-1} \mathbf{k}^T(x, \mathbf{x}_{1:n}). \tag{6.17b}$$

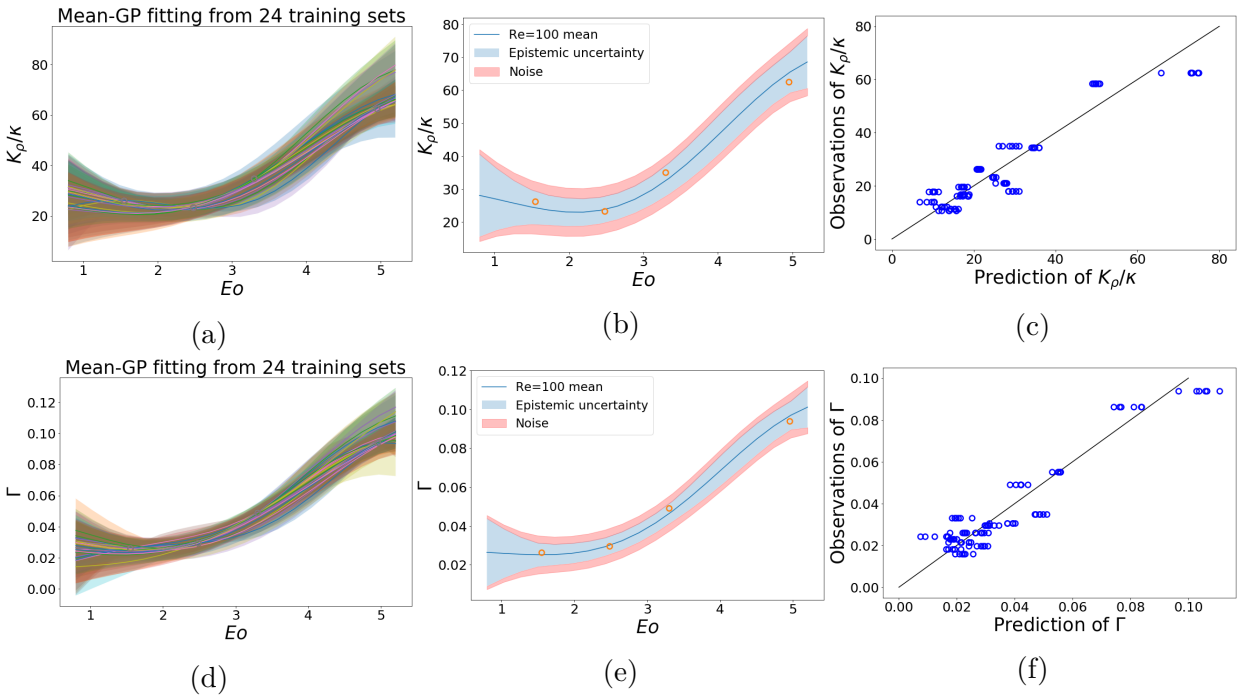

Figure 6.18. (a,d) Mean and uncertainty from 24 GP runs (b,e) Ensemble mean and uncertainty for Re=100, (c,f) Observation vs prediction. (a,b,c) corresponds to eddy diffusivity, (d,e,f) corresponds to mixing efficiency

We extend the same concept to 2 dimensions, our dimensions consisting of Re and Eo. We use the GPy package to carry out Gaussian Process regression. In our simulations, we use a squared exponential kernel function in two dimensions and use ARD to pick the lengthscales for each dimension.

Another step in the Gaussian proccess training is to make sure the training procedure is not merely memorizing the data and is able to predict correct values at unknown inputs. In order to do this, we divide our data into training and testing sets. Since we have a limited data set, the splitting of data is done randomly and multiple times. In the present analysis we use 24 non-repetitive training and testing sets by shuffling the data. The final mean and covariance prediction is an average of all the 24 training procedures. In order to perform diagnostics, we plot the predictions vs observations as well as find the coefficient of determination R squared, defined as, $R^2 = 1 - \frac{\sum_{\mathrm{i}=1}^{n^v}\left[y_{\mathrm{i}}^v - m_n(\mathbf{x}_{\mathrm{i}}^v)\right]^2}{\sum_{\mathrm{i}=1}^{n^v}\left[y_{\mathrm{i}}^v - \bar{y}^v\right]^2}$, where $\bar{y}^v$ is the mean of the observed data $\bar{y}^v = \frac{1}{n^v}\sum_{\mathrm{i}=1}^{n^v} y_{\mathrm{i}}^v$.

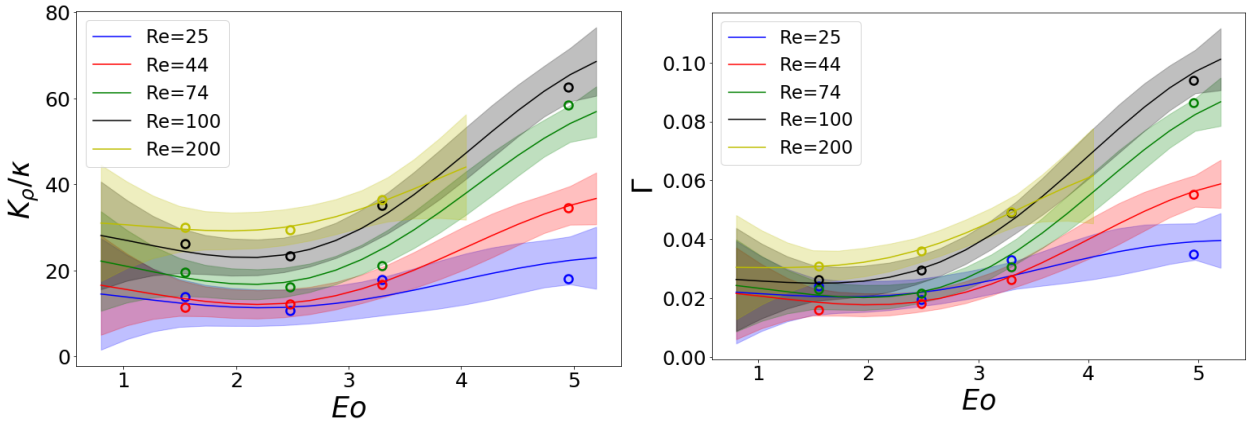

(a) (b)

Figure 6.19. Posterior predictive distribution of (a) eddy diffusivity (b) mixing efficiency

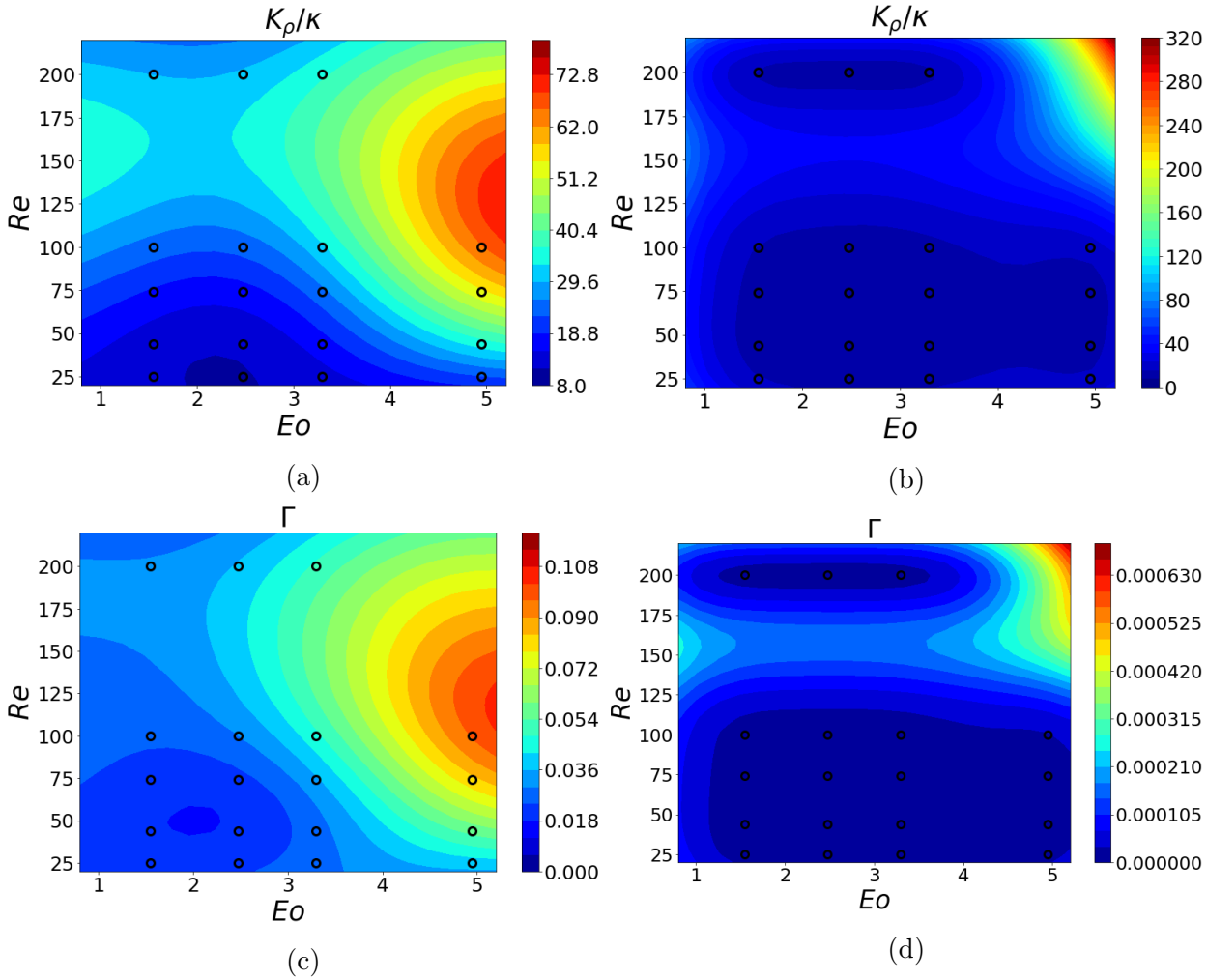

(a) (b) (c) (d)

Figure 6.20. Two dimensional response surfaces for (a,b) eddy diffusivity (c,d) mixing efficiency where (a,c) give the mean and (b,d) give the variance

Using the GP method discussed above, we perform regression on K_ρ and Γ in the $Re - Eo$ plane. We shuffle the available data into 24 training + testing sets and we obtain the mean and variance from these 24 regressions (see figure 6.18a, d). We take an average of all these outputs to get the mean, epistemic uncertainty and noise. One of the cases (Re = 100) is shown in figures 6.18b, e. From these 24 regression sets, with each set composed of 4 training points, we plot the observation vs prediction plot of K_ρ and Γ in figures 6.18c and f respectively. We see that at low values of K_ρ and Γ the points lie very close to the $y = x$ line. The higher values do show some discrepancies. This could be because at higher Reynolds numbers, where we expect higher mixing levels, we only have sparse data due to high computational cost. We believe that the analysis can be improved by adding more points to our data. Nevertheless, we also compute the R^2 value which gives a measure of how well the observed outcomes are replicated by the model, based on the proportion of total variation of outcomes explained by the model. As defined before $R^2 = 1 - \frac{\sum_{i=1}^{n^v}\left[y_i^v - m_n(\mathbf{x}_i^v)\right]^2}{\sum_{i=1}^{n^v}\left[y_i^v - \bar{y}^v\right]^2}$, where the numerator of the second term on the right hand side, gives the variance of the mean prediction from the observed quantity. For a perfect model, this term would go to 0 leading to $R^2 = 1$. For the present analysis, we obtained an R^2 value of 0.88 for Γ and 0.854 for K_ρ which come close to 1.

We then get the posterior predictive distribution for the two quantities as a function of Eo at different Re (figure 6.19). We see that at low Eo the mixing strength is stagnant and increases rapidly for higher Eo. This trend is captured by the posterior GP well. We also get the 2D response surface plotted as a contour plot (see figure 6.20). The mean values are given in figure 6.20a and c, while the variances are plotted in figure 6.20b and d. The dots on the figures correspond to the observed quantities. We see that the uncertainty at the right top corner, corresponding to high Eo and high Re, is high for both the mixing quantities. This is because we have very sparse data near these points. The mean trend at these points may also be misrepresented. However, the trend at low Re and Eo have been captured quite well by the GP.

6.5 Summary

In this study, we numerically investigated the rise of bubbles in a stratified flow in an unconfined domain. We run simulations for a range of void fractions, Froude numbers, Reynolds numbers and bubble deformabilities. The bubble dynamics is studied by looking at the rise velocities and temporal velocity autocorrelations of the bubbles. We find that the vertical velocity is correlated for longer than the horizontal in general and also record trends for the correlation times as we change various physical parameters of the system. Bubble dispersion in the vertical and horizontal directions is quantified by the dispersion coefficient. The dispersion increases as we increase Reynolds number, void fraction or the Froude number. We quantify the mixing induced in the background liquid by the motion of bubbles through the diapycnal eddy diffusivity, Cox number and mixing efficiency. We find that the vertical buoyancy flux increases when we decrease the stratification due to lesser resistance to disturbance by the isopycnals. This allows for more time for thermal mixing. We see that increasing the number of bubbles in the domain has a similar effect. We also quantify mixing in terms of energetics of the background liquid. An increase in Eo has almost no effect on liquid velocity fluctuations, but we see that the vertical eddy diffusivity increases. This leads to the inference that the energy input to the system is constant, but more of it goes into vertical mixing of the liquid than viscous dissipation as we increase Eo. Similarly, when we increase Re, we see a near linear increase in liquid fluctuations. However, this is not the case with the mixing efficiency trend, suggesting that most of the extra energy input upon increasing Re is dissipated. We also gain interesting insights by looking at the energy spectrum and see that the energy cascade follows a slope of ~ -3.0. Finally, preliminary modeling of the data using Gaussian Process regression has been performed. We report an R^2 value of 0.880 and 0.854 for the mixing efficiency and the diapycnal eddy diffusivity, respectively. We get a very good prediction vs observation plot for lower mixing values where we have a good amount of data.

7. TRANSIENT SINGLE BUBBLE DYNAMICS IN STABLY STRATIFIED FLUIDS

7.1 Literature Review

Rising motion of a bubble and the bubble dynamics are significantly affected by density gradients in the background liquid produced by temperature and salinity gradients in oceans and lakes. Numerous studies have been made in understanding the physics behind settling spheres [6], [73], [74], [75] and rising drops [27], [5], [25] in a density gradient.

Settling of sphere through sharp density gradients results in enhanced drag on the sphere [74]. As the sphere moves from lower to higher density, it entrains liquid, which experiences buoyant forces when it enters the high density region. Stratification effects can lead to oscillating velocity of particles with the formation of secondary and tertiary vortices behind the primary vortex [76]. In extreme cases, particles experience such high levels of drag that levitation and bounce back of sphere has been reported in sharp gradients [77].

Stratification effects in the rise and settling of drops has gained significant importance in recent times. Blanchette and Shapiro [78] analyzed the descent of nearly spherical drops in density gradients. For a Reynolds number of 10, they found that if the two background fluids had the same surface tension, the fluid entrained by the drop becomes buoyant and slows down the drop temporarily. When the surface tensions are different, the tangential flows or the Marangoni effect becomes important in determining the drop's motion. Bayareh et. al. [5] observed that a single drop rising in a stratified medium experiences drag enhancement compared to a homogeneous fluid. They also report the formation of secondary vortex and resulting buoyant jet in wake of the drop.

Díaz-Damacillo et. al. [29] experimentally investigated the rising motion of a single bubble across two different-density liquids. For smaller bubbles moving in a rectilinear fashion, they find that the drift volume returns to the bottom fluid with almost no mixing. The drift volume in this case was found to be stable and inversely

proportional to the bubble Reynolds number. On the other hand, for larger bubbles moving in a zigzag manner, the drift volume became unstable. Patches of dense fluid are left behind in the lighter fluid, leading to mixing. To the best of our knowledge, the effects of stratification, Reynolds number and interface deformability on the rising motion of a bubble in stratified fluids is a problem that has not been widely tackled in literature.

In this study, we will study the transient rising motion of a bubble in density stratified fluids. The organization of different sections is as follows. The problem set up and initial and boundary conditions are first discussed. Next, the validation of the code written in Basilisk using AMR is presented for both non-stratified flow and the implementation of the energy equation solver. We then move on to the results. The effect of stratification on bubble dynamics is first analyzed. The modified bubble wake, drift volume associated with the bubble and drag estimation for different stratification strengths is discussed. Following this, the role of bubble Reynolds number and deformability effects on the above-mentioned physical parameters are analyzed. Finally, the behavior of the bubble when it rises in a fluid with only partial stratification is touched upon briefly, since this comes closer to the real world density gradients present in lakes and reservoirs.

7.2 Problem Description

The objective here is to simulate the rise of a single bubble in infinite stratified fluids and study the resulting bubble dynamics in the axisymmetric limit. A schematic for the problem is shown in figure 7.1. We have rigid walls on the left, top and right and we have a symmetry boundary at the bottom. The gravity acts in the x direction. We will restrict ourselves to rise of bubbles in the axisymmetric $Re - Eo$ range. The bubble motion and wake is reported to be axisymmetric in the range $0.1 < Bo < 100$ and $5 < Re < 200$ [79], [65]. Axisymmetric shape oscillations were observed for $Re = 200$ when $5 < Bo < 20$ [79]. Experimental work have also shown wobbling bubbles [80], [81] for $Re \geq 200$. Bhaga and Weber [82] report cases where bubble shapes oscillate

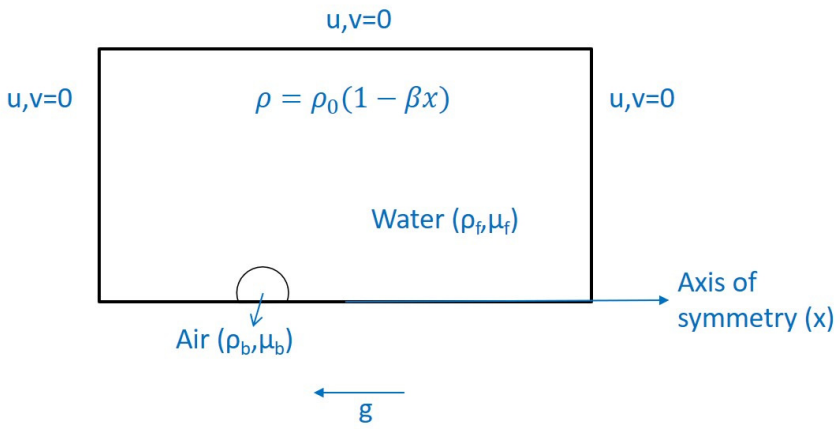

Figure 7.1. Schematic

from the base, but the bubble moves rectilinearly. However, in these cases, the bubble wake is no longer axisymmetric. We will thus explore the parameter space where the bubble motion is rectilinear.

We have a linear temperature stratification leading to a density stratification in the x direction. On the left wall the temperature perturbation, $T_m = 0$, on the right, $T_m = \frac{dT}{dx} L_x$ and on top, $T_m = \frac{dT}{dx} x$. All the walls have zero slip and are far from the bubble to mimic the flow in an infinite liquid. We will use $d/L = 40 \sim 80$, depending on the length of the domain needed to study the bubble wake. The initial location of the bubble is at $x = 2d_{\mathrm{i}}$ from the left wall and it rises from rest due to gravitational effects.

Similar to the previous studies we will solve the Navier-Stokes Equations along with the energy equation. In this study we will use a partial differential equation solver called Basilisk, which encompasses a numerical solver for two-phase flows using the Volume of fluid method. We parallelize this code to be run on the Purdue Research cluster. Along with the momentum equation we also implement the energy equation. Since we neglect phase change and compressibility, we use the advection and diffusion solvers in tandem to solve for the temperature. We also implement a jump condition for κ and ρC_p for the gas-liquid interface using the volume fraction, C. The Boussinesq approximation is done by simply adding a force term to the momentum equation, thus coupling the momentum and energy equations.

The density and viscosity ratios will be maintained at $\rho_l/\rho_b = 842$ and $\mu_l/\mu_b = 48.1$, respectively. These values correspond to the properties of air-water. The relevant non-dimensional parameters which we will consider in this study include Reynolds number, E*ö*tv*ö*s number, and Froude number.

7.3 Validation

This section will be devoted to validation of the code. This will be done in two parts; (a) the two-phase flow momentum solver in the absence of stratification (b) energy equation solver and Boussinesq approximation

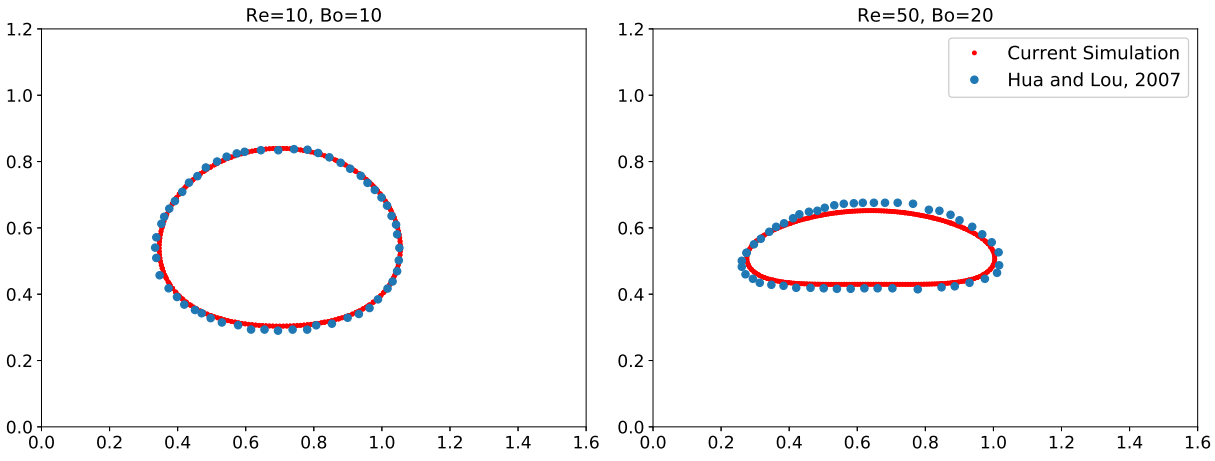

Figure 7.2. Bubble shape validation for (a) $Re = 10, Bo = 10$ (b) $Re = 50, Bo = 20$

7.3.1 Non-stratified flow

Table 7.1. Comparison of bubble aspect ratio and terminal velocity non-dimensionalized by $(gd)^{1/2}$ with results by [79]

Case	χ	χ_p	v^*	v_p^*
$Re = 100, Bo = 10$	3.197	3.19	0.873	0.92
$Re = 50, Bo = 20$	3.275	3.23	0.69	0.72
$Re = 10, Bo = 10$	1.322	1.34	0.51	0.52
$Re = 50, Bo = 1$	1.262	1.27	1.374	1.41

We validate the homogeneous case by comparing bubble shapes, aspect ratio and bubble terminal velocities for different cases with existing literature. Figure 7.2 shows the bubble shapes for $Re = 10, Bo = 10$ (figure 7.2a) and $Re = 50, Bo = 20$ (figure 7.2b), where Bo is the Bond number, $Bo = \frac{\rho_f g d^2}{\sigma}$. Comparison of the shape is made with the paper by Hua and Lou [65] and we find that both these cases visually show a very good match. In order to express this more quantitatively, a comparison with the results by Cano-Lozano et. al. [79] is shown in table 7.1. Here χ and v^* refer to the bubble aspect ratio and non-dimensionalized bubble terminal velocity, respectively. The subscript, p, refers to the results taken from [79]. We find that for the diverse cases

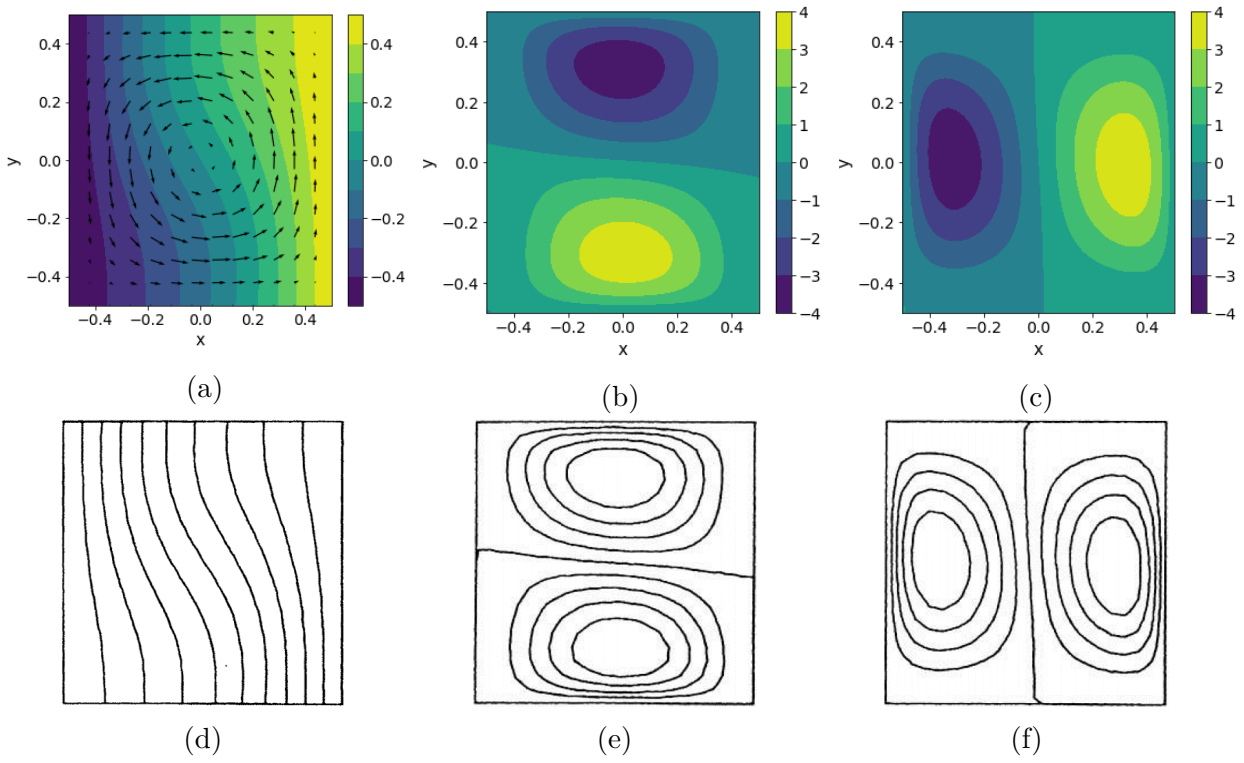

Figure 7.3. (a,d) Temperature (b,e) horizontal velocity (c,f) vertical velocity contours in a differentially heated cavity. (a,b,c) correspond to the present work (d,e,f) results from existing study [83]

that we considered, our results match very closely with the study by Cano-Lozano et al. [79].

7.3.2 Energy equation solver

In order to validate the energy solver, we consider the problem of a differentially heated square two-dimensional cavity with a Boussinesq fluid of Prandtl number $Pr = \nu/\mathcal{D} = 0.71$, where $\mathcal{D}$ is the thermal diffusivity. All the four boundaries have zero tangential and normal velocities. Top and bottom walls are insulated. Left wall is maintained at a $T = 0.5$ and the right wall at $T = -0.5$. We obtain the velocities and temperatures at steady state for a Rayleigh number of $Ra = \dfrac{\gamma \Delta T L^3 g}{\nu \mathcal{D}} = 1000$. We compare our results with the solution from de Vahl Davis [83] in figure 7.3.

The isotherms (figure 7.3a) and isocontours of velocity (figures 7.3b, c) show a good match qualitatively with the existing results in [83] (figures 7.3d-f). We also make a quantitative matching of the maximum horizontal (u_{max}) and vertical (v_{max}) velocity and the average Nusselt number on the vertical mid-plane, $Nu_{1/2} = \frac{q_{x=0}L}{T_h - T_c}$ (see table 7.2).

Table 7.2. Comparison of $Nu_{1/2}, v_{max}, u_{max}$ with results by [83]

	Current Simulation	**De Vahl Davis (1983) [83]**
$Nu_{1/2}$	1.289	1.118
u_{max}	3.669, y=0.82	3.649, y=0.813
v_{max}	3.719, x=0.18	3.697, x=0.178

7.4 Results and Discussion

The validated code is now used to study the transient motion of a single bubble in density-stratified fluids. The effect of stratification (in the range $9 < Fr < 50$, Reynolds number ($5 < Re < 124$) and Eötvös number ($1 < Eo < 20$) are presented.

7.4.1 Effect of Stratification

Stratification offers resistance to disturbance by rising bubbles and this can have a significant impact on the bubble dynamics

Bubble Wake

Thermal stratification leads to a density stratified background liquid which influences the bubble shapes, deformation and wake dynamics. The first phenomenon we will discuss here is the collapse of the standing vortex and generation of negative buoyant jet. Figure 7.4 shows the vorticity (top) and temperature (bottom) contours for a rising bubble at different Fr. We notice that as the stratification gets stronger, the standing vortex usually present in the rectilinear rise of bubble starts to collapse. The negative buoyant jet on the symmetry axis at the rear of the bubble is responsible for

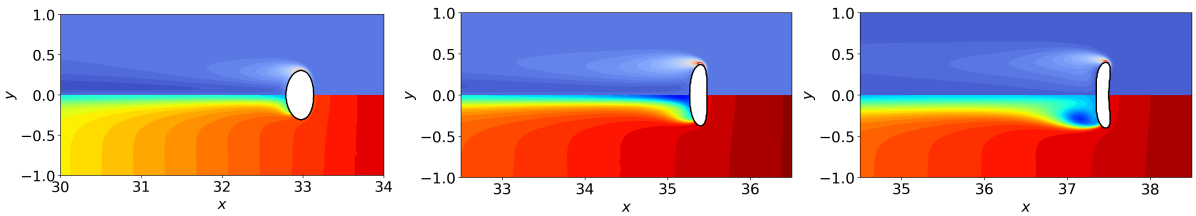

(a) (b) (c)

Figure 7.4. Vorticity and temperature contours for (a) $Fr = 9$ (b) $Fr = 15$ (c) $Fr = 25$

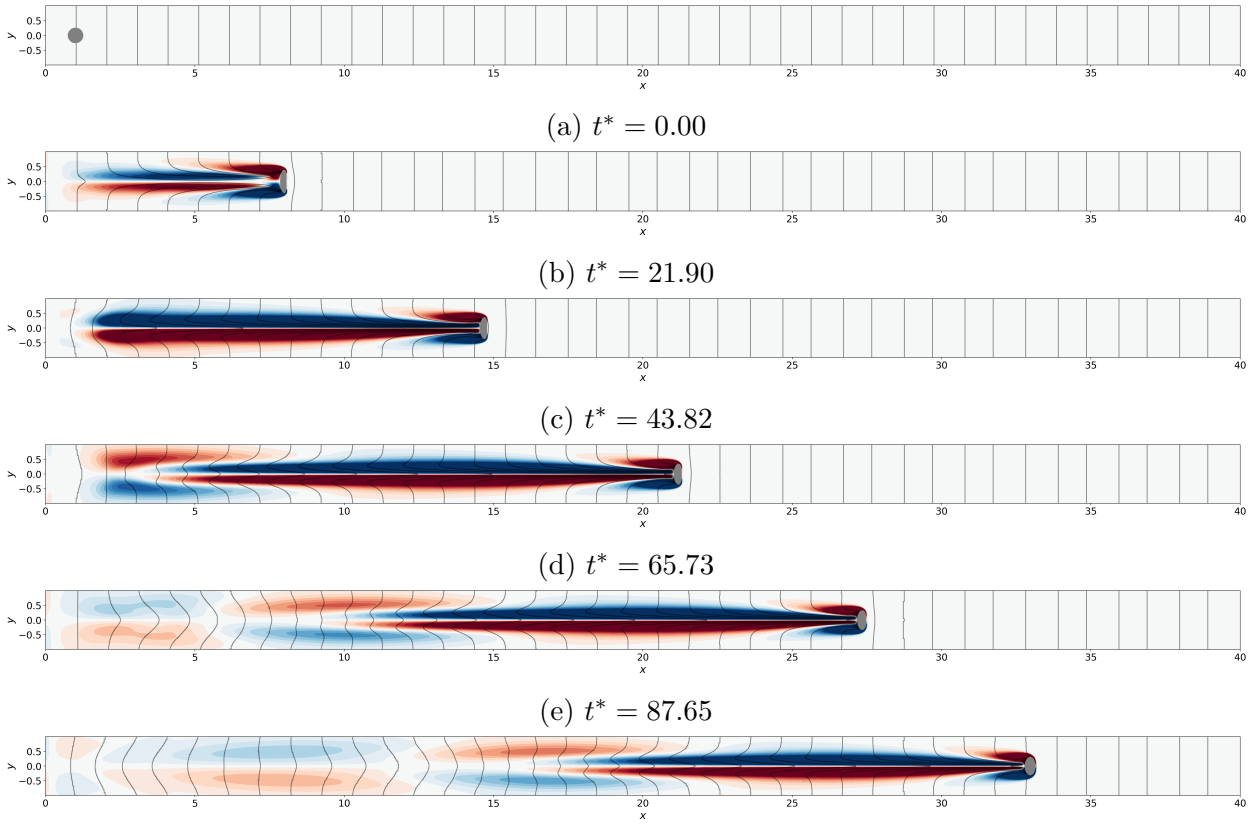

(a) $t^* = 0.00$

(b) $t^* = 21.90$

(c) $t^* = 43.82$

(d) $t^* = 65.73$

(e) $t^* = 87.65$

(f) $t^* = 109.57$

Figure 7.5. Time snapshots of vorticity plotted along with temperature streamlines for $Fr = 9$ at $Re = 124, Eo = 20$ where $t^* = t/(d^{1/2}/g^{1/2})$. The non-dimensional vorticity $\omega/(g^{1/2}d^{3/2})$ goes from -0.9 to 0.9

this behavior. The formation of the negative buoyant jet is explained as follows. As the bubble rises up, the isopycnals get disturbed. The displaced isopycnals experience a negative buoyancy force or a restorative force since they are in stable equilibrium. This force creates a velocity field pointing in the direction opposite to the motion of the bubble, thereby generating a rear buoyant jet. The rear buoyant jet is stronger for low Froude numbers, since the isopycnals experience stronger forces. Due to this, the stagnation point on the symmetry axis moves closer to the bubble rear for low Fr (figure 7.4). The separation point on the interface also moves towards the rear of the bubble as Fr is decreased. From the temperature contours (bottom half of figure 7.4) we see that the recirculation zone is most prominent for $Fr = 25$

The temperature isolines and vorticity contours during the passage of a single bubble through the density stratified liquid are plotted in figure 7.5. The displacement of the isopycnals due to entrainment by the bubble wake is depicted well in the figures. The restoration of the displaced isopycnals downstream of the bubble causes the buoyancy induced secondary vortex as seen, with the stagnation point located close to the bubble rear. The displaced isopycnals oscillate about their stable state before restoration to the original configuration. This behavior is also seen by observing the temperature isoline. For instance, at around $x = 5$ in figure 7.5e, the isotherms peak to the right in the positive x direction, while in figure 7.5f, they peak towards negative x, showing that the lines are oscillating.

The restoration of isopycnals causes a secondary vortex at the rear of the bubble. The evolution of this secondary vortex is depicted in figure 7.5a-f. The isopycnal tends to oscillate with a frequency proportional to the buoyancy frequency, N, before returning to its stable state. This induces not just a single secondary vortex, but multiple counter-rotating vortices in the rear of the bubble. In figure 7.5f, we see the original standing vortex, a secondary vortex behind it and more tertiary vortices which keep changing directions due to the oscillatory isopycnals.

The strength of negative jet increases as we increase the stratification. In figure 7.6a at $Fr = 9$, the velocity behind the bubble is oscillatory. At the same time instant, for $Fr = 25$, we only see one negative jet. The positive jet behind it is yet to form. This is because $Fr = 25$ has a lower buoyancy frequency or higher buoyancy time period of oscillation compared to $Fr = 9$. Thus, the isopycnals take longer to complete one cycle of oscillation. If we were to increase the domain size and let the bubble rise for longer, we expect to see tertiary vortices in the rear of the bubble for $Fr = 25$ as well.

The oscillatory nature of the density lines can be better explained by looking at the x velocity on the symmetry axis behind the bubble (figure 7.7a). For $Fr = 9$, the velocity oscillates about zero before dying down. Farther from the bubble rear, the amplitude of oscillation reduces, bringing the velocity closer to zero. The isopycnals farthest from the bubble have undergone multiple oscillations and are closer to coming back to their

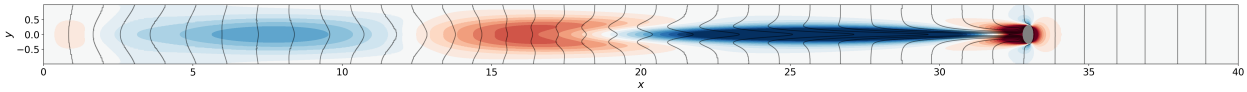

(a)

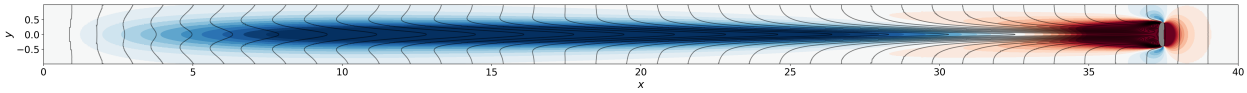

(b)

Figure 7.6. x velocity contours for $Re = 124, Eo = 20$ at (a)$Fr = 9$ (b) $Fr = 25$ at $t^* = 109.57$ with $u/(d^{1/2}g^{1/2})$ going from -0.18 to 0.18

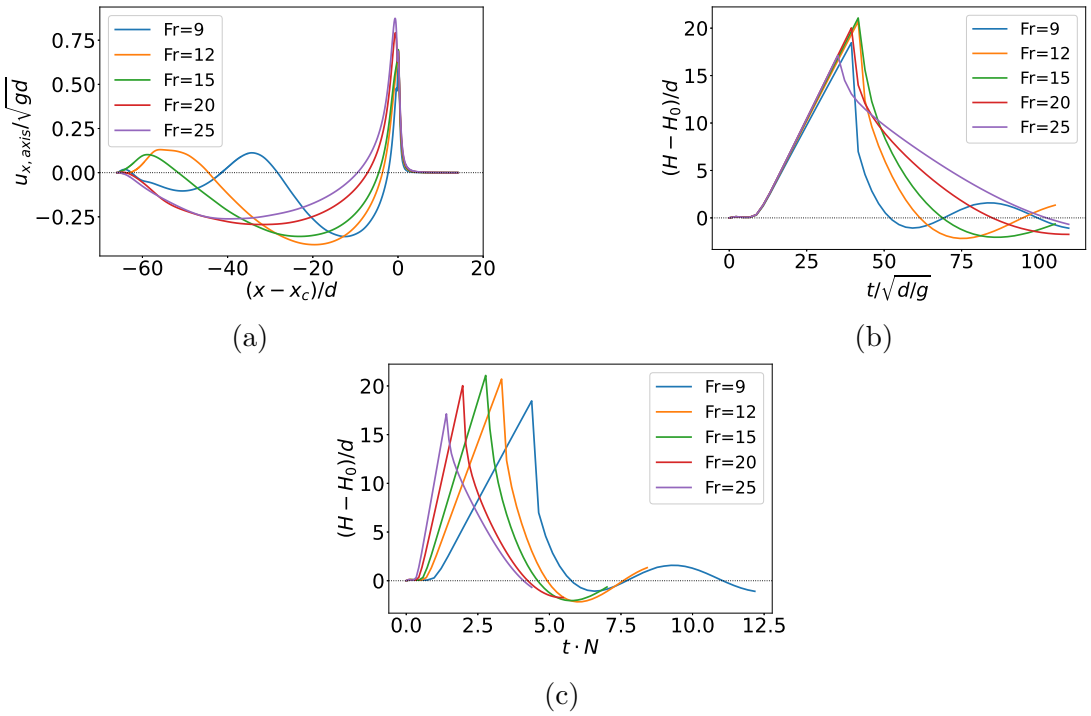

Figure 7.7. (a)Liquid velocity behind bubble on the axis (b,c) Height of isopycnal at $x/d = 4$ for $Re = 124, Eo = 20$

original configuration. As Fr increases, the frequency of oscillation increases. The restorative force weakens, thereby increasing the lengthscale of oscillation.

The height of one particular temperature isoline is plotted as a function of time for different Froude numbers (figure 7.7b). When time is normalized by a constant value for all Froude numbers, we see that the oscillation frequency reduces as Fr increases, with $Fr = 4$ having the highest number of cycles by the end of the simulation. We already know that this frequency is governed by the buoyancy frequency of the system. When time is thus normalized by $1/N$, we see that the isopycnal for all the Froude numbers collapse at the beginning of the oscillation cycles (figure 7.7c). This strengthens our proposition that the isopycnals in liquids of all stratification strengths will exhibit the oscillatory motion on a large enough timescale.

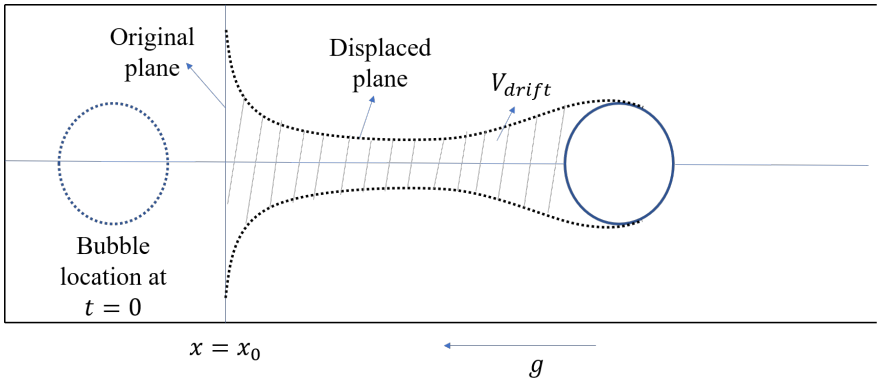

Figure 7.8. Illustration of partial drift volume

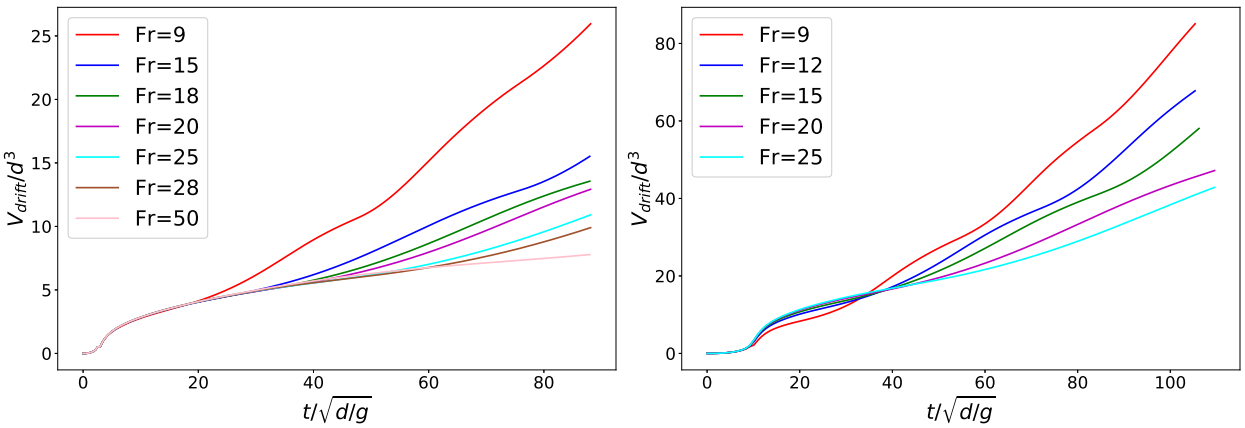

(a) (b)

Figure 7.9. Drift Volume for (a)$Eo = 5$, (b)$Eo = 20$

Drift Volume

When considering the deformation of a plane of marked fluid, drift volume is defined as the volume between the initial and final plane of marked fluid after the passage of any body, when the body is infinitely far from the initial plane [84]. A schematic defining the drift volume is shown in figure 7.8.

Drift volume can also be interpreted as the time integrated flux through a kinematic surface within the fluid domain. In order to calculate this, we pick a transverse surface $x = x_0$ (undisturbed isopycnal line) through which bubble has not yet passed. Volume flow rate through the surface can be calculated as $Q = \int u_f^+ dA$, where u_f^+ is the x velocity on the surface as a function of space and time. We take into account only

the positive liquid velocity, since reflux will involve negative velocity too. Through material balance, $\int_0^t Q dt$ will give the partial drift volume as a function of time.

When the drift volume stagnates with time, it means that there is no more positive velocity through the kinematic surface. The stagnation value is the total drift volume of the bubble. We calculate the partial drift volume for different Froude numbers at $Eo = 5$ and $Eo = 20$ (figure 7.9). For the lowest $Fr = 9$, we see that V_{drift} initially increases, stagnates and then starts to increase again, following an oscillatory pattern between stagnation and increase. The stagnation first happens when the isopycnals in the vicinity of the original plane start to experience negative buoyant force and fall back towards their stable state. In this time period, the velocity on the plane $x = x_0$ is mostly negative and thus positive drift stagnates. However, since the isopycnals oscillate before returning to their stable state, there is positive flow rate through $x = x_0$ once again when the second cycle of oscillation starts, leading to an increase in V_{drift}. This cycle continues periodically until the density lines close to $x = x_0$ are at rest. The value at the initial stagnation can be considered as the drift volume associated with the bubble.

For $Eo = 5$, the drift volume at first stagnation does not change much with Fr (figure 7.9a). For $Eo = 5$, we see that initially the drift increases with Fr (figure 7.9b). This is because dragging lighter fluid is easier, coupled with the fact that at low Fr the bubbles are more spherical due to high stratification strength leading to decreased drift. Beyond this initial phase, V_{drift} increases for lower Fr, since the tertiary jets behind the bubble are forming at a faster rate. For highest $Fr = 50$, the tertiary jets are not formed till the end of simulation and we do not see much increase in the drift volume beyond the initial stagnation.

Drag Estimation

Figures 7.10b,c show the transient evolution of rise velocity of bubbles for different stratification strengths. For nearly homogeneous liquid, the bubble velocity increases and reaches a constant steady state value. As Froude number decreases, the bubble

velocity is continuously changing. This happens due to the changing density levels and the heavier liquid dragged by the bubble. The bubble deformation also has a role to play in the changing rise velocity of the bubbles. The bubble deformation in this case is calculated as $\chi = d_y/d_x$, where d_y and d_x are the diameter of the bubble in the y and x direction, respectively (figure 7.10a). The bubble deformation reduces and bubble becomes more spherical as the bubble rises through stratified layers (figures 7.10d, e) and the reduction is more pronounced for strongly stratified liquids.

The rise velocity oscillates about a mean value for nearly homogeneous liquids, i.e, $Fr > 30$, (figure 7.10b), while the oscillations are absent for high levels of stratification. The velocity oscillations are an artifact of shape oscillations. The entire system is more stabilized at high Fr, due to the stabilizing buoyant force. This suppresses the shape oscillations of the bubble, in-turn leading to an absence of velocity oscillations.

Presence of stratification modifies the motion of particles, drops and bubbles. An important parameter to consider is the terminal velocity and drag experienced by the dispersed phase. A strong drag enhancement with an increase in stratification strength for $25 < Re < 100$ and $Fr \leq 200$ has been previously reported [6] for a sphere moving vertically in a stratified diffusive fluid. Rising particles and settling drops can even experience levitation when they cross a strong enough stratified layer [77], [78]. Drag enhancement was also reported for a rising drop in stratified fluids [5], where the normalized drag coefficient was shown to scale as $Fr^{-2.28}$.

Drag coefficient can be estimated by performing a simple force balance on the rising bubble. Some factors which need to be considered when calculating drag coefficient on a bubble in a stratified liquid are

- Changing bubble shape while passing through the stratified layers
- Changing buoyancy force
- Resulting non-constant terminal velocity
- Acceleration and added mass term in force balance

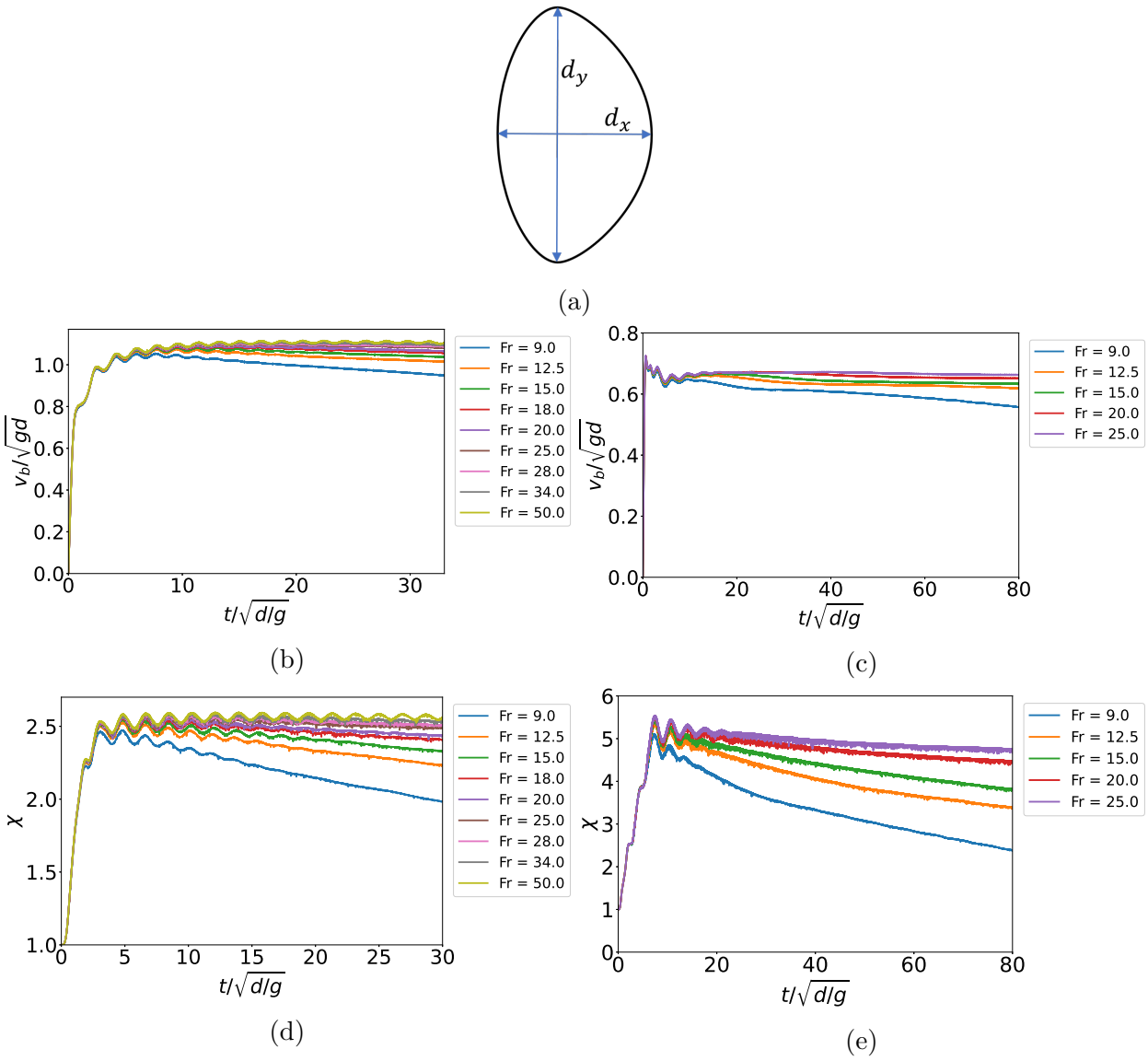

Figure 7.10. Bubble deformation definition(a). Rise velocity and bubble deformation for $Eo =$ (b,f) 5 (c,e) 20

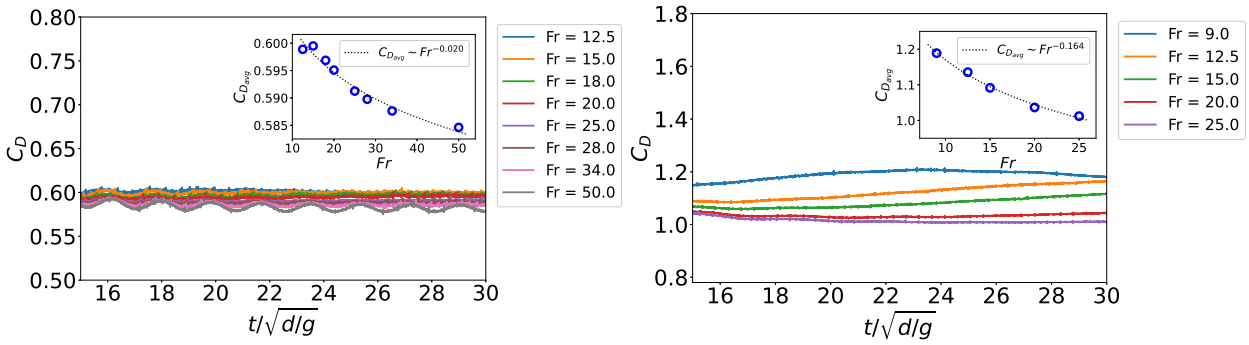

(a) (b)

Figure 7.11. Drag coefficient at $Re = 124$ for (a) $Eo = 5$,(b) $Eo = 20$.

Considering the above factors, the analytical expression for the drag coefficient can be derived as

$$C_D = \frac{2d_i^3}{3d_y(t)^2}\left(\frac{1-\gamma\frac{dT}{dx}x_b(t)}{\frac{1}{2}\rho_{l,0}v_b^2(t)}\right)\left((\rho_{l,0}-\rho_{b,0})g - \rho_{b,0}\frac{dv_b}{dt} - C_{AM}\rho_{l,0}\frac{dv_b}{dt}\right), \tag{7.1}$$

where the first term is the buoyancy term, the second is the bubble velocity acceleration and the third is the added mass term. Here, we calculate the buoyancy force based on the density of the liquid and bubble at the location of the center of mass of the bubble at any given time instant. At the location of center of mass of the bubble, $x_b(t)$, the liquid density is given by $\rho_l = \rho_{l,0}(1-\gamma\frac{dT}{dx}x_b(t))$. d_i is the initial bubble radius and the bubble volume is calculated based on this. The projected area perpendicular to the flow, on the other hand is calculated based on $d_y(t)$, which is the bubble diameter in the y direction (see figure 7.10a) or the axis perpendicular to the symmetry axis. $d_y(t)$ is constantly changing when the bubble shape changes as it rise up through the stratified liquid.

Drag coefficient based on the expression given by equation 7.1 is obtained for varying Fr, for $Eo = 5$ (figure 7.11a) and $Eo = 20$ (figure 7.11b). Since we account for changing buoyancy and bubble shape deformation, a constant C_D is obtained. For the lower Eo, drag enhancement for stratified fluids is less pronounced and we obtain a scaling of $C_D \sim Fr^{-0.02}$. Drag enhancement is more pronounced for $Eo = 20$, with a scaling of

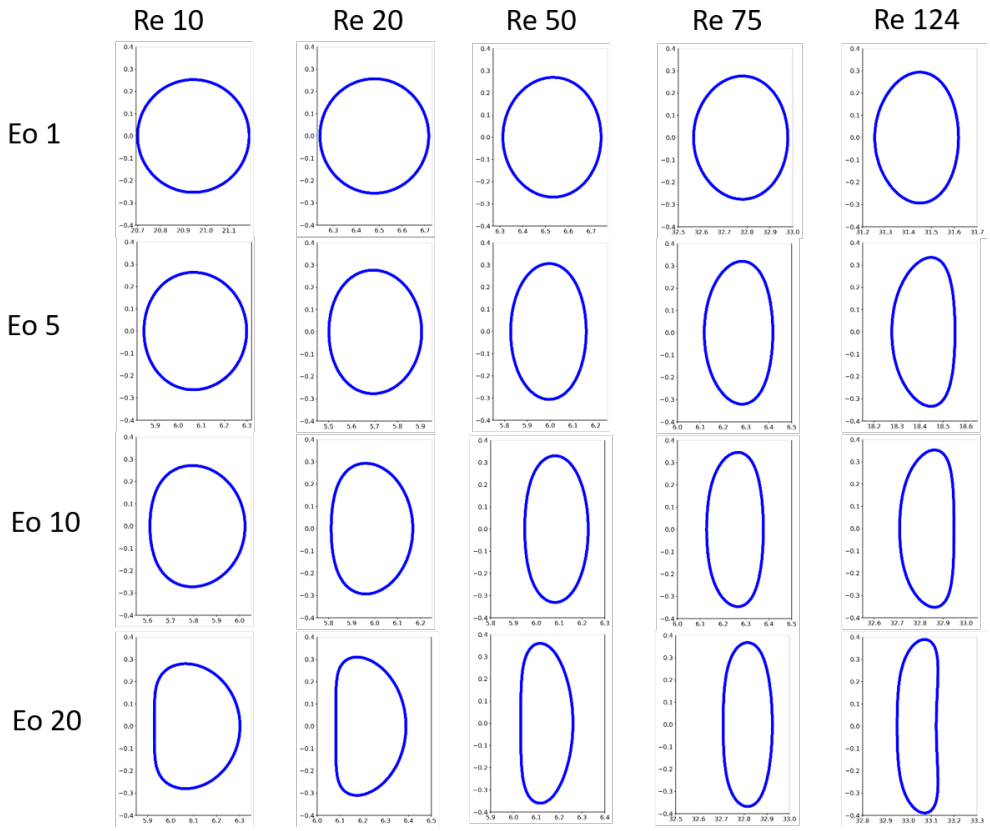

(a)

Figure 7.12. Bubble shapes at $Fr = 20$

$C_D \sim Fr^{-0.164}$. This can possibly be attributed to the bubble shape deformation. The bubble shape is much more sensitive to the stratification strength at $Eo = 20$ than at $Eo = 5$. For instance, at $t^* = t/\sqrt{d/g} = 30$, the percentage reduction in χ from $Fr = 20$ to $Fr = 12.5$ for $Eo = 5$ is approximately 8%, while for $Eo = 20$ it is 20%. Since we already accounted for changing buoyancy and shape, the drag enhancement obtained here is purely because of the heavier fluid being dragged by the bubble.

7.4.2 Effect of Reynolds and Eotvos numbers

Bubble Reynolds number and deformability play an important role in determining the rise velocity, drag coefficient and bubble wake dynamics. In our simulations we vary $Re = \rho_{l,0}\sqrt{gd}d/\mu_l$ between 5 and 124 and $Eo = (\rho_{l,0} - \rho_{b,0})gd^2/\sigma$ between 1 and

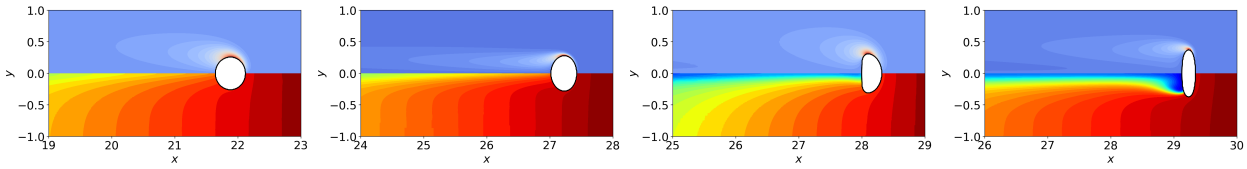

(a) (b) (c) (d)

Figure 7.13. Vorticity and temperature contours for Fr=20 (a,c) $Re = 20$ (b,d) $Re = 75$. The rows have same Eo, i.e, (a,b) $Eo = 1$ (c,d) $Eo = 20$

20. The bubble shapes for the various cases are shown in figure 7.12. An increase in Re and Eo lead to flattening of the bubble in the flow direction, giving it an oblate ellipsoid shape.

The bubble shapes become very important because they influence the bubble wake pattern, which subsequently affects the displacement and motion of the isopycnals. This becomes more clear by looking at the vorticity and temperature contours for $Re = 20, 75$ for two different $Eo = 1, 20$ (figure 7.13). The thermal and velocity boundary layer are thinner for the higher Re resulting in differences in the temperature pattern.The beginning of the formation of the negative jet can be observed for the higher Eo of 20 (figure 7.13c,d).

Rise velocity and Drag coefficient

The transient evolution of bubble rise velocity and bubble deformation is depicted for one particular *Eötvös* number to show that the system reaches a steady state (figure 7.14a,b). At the high Fr that we consider, the transient effects are minimal and a steady rise velocity is obtained for the different Reynolds numbers. It is also seen that the higher Reynolds numbers reach steady state faster, since the wake develops more slowly for lower Re. The bubble deformation is also drastically affected by Re (figure 7.14b).

Since the bubble reaches a steady state, we are able to plot the average deformation of the bubble for different Re and Eo ((figure 7.14c). An increase in Re produces an almost linear increase of χ. The dependence on Eo can also be interpreted from

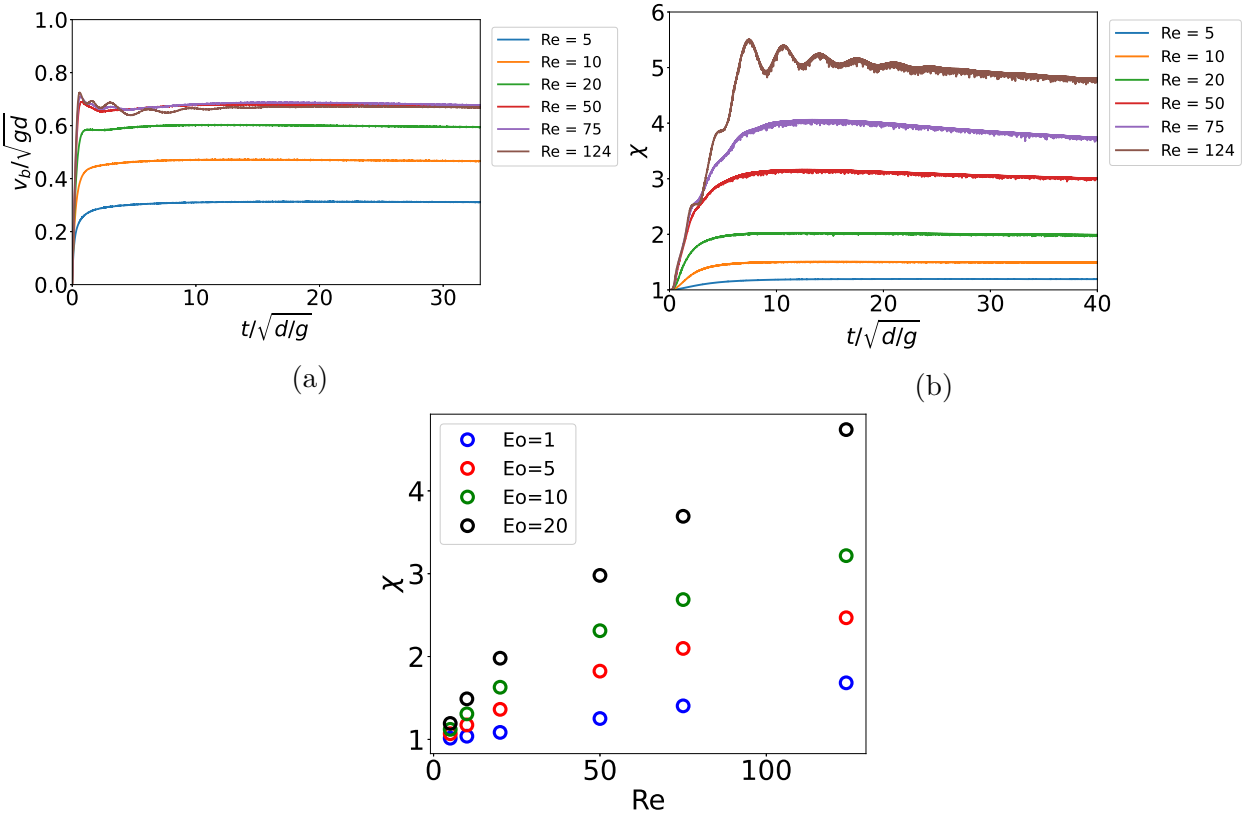

(a) (b)

(c)

Figure 7.14. (a)Rise velocity and (b) bubble deformation for $Fr = 20, Eo = 20$ as a function of Re. (c) Average bubble deformation

this plot. At low Re, an increase in Eo causes only a mild increase in the bubble deformation. However, as Re increases, the sensitivity of χ to Eo increases drastically.

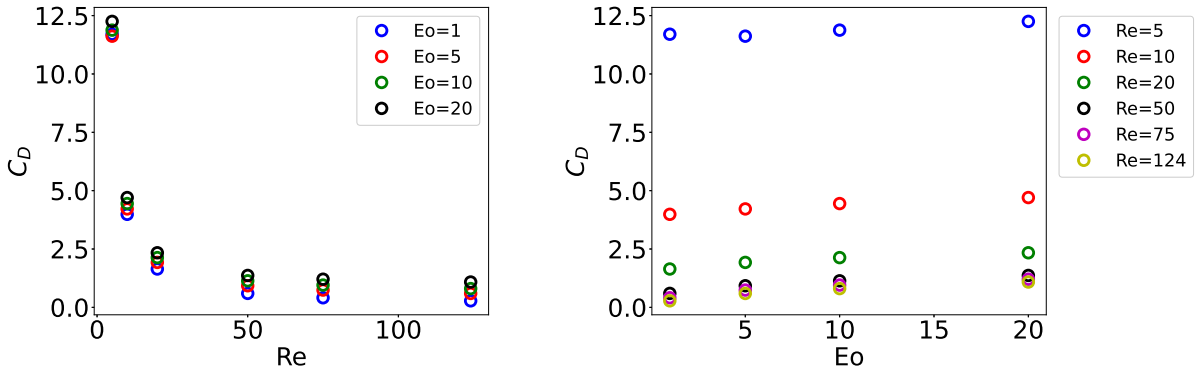

(a) (b)

Figure 7.15. Drag coefficient for $Fr = 20$ as a function of Eo and Re

Drag coefficient is calculated using equation 7.1. C_D reduces as Re increases (figure 7.15a). Viscous effects are dominating at low Re giving rise to a reduced rise velocity (figure 7.14a) and higher drag. The curves for different Eo almost collapse on top of each other.

Dependence of C_D on Eo is shown in figure 7.15b. We only see a very mild increase with Eo, especially pronounced at high Re. Had we used a constant project area to calculate the drag force, i.e, $F_D = C_D \frac{1}{2} \rho_{l,0} v_b^2(t) \pi \frac{d_i^2}{4}$, we would have ended up with a value of C_D which increases with Eo. Since we use a projected area which accounts for the shape change due to surface tension effects, $A_p = \pi \frac{d_y^2}{4}$, the drag coefficient we obtain does not change much with Eo. The driving factor for the changing drag force with a change in Eo, is the differences in bubble shapes at higher Eo which offers higher resistance to the flow.

Drift Volume

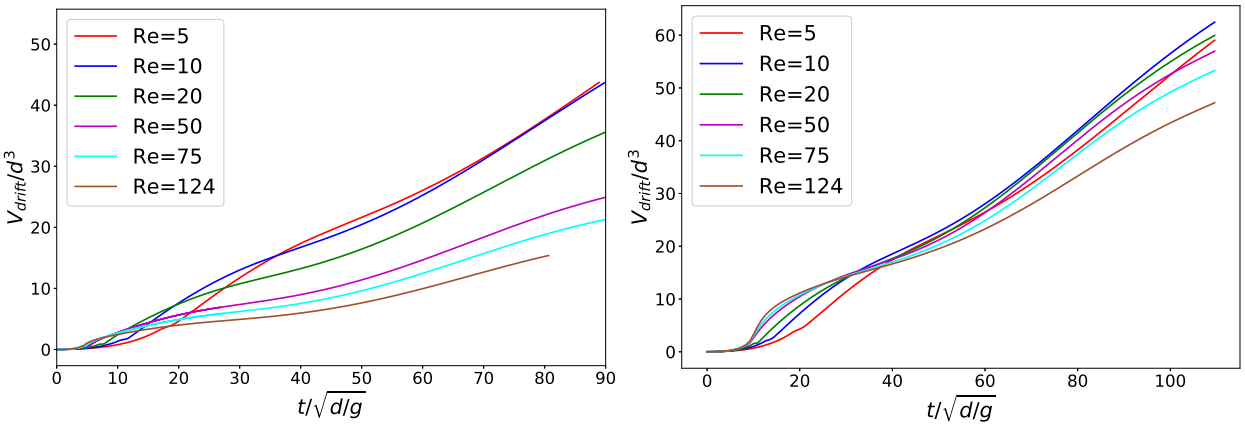

Figure 7.16. Drift Volume for $Fr = 20$ (a)$Eo = 1$, (b)$Eo = 20$ for varying Re

Drift of heavier fluid by the bubble depends on Reynolds number and bubble deformability as well. In order to explore these effects, we look at the drift volume as a function of Re and Eo (figure 7.16). Since the bubble moves slower at lower Re (figure 7.14a), it takes longer to cross $x = x_0$, because of which increase in V_{drift} happens later

for lower Re. Lower Re shows higher drift volume. Lower Reynolds number bubble has a larger boundary layer and wider wake leading to higher levels of entrainment. The higher viscous effects at low Re also leads to slower decay of the disturbance of the material plane. This results in the larger drift when integrated over time.

The increase in drift volume when the Eo is increased can be seen by comparing $Eo = 1$ and $Eo = 20$ in figures 7.16a,b, and comparing $Eo = 5$ and $Eo = 20$ in figures 7.9a,b. This happens because at larger Eo, the bubble is more flattened in the flow direction leading to a wider wake and larger entrainment. Similar trends for the drift volume for changing Re and Eo have been obtained for a cylindrical body migrating in a viscous fluid [85]. In the Stokes limit, the partial drift volume associated with a moving body becomes unbounded [86]. This happens because the flow decays very slowly in the far field, causing an infinite volume of fluid to be transported in the direction of motion of the body.

7.5 Partial Stratification

So far in this section, we have been discussing the study of a single bubble in linearly stratified fluids. In order to apply our results to the real world, for instance bubble rise in oceans and lakes, a few other factors have to be accounted for.

Typically, steep vertical temperature gradients are present only in parts of the lakes and reservoirs. The stratified layers are called metalimnion in which the temperature changes much more drastically with depth compared to the layers above or below. The stratification occurs in lakes usually in the summer season. The surface water or the epilimnion, heats up due to warmer atmospheric conditions and fails to mix with the colder, lower water layers or the hypolimnion. Water still does circulate within these regions, maintaining approximately uniform temperatures in this region, but does not mix between the regions. This creates the steep temperature gradient in the metalimnion. We will thus need to have a domain which reflects this. We will study the passage of the bubble through a medium where the bottom and top part of the domain remain non-stratified. A partial linear stratification, resembling the metalimnion will

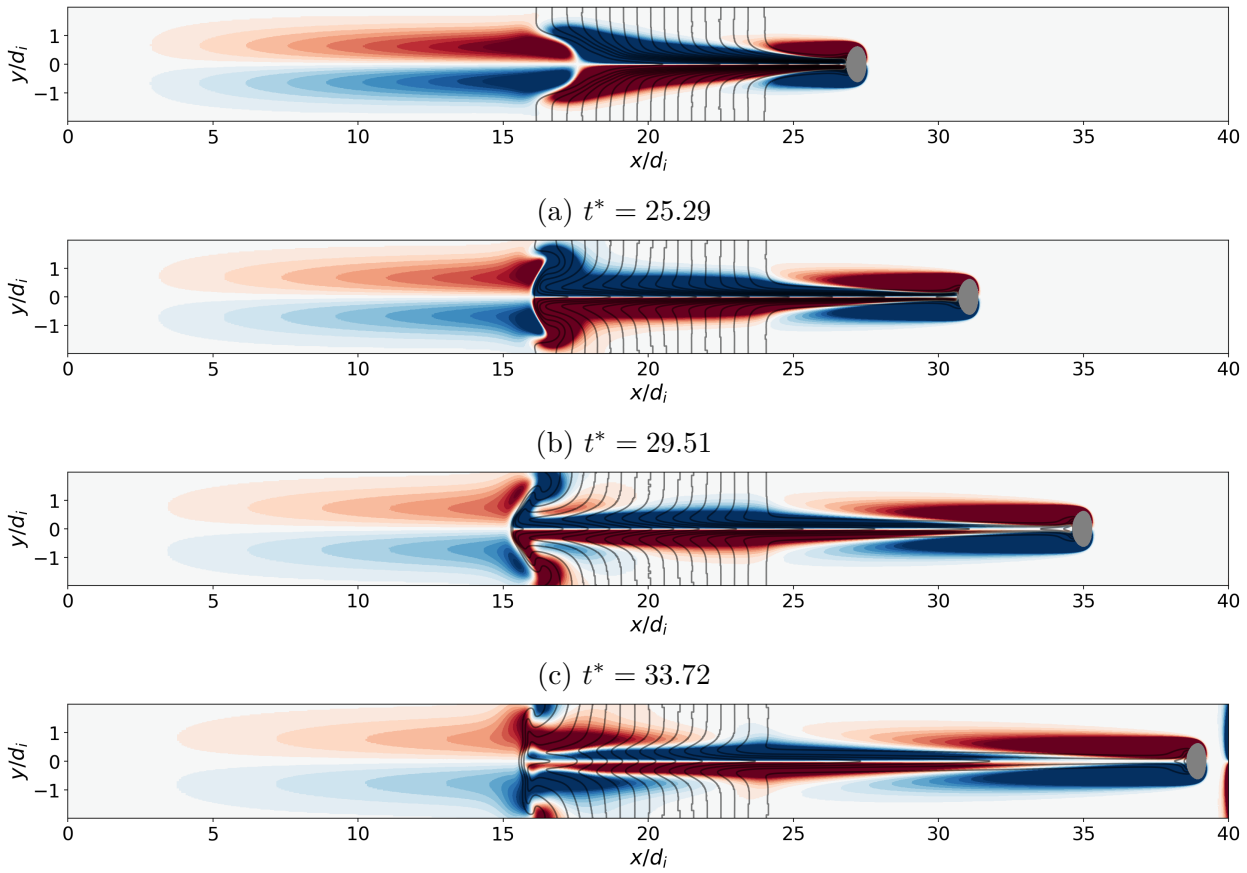

(a) $t^* = 25.29$

(b) $t^* = 29.51$

(c) $t^* = 33.72$

(d) $t^* = 37.94$

Figure 7.17. Time snapshots of vorticity contours and isotherms for partial stratification at $Fr = 4, Eo = 5, Re = 124$. The non-dimensional vorticity $\omega/(g^{1/2}d^{3/2})$ goes from -0.9 to 0.9

be initiated. We wish to study the transient evolution of the bubble dynamics as the bubble transitions from the homogeneous to stratified regions.

The temperature and vorticity patterns after the passage of a bubble through partially stratified medium is shown in figure 7.17. The domain length is $40d_{\mathrm{i}}$, with stratification present between $x = 16d_{\mathrm{i}}$ and $x = 24d_{\mathrm{i}}$. The length of stratification is $L_{strat} = 8d_{\mathrm{i}}$. Temperature profile in this region is given by $T = \dfrac{dT}{dx}x$. Below and above this region, the temperatures are constant at $T = 0$ and $T = \dfrac{dT}{dx}L_{strat}$, respectively.

At $t = 25.29d_{\mathrm{i}}$ (figure 7.17a), the bubble has passed through and exited the stratified portion of the liquid. It has the primary vortex followed by the negative buoyant jet in its wake. Since only part of the liquid is stratified, the negative jet is present only in

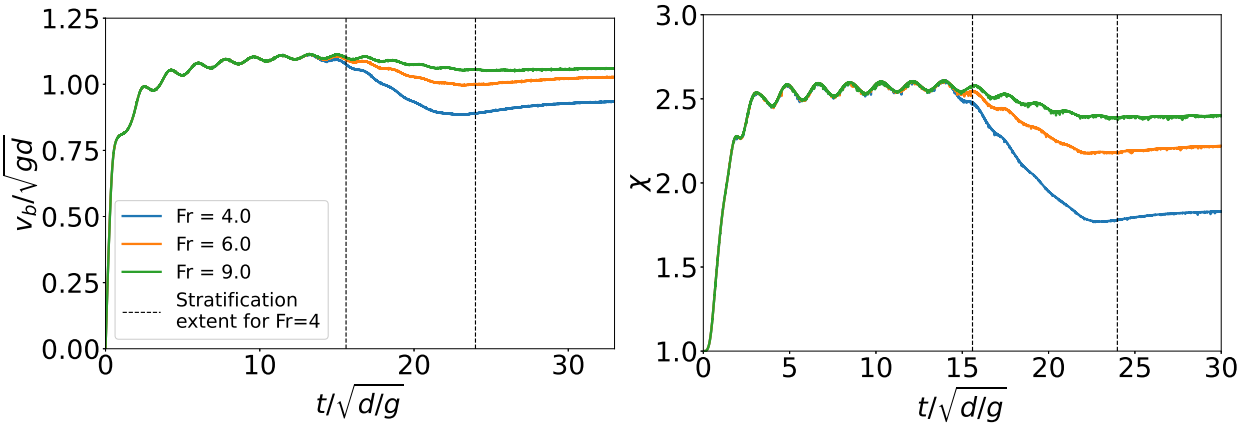

(a) (b)

Figure 7.18. (a)Rise velocity and (b) Bubble deformation for partial stratification at $Re = 124, Eo = 5$

the stratified region due to the negative buoyant force experienced by the isopycnals. Behind this region, the liquid is still homogeneous and the positive velocity in the liquid created by the bubble wake is still present. It is important to note, that unlike the previous cases where we had stratification throughout the domain, the positive jet behind the negative jet is not due to oscillatory isopycnals. It is the standing vortex created due to the bubble rising, which still has not dissipated in the homogeneous liquid (between $x = 0$ to $x = 16d_i$).

The positive and negative jets at the starting point of stratification interact, resulting in roll up (figures 7.17b,c). Simultaneously the vortices in the homogeneous part between $x = 0$ to $x = 16d_i$ starts slowly dissipating, since this portion is not influenced by the bubble anymore. Towards the end at $t^* = 37.94$ (figure 7.17d), the isopycnals in the stratified region starts to oscillate resulting the tertiary vortex behind the secondary vortex resulting in complex temperature and vorticity patterns at the beginning of the stratified layers.

It is worth noting that the wake of the bubble has been attenuated due to the secondary vortex (figure 7.17a) when the bubble passes through the stratification. However, when the bubble re-enters the non-stratified region, beyond $x = 24d_i$, the primary wake length once again increases, leading to increased drift (figures 7.17b-d).

The stagnation point also moves farther away from the rear of the bubble, when it moves from stratified to non-stratified layers.

Figure 7.18 shows the rise velocity and bubble deformation for varying Fr, where the background medium has stratification only in a portion of the domain. The black dotted lines here correspond to the times when the bubble enters and leave the stratified layers for the lowest Froude number of $Fr = 4$. The rise velocity reaches a steady state before entering the stratified layers, although it is oscillating due to shape instabilities. Once the bubble enters the stratified liquid, the rise velocity starts decreasing uniformly for all Froude numbers. Upon exit from the stratified liquid, the velocity increases mildly before coming to a steady state once again. The velocity and shape oscillations have also been suppressed due to the stratification. The reduction in the velocity of the bubble is a function of both the stratification strength and length of stratification L_{strat}.

We see that the bubble deformation also decreases when it is moving through the stratification and reaches back up to a constant value beyond this region (figure 7.18b). The final bubble deformation does not reach the initial deformation level and thus, the bubble velocity is also affected by the change in the bubble shape.

7.6 Summary

We perform direct numerical simulations of rising motion of a single bubble in stratified fluids using Basilisk and taking advantage of Adaptive Mesh Refinement. A temperature stratification in the domain gives rise to a stable density-stratified fluid. We discuss the bubble wake dynamics in detail and find the presence of secondary and tertiary vortices, which are alternating in direction, in the wake of the bubble due to the negative buoyant force experienced by the isopycnals. The other physical parameters we take into consideration include the bubble shapes, drift volumes and drag coefficient. Unlike in a homogeneous fluid, the drift volume keeps increasing and at low Froude numbers, it shows oscillations as it increases due to the oscillatory nature

of the bubble wake. The drag coefficient is estimated using a simple force balance on the bubble taking in to account the changing bubble shape and the buoyancy force.

We study the effect of stratification in the range $9 < Fr < 50$ and show that it has a significant role to play in the bubble dynamics. The strength of the negative buoyant jet increases for higher stratification. The frequency of oscillation of isopycnals also increases with stratification and scales with the buoyancy frequency, N. The bubble shape deformation is suppressed greatly as the bubble rises through sharp stratification. Drag coefficient is also likewise enhanced. We also explore the role of Reynolds and Eotvos numbers in the bubble rise in the range $5 < Re < 124$ and $1 < Eo < 20$. We record bubble shapes and deformations for different cases at $Fr = 20$. We observe enhanced C_D as Re is reduced. The increase of C_D with Eo is mild for low Re and is most pronounced at $Re = 124$. The drift volume increase with Eo is attributed to the bubble shape and resulting wake size. V_{drift} is inversely proportional to Re due to the slower decay of velocity in the far field.

Finally we also look at partial stratification, where we are able to observe the differences between homogeneous and stratified mediums. We see the development of complex vorticity patterns at the region between the homogeneous and stratified liquid, once the bubble has passed through. The stratified region also suppresses the rise velocity, the length of the bubble wake and the bubble deformation.

8. TOPOLOGICAL CHANGES

8.1 Free surface

Until now, we have been modeling the rise of bubbles in an infinite domain far away from boundaries. Typically, since we have the presence of stratification near the free surface, we will also have to consider the interaction between bubble and the free surface as the bubbles rise to the top. Free surface flows are in fact something we encounter everyday, right from drinking, washing and cooking to other major applications like breaking waves, boiling in nuclear plants and so on. When an air bubble bursts at an air-water interface, it gives rise to a liquid jet and surface waves [87], [88]. A lot of operations in ocean engineering require the consideration of free surface effect. VOF method has been used previously for simulating bubble interactions with the free surface [89]. We also have the advantage of using the adaptive meshing tool and can thus resolve the flow well. The use of VOF method also makes it easy to handle topological changes.

We simulate a bubble which rises from rest (initiated at $x = 2d_{\mathrm{i}}$ from the left wall) in a stratified fluid due to gravitational effects and meets the free surface. The domain length is $20d_{\mathrm{i}}$, with liquid height being $16d_{\mathrm{i}}$. The top $4d_{\mathrm{i}}$ is filled with gas phase with same properties as the bubble. The background liquid is stratified with a Froude number of 9. Re and Eo corresponding to the flow are 100 and 5, respectively. Time snapshots are shown in figure 8.1 with the top half showing the vorticity contours and the bottom half, the temperature. The free surface deforms before the bubble reaches it (figure 8.1a), raised in a hat shape. Once the bubble reaches the free surface, there is a small bounce back of the bubble (figures 8.1c-f) due to the strong surface tension force. Following this the upward bubble velocity overcomes the surface tension effects and the bubble merges with the free surface. This creates a vertical liquid jet as well as stray droplets in the air (figure 8.1i-k). The bubble bursting creates surface waves, which is apparent from the free surface level and vorticity contours in figures 8.1h-l. The bubble also entrains heavier liquid while rising up. Upon bursting, there is horizontal intrusion on the free surface, which causes the temperature at the free

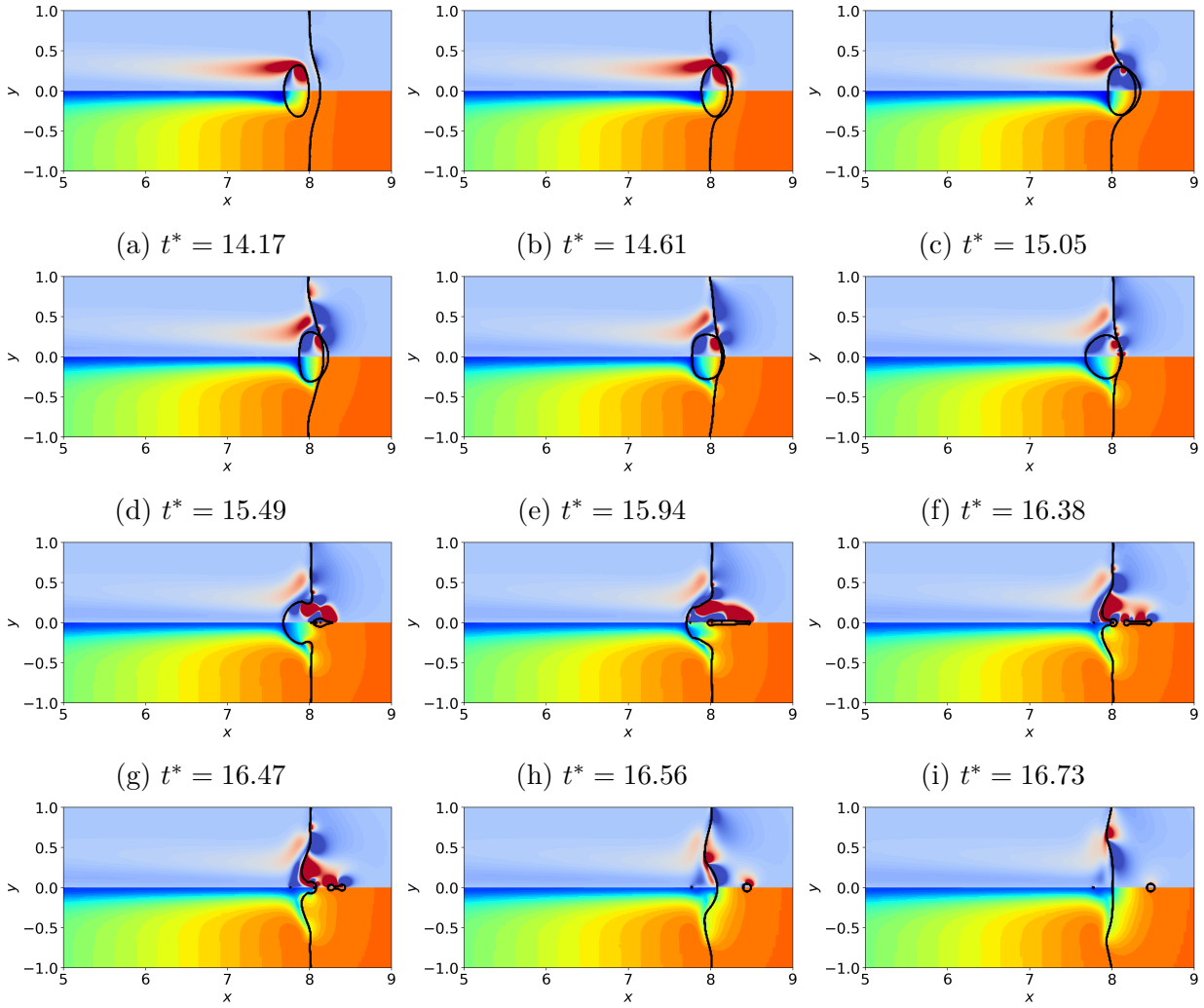

(a) $t^* = 14.17$ (b) $t^* = 14.61$ (c) $t^* = 15.05$

(d) $t^* = 15.49$ (e) $t^* = 15.94$ (f) $t^* = 16.38$

(g) $t^* = 16.47$ (h) $t^* = 16.56$ (i) $t^* = 16.73$

(j) $t^* = 16.82$ (k) $t^* = 17.27$ (l) $t^* = 17.71$

Figure 8.1. Bubble bursting at free surface at $Re = 100, Fr = 9, Eo = 5$. Top shows the vorticity contours ($\omega/(g^{1/2}d^{3/2}$ in the range -4.52 to 9.03) and the bottom shows the temperature contours

surface to reduce quite a bit (figure 8.1l). Bubbles rising up to the free surface can thus help in preserving freshwater by lowering surface temperatures and achieve liquid destratification, especially when plumes of bubbles rise up entraining large amounts of liquid.

8.1.1 Future Work

We performed preliminary simulation of a bubble rising in temperature stratified fluid and meeting the free surface. A more detailed analysis is necessary to understand the complex flow features involved in the bubble interaction with the free surface. The liquid jet, surface waves and droplet spray created when the bubble reaches the surface have important applications. For instance, sea spray is responsible for heat and moisture fluxes between the ocean and the atmosphere and plays a role in determining climate patterns and storm intensities.

We know that the study of a single bubble gives important insights into the dynamics of the bubble motion in the stratified fluid. In order to study large scale mixing effects by bubbles in lakes and oceans, considering the rise of a plume/swarm of bubbles up to the free surface is necessary. Multiple bubbles rising and bursting at the surface will lead to horizontal intrusions on the surface and create upper and lower re-circulation zones [90]. These effects are not always axisymmetric especially with multiple bubble and full 3D simulations will need to be developed

8.2 Bubble coalescence and breakup in stratified liquids

Another problem of interest is the coalescence and breakup of bubbles in stratified liquids. The previous studies based on a swarm of rising bubbles in stratified medium, do not account for topological changes. In reality, drops and bubbles have been reported to form clusters and the clustering is even enhanced in stratified flows. The possibility of coalescence is high in these cases. At high enough Reynolds ($\geq$ 200) and Eotvos numbers, there is also a possibility of bubble break up due to the high levels of bubble induced turbulence. Topological changes in bubbles have the potential to change the

liquid dynamics and is very much a real possibility while dealing with bubbly flow. On a fine enough grid, topology changes are naturally handled by methods which directly advect the interface, like the VOF method.

Multiple studies have been carried out on coalescence and breakup of bubbles in non-stratified liquids [68], [91], [92], [93]. Furthermore, it has been shown that drops rising in line tend to attract each other which in some cases may lead to coalescence [27]. In case of coalescence, the thin film between the two bubbles or drops is ruptured. This happens due to the short range attractive forces [94]. The collision of two drops has been classified into various categories which include bouncing collision, where drops separate after collision, coalescence collision, where they merge, separation collision, where the drops coalesce for a brief period after which they break up and shattering collision, where strong impact leads to formation of several smaller drops [95].

In this work we will briefly look at the in-line bubble coalescence in a homogeneous liquid and compare qualitatively with experimental results from literature. We look at the case where two bubbles are placed in-line or one behind the other. The trailing bubble moves into the wake of the leading bubble and is accelerated. It finally merges with the leading bubble. The whole process in this case is divided into a contact stage and a drainage stage as explained in Feng et. al. 2016 [96]. The two bubbles have the same diameter with an initial distance of $24mm$ between them. They are released in a quiescent liquid and have an $Eo = \rho_l g R^2/\sigma_l = 3.936$ and $Ga = \rho_l \sqrt{gR} R/\mu_l = 0.559$, where R is the initial bubble radius. These are the same values estimated [97] for the experiments conducted by Feng et. al. 2016 [96].

A comparison of time snapshots of the bubbles is shown in figure 8.2 with top row showing the results from Feng et. al. 2016 [96] and bottom row showing our simulations at the same time. Δt is the time difference between the first snapshot and subsequent snapshots of the experiment. In general we see a good match with the experimental results. The trailing bubble gets accelerated in the wake of the leading bubble. The time of merging is also captured reasonably well by the numerical simulations. The simulation presented here has been run on a very coarse grid with a maximum resolution

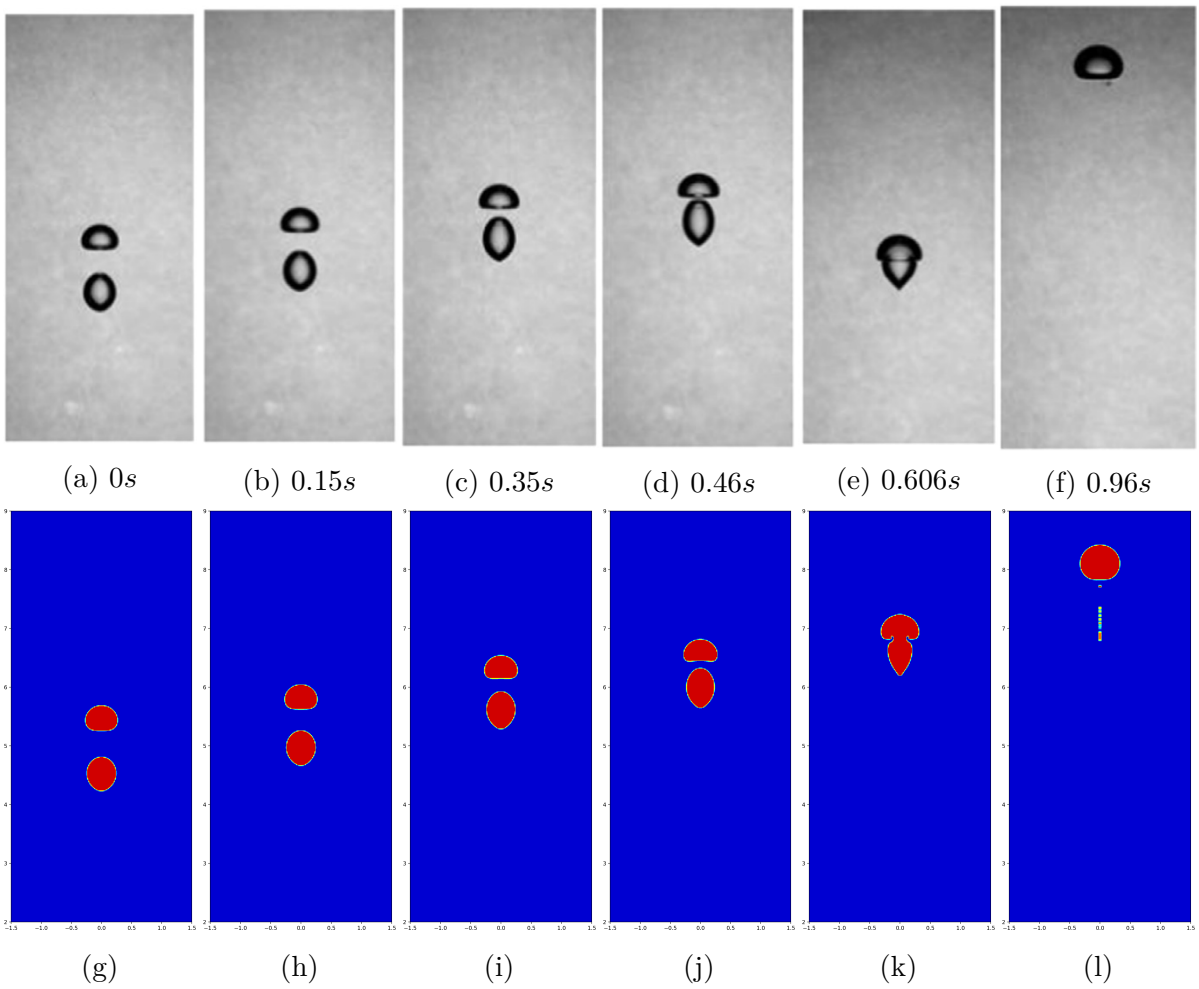

(a) $0s$ (b) $0.15s$ (c) $0.35s$ (d) $0.46s$ (e) $0.606s$ (f) $0.96s$

(g) (h) (i) (j) (k) (l)

Figure 8.2. In-line bubble coalescence (a)-(f) experiments by Feng et. al. 2016 [96]. (g)-(l) numerical simulations. The timestamps (Δt) for (g-l) are the same as (a-f)

of $1/2^6$. We believe that the spurious daughter bubbles below the coalesced bubble is an artefact of the coarse mesh and should go away with a finer mesh.

8.2.1 Future Work

We performed a preliminary simulation of in-line bubbles coalescing with each other in an axisymmetric domain and did a qualitative comparison with existing experimental work. A full 3D simulation is required to address coalescence of side by side bubbles and coalescence due to random collisions and bubble clustering in bubble swarms. In the future this work can also be extended to looking at the impact that enhanced clustering in stratified fluids has on bubble coalescence.

Documenting the range of parameters (Re, Eo, Fr) at which topological changes tend to occur is also an interesting and important problem. This will help understand at what range the simulations can avoid having to account for topological changes since we expect things to be different for stratified fluids. We also need to know how close the bubbles have to be for attractive forces to cause coalescence and how this range is different from the non-stratified case.

The breakup/coalescence is also prone to affect the liquid dynamics. We know that a polydisperse mixture of bubbles has different properties than a monodisperse swarm [91], [98]. We still need to understand how this changes in the context of stratified fluids.

Overall topological changes play an important role in addressing rise of bubbles in any stratified water body. Once the problems of bubble interaction with the free surface and the coalescence/breakup of bubbles are sufficiently addressed, the work we did on stratified bubbly flows could lead to ground-breaking revelations about real world destratification effects and bubble plume dynamics in ponds, lakes and even oceans.

9. CONCLUSIONS

Rising motion of bubbles through thermally or saline stratified liquids poses a challenging problem with important physical impacts. Rising bubbles lead to mixing of stratified fluids through two major mechanisms: (a) the pseudo-turbulence or liquid agitation which leads to thermal mixing (b) transport in bubble wake, which causes localized disturbances. Almost every known water body has some level of thermal/saline stratification and destratification methods become problems of interest.

We numerically investigate the mixing in stratified fluids by bubbles. A confined study of the rise of a swarm of bubbles in a Hele-Shaw cell with density-stratified fluids enables us to isolate the mixing effects produced primarily due to transport by the bubble wake. The zigzag motion of the bubbles results in the bubbles dragging heavier fluid up in their wake. Due to periodic vortex shedding in the bubble wake, the heavier fluid dragged by the bubble is deposited in the lighter layers, facilitating thermal mixing. We explore the void fraction - Froude number space and unravel their effects on background mixing

The rising of bubbles in unbounded fluids results in the production of liquid agitation and velocity fluctuations, which are primarily responsible for the mixing effects. On the other hand stratification also plays a major role in determining the bubble dynamics by enhancing clustering, suppressing vertical and horizontal velocities, reducing bubble dispersion and so on. We study effects of bubble density, stratification strength, bubble Reynolds number and bubble deformability on the background mixing. We find that the vertical buoyancy flux increases when we decrease the stratification due to lesser resistance to disturbance by the isopycnals. This allows for more time for thermal mixing. We see that increasing the number of bubbles in the domain has a similar effect. As we increase Eo, the energy input to the system is constant, but more of it goes into vertical mixing of the liquid than viscous dissipation. On the other hand, upon increasing Re, most of the extra energy input is dissipated leading to an almost constant mixing efficiency.

Following this, we study the rise of a single bubble in stratified fluids under various conditions, to better understand the bubble dynamics. The uniqueness of the bubble behavior in stratified as opposed to homogeneous fluids is presented by looking at the bubble wake, shapes, drift volumes and drag coefficient. A discussion on partial stratification, similar to thermal stratification in lakes, is done. Finally, we also briefly touch upon bubble topological changes by performing some preliminary simulations of a bubble bursting at the free surface and two in-line bubbles coalescing.

In conclusion, we have established the importance and role of bubble plumes in mixing stratified fluids and the effects of stratification on the bubble dynamics and interactions. We implemented two different kinds of interface-tracking (front-tracking and Volume of Fluid) methods depending on our needs and have successfully implemented computational fluid dynamics tools in studying multiphase flows.

REFERENCES

[1] T. Wilmarth and M. Ishii, "Two-phase flow regimes in narrow rectangular vertical and horizontal channels," *International Journal of Heat and Mass Transfer*, vol. 37, no. 12, pp. 1749–1758, 1994.

[2] P. Spicka, M. M. Dias, and J. C. B. Lopes, "Gas–liquid flow in a 2D column: Comparison between experimental data and CFD modelling," *Chemical Engineering Science*, vol. 56, no. 21-22, pp. 6367–6383, Nov. 2001. DOI: 10.1016/s0009-2509(01)00276-7. [Online]. Available: https://doi.org/10.1016/s0009-2509(01)00276-7.

[3] E. Bouche, V. Roig, F. Risso, and A. Billet, "Homogeneous swarm of high-Reynolds-number bubbles rising within a thin gap. part 2. liquid dynamics," *Journal of Fluid Mechanics*, vol. 758, pp. 508–521, Oct. 2014. DOI: 10.1017/jfm.2014.544. [Online]. Available: https://doi.org/10.1017/jfm.2014.544.

[4] A. Ardekani and R. Stocker, "Stratlets: Low reynolds number point-force solutions in a stratified fluid," *Physical review letters*, vol. 105, no. 8, p. 084 502, 2010.

[5] M. Bayareh, A. Doostmohammadi, S. Dabiri, and A. Ardekani, "On the rising motion of a drop in stratified fluids," *Physics of Fluids*, vol. 25, no. 10, p. 023 029, 2013.

[6] C. R. TORRES, H. HANAZAKI, J. OCHOA, J. Castillo, and M. Van Woert, "Flow past a sphere moving vertically in a stratified diffusive fluid," *Journal of Fluid Mechanics*, vol. 417, pp. 211–236, 2000.

[7] S. O. Unverdi and G. Tryggvason, "A front-tracking method for viscous, incompressible, multi-fluid flows," *Journal of Computational Physics*, vol. 100, no. 1, pp. 25–37, May 1992. DOI: 10.1016/0021-9991(92)90307-k. [Online]. Available: https://doi.org/10.1016/0021-9991(92)90307-k.

[8] G. Tryggvason, B. Bunner, A. Esmaeeli, D. Juric, N. Al-Rawahi, W. Tauber, J. Han, S. Nas, and Y.-J. Jan, "A front-tracking method for the computations of multiphase flow," *Journal of computational physics*, vol. 169, no. 2, pp. 708–759, 2001.

[9] A. J. Chorin, "Numerical solution of the Navier-Stokes equations," *Mathematics of Computation*, vol. 22, no. 104, pp. 745–745, 1968. DOI: 10.1090/s0025-5718-1968-0242392-2. [Online]. Available: https://doi.org/10.1090/s0025-5718-1968-0242392-2.

[10] R. D. Falgout and U. M. Yang, "Hypre: A library of high performance preconditioners," in *Computational Science — ICCS 2002*, P. M. A. Sloot, A. G. Hoekstra, C. J. K. Tan, and J. J. Dongarra, Eds., Berlin, Heidelberg: Springer Berlin Heidelberg, 2002, pp. 632–641, ISBN: 978-3-540-47789-1. DOI: 10.1007/3-540-47789-6_66.

[11] B. P. Leonard, "A stable and accurate convective modelling procedure based on quadratic upstream interpolation," *Computer Methods in Applied Mechanics and Engineering*, vol. 19, no. 1, pp. 59–98, Jun. 1979. DOI: 10.1016/0045-7825(79)90034-3. [Online]. Available: https://doi.org/10.1016/0045-7825(79)90034-3.

[12] C. S. Peskin, "Numerical analysis of blood flow in the heart," *Journal of computational physics*, vol. 25, no. 3, pp. 220–252, 1977.

[13] S. Popinet, "Gerris: A tree-based adaptive solver for the incompressible euler equations in complex geometries," *Journal of Computational Physics*, vol. 190, no. 2, pp. 572–600, 2003.

[14] E. Aulisa, S. Manservisi, R. Scardovelli, and S. Zaleski, "Interface reconstruction with least-squares fit and split advection in three-dimensional cartesian geometry," *Journal of Computational Physics*, vol. 225, no. 2, pp. 2301–2319, 2007.

[15] D. L. Youngs, "An interface tracking method for a 3d eulerian hydrodynamics code," *Atomic Weapons Research Establishment (AWRE) Technical Report*, vol. 44, no. 92, p. 35, 1984.

[16] J. Li, "Calcul d'interface affine par morceaux," *Comptes rendus de l'Académie des sciences. Série II, Mécanique, physique, chimie, astronomie*, vol. 320, no. 8, pp. 391–396, 1995.

[17] M. Ganesh, S. Kim, and S. Dabiri, "Induced mixing in stratified fluids by rising bubbles in a thin gap," *Physical Review Fluids*, vol. 5, no. 4, p. 043 601, 2020.

[18] E. Alméras, F. Risso, V. Roig, S. Cazin, C. Plais, and F. Augier, "Mixing by bubble-induced turbulence," *Journal of Fluid Mechanics*, vol. 776, pp. 458–474, Jul. 2015. DOI: 10.1017/jfm.2015.338. [Online]. Available: https://doi.org/10.1017/jfm.2015.338.

[19] E. Bouche, S. Cazin, V. Roig, and F. Risso, "Mixing in a swarm of bubbles rising in a confined cell measured by mean of PLIF with two different dyes," *Experiments in Fluids*, vol. 54, no. 6, Jun. 2013. DOI: 10.1007/s00348-013-1552-0. [Online]. Available: https://doi.org/10.1007/s00348-013-1552-0.

[20] J. W. M. Bush and I. Eames, "Fluid displacement by high Reynolds number bubble motion in a thin gap," *International Journal of Multiphase Flow*, vol. 24, no. 3, pp. 411–430, Apr. 1998. DOI: 10.1016/s0301-9322(97)00068-2. [Online]. Available: https://doi.org/10.1016/s0301-9322(97)00068-2.

[21] V. Roig, M. Roudet, F. Risso, and A. Billet, "Dynamics of a high-Reynolds-number bubble rising within a thin gap," *Journal of Fluid Mechanics*, vol. 707, pp. 444–466, Aug. 2012. DOI: 10.1017/jfm.2012.289. [Online]. Available: https://doi.org/10.1017/jfm.2012.289.

[22] X. Wang, B. Klaasen, J. Degrève, A. Mahulkar, G. Heynderickx, M. Reyniers, B. Blanpain, and F. Verhaeghe, "Volume-of-fluid simulations of bubble dynamics in a vertical Hele-Shaw cell," *Physics of Fluids*, vol. 28, no. 5, p. 053 304, May 2016. DOI: 10.1063/1.4948931. [Online]. Available: https://doi.org/10.1063/1.4948931.

[23] S. Dabiri and P. Bhuvankar, "Scaling law for bubbles rising near vertical walls," *Physics of Fluids*, vol. 28, no. 6, p. 062 101, Jun. 2016. DOI: 10.1063/1.4948464. [Online]. Available: https://doi.org/10.1063/1.4948464.

[24] E. Bouche, V. Roig, F. Risso, and A. Billet, "Homogeneous swarm of high-Reynolds-number bubbles rising within a thin gap. part 1. bubble dynamics," *Journal of Fluid Mechanics*, vol. 704, pp. 211–231, Jul. 2012. DOI: 10.1017/jfm.2012.233. [Online]. Available: https://doi.org/10.1017/jfm.2012.233.

[25] S. Dabiri, A. Doostmohammadi, M. Bayareh, and A. M. Ardekani, "Rising motion of a swarm of drops in a linearly stratified fluid," *International Journal of Multiphase Flow*, vol. 69, pp. 8–17, 2015.

[26] A. M. Ardekani, A. Doostmohammadi, and N. Desai, "Transport of particles, drops, and small organisms in density stratified fluids," *Physical Review Fluids*, vol. 2, no. 10, Oct. 2017. DOI: 10.1103/physrevfluids.2.100503. [Online]. Available: https://doi.org/10.1103/physrevfluids.2.100503.

[27] M. Bayareh, S. Dabiri, and A. M. Ardekani, "Interaction between two drops ascending in a linearly stratified fluid," *European Journal of Mechanics - B/Fluids*, vol. 60, pp. 127–136, 2016.

[28] M. Chen and S. Cardoso, "The mixing of liquids by a plume of low-Reynolds number bubbles," *Chemical Engineering Science*, vol. 55, pp. 2585–2594, 2000.

[29] L. Díaz-Damacillo, A. Ruiz-Angulo, and R. Zenit, "Drift by air bubbles crossing an interface of a stratified medium at moderate Reynolds number," *International Journal of Multiphase Flow*, vol. 85, pp. 258–266, Oct. 2016. DOI: 10.1016/j.ijmultiphaseflow.2016.06.015. [Online]. Available: https://doi.org/10.1016/j.ijmultiphaseflow.2016.06.015.

[30] W. D. Baines and A. M. Leitch, "Destruction of Stratification by Bubble Plume," *Journal of Hydraulic Engineering*, vol. 118, no. 4, pp. 559–577, Apr. 1992. DOI: 10.1061/(asce)0733-9429(1992)118:4(559). [Online]. Available: https://doi.org/10.1061/(asce)0733-9429(1992)118:4(559).

[31] I. E. L. Neto, S. S. S. Cardoso, and A. W. Woods, "On mixing a density interface by a bubble plume," *Journal of Fluid Mechanics*, vol. 802, Aug. 2016. DOI: 10.1017/jfm.2016.454. [Online]. Available: https://doi.org/10.1017/jfm.2016.454.

[32] F. Blanchette, "Mixing and convection driven by particles settling in temperature-stratified ambients," *International Journal of Heat and Mass Transfer*, vol. 56, no. 1-2, pp. 732–740, Jan. 2013. DOI: 10.1016/j.ijheatmasstransfer.2012.09.042. [Online]. Available: https://doi.org/10.1016/j.ijheatmasstransfer.2012.09.042.

[33] S. Wang and A. M. Ardekani, "Biogenic mixing induced by intermediate Reynolds number swimming in stratified fluids," *Scientific Reports*, vol. 5, no. 1, Dec. 2015. DOI: 10.1038/srep17448. [Online]. Available: https://doi.org/10.1038/srep17448.

[34] E. Kelley and M. Wu, "Path Instabilities of Rising Air Bubbles in a Hele-Shaw cell," *Physical Review Letters*, vol. 79, no. 7, pp. 1265–1268, Aug. 1997. DOI: 10.1103/physrevlett.79.1265. [Online]. Available: https://doi.org/10.1103/physrevlett.79.1265.

[35] C. J. Falconi, C. Lehrenfeld, H. Marschall, C. Meyer, R. Abiev, D. Bothe, A. Reusken, M. Schlüter, and M. Wörner, "Numerical and experimental analysis of local flow phenomena in laminar Taylor flow in a square mini-channel," *Physics of Fluids*, vol. 28, no. 1, p. 012109, Jan. 2016. DOI: 10.1063/1.4939498. [Online]. Available: https://doi.org/10.1063/1.4939498.

[36] G. Riboux, F. Risso, and D. Legendre, "Experimental characterization of the agitation generated by bubbles rising at high Reynolds number," *Journal of Fluid Mechanics*, vol. 643, p. 509, Dec. 2010. DOI: 10.1017/s0022112009992084. [Online]. Available: https://doi.org/10.1017/s0022112009992084.

[37] A. S. Sangani and A. K. Didwania, "Dynamic simulations of flows of bubbly liquids at large Reynolds numbers," *Journal of Fluid Mechanics*, vol. 250, no. -1, p. 307, May 1993. DOI: 10.1017/s0022112093001478. [Online]. Available: https://doi.org/10.1017/s0022112093001478.

[38] Y. Yurkovetsky and J. F. Brady, "Statistical mechanics of bubbly liquids," *Physics of Fluids*, vol. 8, no. 4, pp. 881–895, Apr. 1996. DOI: 10.1063/1.868869. [Online]. Available: https://doi.org/10.1063/1.868869.

[39] B. Bunner and G. Tryggvason, "Dynamics of homogeneous bubbly flows Part 1. Rise velocity and microstructure of the bubbles," *Journal of Fluid Mechanics*, vol. 466, Sep. 2002. DOI: 10.1017/s0022112002001179. [Online]. Available: https://doi.org/10.1017/s0022112002001179.

[40] B. Figueroa-Espinoza and R. Zenit, "Clustering in high Re monodispersed bubbly flows," *Physics of Fluids*, vol. 17, no. 9, p. 091 701, Sep. 2005. DOI: 10.1063/1.2055487. [Online]. Available: https://doi.org/10.1063/1.2055487.

[41] G. I. Taylor, "Diffusion by continuous movements," *Proceedings of the london mathematical society*, vol. 2, no. 1, pp. 196–212, 1922.

[42] X. Wang, B. Klaasen, J. Degrève, B. Blanpain, and F. Verhaeghe, "Experimental and numerical study of buoyancy-driven single bubble dynamics in a vertical Hele-Shaw cell," *Physics of Fluids*, vol. 26, no. 12, p. 123 303, Dec. 2014. DOI: 10.1063/1.4903488. [Online]. Available: https://doi.org/10.1063/1.4903488.

[43] T. R. Osborn, "Estimates of the Local Rate of Vertical Diffusion from Dissipation Measurements," *Journal of Physical Oceanography*, vol. 10, no. 1, pp. 83–89, Jan. 1980. DOI: 10.1175/1520-0485(1980)010<0083:eotlro>2.0.co;2. [Online]. Available: https://doi.org/10.1175/1520-0485(1980)010%3C0083:eotlro%3E2.0.co;2.

[44] T. R. Osborn and C. S. Cox, "Oceanic fine structure," *Geophysical Fluid Dynamics*, vol. 3, no. 1, pp. 321–345, Jan. 1972. DOI: 10.1080/03091927208236085. [Online]. Available: https://doi.org/10.1080/03091927208236085.

[45] M. C. Gregg, "Variations in the Intensity of Small-Scale Mixing in the Main Thermocline," *Journal of Physical Oceanography*, vol. 7, no. 3, pp. 436–454, May 1977. DOI: 10.1175/1520-0485(1977)007<0436:vitios>2.0.co;2. [Online]. Available: https://doi.org/10.1175/1520-0485(1977)007%3C0436:vitios%3E2.0.co;2.

[46] D. A. Briggs, J. H. Ferziger, J. R. Koseff, and S. G. Monismith, "Turbulent mixing in a shear-free stably stratified two-layer fluid," *Journal of Fluid Mechanics*, vol. 354, pp. 175–208, 1998.

[47] G. Ivey and J. Imberger, "On the nature of turbulence in a stratified fluid. part i: The energetics of mixing," *Journal of Physical Oceanography*, vol. 21, no. 5, pp. 650–658, 1991.

[48] L. H. Shih, J. R. Koseff, G. N. Ivey, and J. H. Ferziger, "Parameterization of turbulent fluxes and scales using homogeneous sheared stably stratified turbulence simulations," *Journal of Fluid Mechanics*, vol. 525, pp. 193–214, Feb. 2005. DOI: 10.1017/s0022112004002587. [Online]. Available: https://doi.org/10.1017/s0022112004002587.

[49] E. Alméras, F. Risso, V. Roig, C. Plais, and F. Augier, "Mixing mechanism in a two-dimensional bubble column," *Physical Review Fluids*, vol. 3, no. 7, p. 074 307, 2018.

[50] J. Moum and T. Osborn, "Mixing in the main thermocline," *Journal of physical oceanography*, vol. 16, no. 7, pp. 1250–1259, 1986.

[51] B. Bunner and G. Tryggvason, "Dynamics of homogeneous bubbly flows Part 2. Velocity fluctuations," *Journal of Fluid Mechanics*, vol. 466, Sep. 2002. DOI: 10.1017/s0022112002001180. [Online]. Available: https://doi.org/10.1017/s0022112002001180.

[52] J. Martínez-Mercado, C. A. Palacios-Morales, and R. Zenit, "Measurement of pseudoturbulence intensity in monodispersed bubbly liquids for 10< re< 500," *Physics of Fluids*, vol. 19, no. 10, p. 103 302, 2007.

[53] A. Esmaeeli and G. Tryggvason, "A direct numerical simulation study of the buoyant rise of bubbles at o (100) reynolds number," *Physics of Fluids*, vol. 17, no. 9, p. 093 303, 2005.

[54] B. Bunner and G. Tryggvason, "Effect of bubble deformation on the properties of bubbly flows," *Journal of Fluid Mechanics*, vol. 495, pp. 77–118, 2003.

[55] R. Zenit, D. L. Koch, and A. S. Sangani, "Measurements of the average properties of a suspension of bubbles rising in a vertical channel," *Journal of Fluid Mechanics*, vol. 429, pp. 307–342, 2001.

[56] P. D. Spelt and A. S. Sangani, "Properties and averaged equations for flows of bubbly liquids," *Applied scientific research*, vol. 58, no. 1-4, pp. 337–386, 1997.

[57] M. Lance and J. Bataille, "Turbulence in the liquid phase of a uniform bubbly air–water flow," *Journal of fluid mechanics*, vol. 222, pp. 95–118, 1991.

[58] G. Riboux, D. Legendre, and F. Risso, "A model of bubble-induced turbulence based on large-scale wake interactions," *Journal of Fluid Mechanics*, vol. 719, pp. 362–387, 2013.

[59] P. Smereka, "On the motion of bubbles in a periodic box," *Journal of Fluid Mechanics*, vol. 254, pp. 79–112, 1993.

[60] H. Schlichting and K. Gersten, *Boundary-layer theory*. Springer, 2016.

[61] M. Gregg, E. D'Asaro, J. Riley, and E. Kunze, "Mixing efficiency in the ocean," *Annual review of marine science*, vol. 10, pp. 443–473, 2018.

[62] S. A. Thorpe, *The turbulent ocean*. Cambridge University Press, 2005.

[63] D. Moore, "The velocity of rise of distorted gas bubbles in a liquid of small viscosity," *Journal of Fluid Mechanics*, vol. 23, no. 4, pp. 749–766, 1965.

[64] G. Ryskin and L. Leal, "Numerical solution of free-boundary problems in fluid mechanics. part 2. buoyancy-driven motion of a gas bubble through a quiescent liquid," *Journal of Fluid Mechanics*, vol. 148, pp. 19–35, 1984.

[65] J. Hua and J. Lou, "Numerical simulation of bubble rising in viscous liquid," *Journal of Computational Physics*, vol. 222, no. 2, pp. 769–795, 2007.

[66] M. K. Tripathi, K. C. Sahu, and R. Govindarajan, "Dynamics of an initially spherical bubble rising in quiescent liquid," *Nature communications*, vol. 6, no. 1, pp. 1–9, 2015.

[67] D. Qian, J. McLaughlin, K. Sankaranarayanan, S. Sundaresan, and K. Kontomaris, "Simulation of bubble breakup dynamics in homogeneous turbulence," *Chemical Engineering Communications*, vol. 193, no. 8, pp. 1038–1063, 2006.

[68] M. J. Prince and H. W. Blanch, "Bubble coalescence and break-up in air-sparged bubble columns," *AIChE journal*, vol. 36, no. 10, pp. 1485–1499, 1990.

[69] W. H. Snyder and J. Lumley, "Some measurements of particle velocity autocorrelation functions in a turbulent flow," *Journal of Fluid Mechanics*, vol. 48, no. 1, pp. 41–71, 1971.

[70] V. N. Prakash, J. M. Mercado, L. van Wijngaarden, E. Mancilla, Y. Tagawa, D. Lohse, and C. Sun, "Energy spectra in turbulent bubbly flows," *Journal of fluid mechanics*, vol. 791, pp. 174–190, 2016.

[71] I. Roghair, J. M. Mercado, M. V. S. Annaland, H. Kuipers, C. Sun, and D. Lohse, "Energy spectra and bubble velocity distributions in pseudo-turbulence: Numerical simulations vs. experiments," *International journal of multiphase flow*, vol. 37, no. 9, pp. 1093–1098, 2011.

[72] J. M. Mercado, D. C. Gomez, D. Van Gils, C. Sun, and D. Lohse, "On bubble clustering and energy spectra in pseudo-turbulence," *Journal of fluid mechanics*, vol. 650, pp. 287–306, 2010.

[73] K. Y. Yick, C. R. Torres, T. Peacock, and R. Stocker, "Enhanced drag of a sphere settling in a stratified fluid at small reynolds numbers," 2009.

[74] A. Srdić-Mitrović, N. Mohamed, and H. Fernando, "Gravitational settling of particles through density interfaces," *Journal of Fluid Mechanics*, vol. 381, pp. 175–198, 1999.

[75] H. Hanazaki, K. Kashimoto, and T. Okamura, "Jets generated by a sphere moving vertically in a stratified fluid," *Journal of fluid mechanics*, vol. 638, p. 173, 2009.

[76] A. Doostmohammadi, S. Dabiri, and A. M. Ardekani, "A numerical study of the dynamics of a particle settling at moderate reynolds numbers in a linearly stratified fluid," *Journal of Fluid Mechanics*, vol. 750, p. 5, 2014.

[77] N. Abaid, D. Adalsteinsson, A. Agyapong, and R. M. McLaughlin, "An internal splash: Levitation of falling spheres in stratified fluids," *Physics of Fluids*, vol. 16, no. 5, pp. 1567–1580, 2004.

[78] F. Blanchette and A. M. Shapiro, "Drops settling in sharp stratification with and without marangoni effects," *Physics of Fluids*, vol. 24, no. 4, p. 042 104, 2012.

[79] J. Cano-Lozano, P. Bohorquez, and C. Martínez-Bazán, "Wake instability of a fixed axisymmetric bubble of realistic shape," *International journal of multiphase flow*, vol. 51, pp. 11–21, 2013.

[80] R. A. Hartunian and W. Sears, "On the instability of small gas bubbles moving uniformly in various liquids," *Journal of Fluid Mechanics*, vol. 3, no. 1, pp. 27–47, 1957.

[81] J. Grace, "Shapes and velocities of bubbles rising in infinite liquid," *Transactions of the Institution of Chemical Engineers*, vol. 51, pp. 116–120, 1973.

[82] D. Bhaga and M. Weber, "Bubbles in viscous liquids: Shapes, wakes and velocities," *Journal of fluid Mechanics*, vol. 105, pp. 61–85, 1981.

[83] G. de Vahl Davis, "Natural convection of air in a square cavity: A bench mark numerical solution," *International Journal for numerical methods in fluids*, vol. 3, no. 3, pp. 249–264, 1983.

[84] I. Eames, S. Belcher, and J. Hunt, "Drift, partial drift and darwin's proposition," *Journal of Fluid Mechanics*, vol. 275, pp. 201–223, 1994.

[85] K. Katija and J. O. Dabiri, "A viscosity-enhanced mechanism for biogenic ocean mixing," *Nature*, vol. 460, no. 7255, pp. 624–626, 2009.

[86] I. Eames, D. Gobby, and S. Dalziel, "Fluid displacement by stokes flow past a spherical droplet," *J Fluid Mech*, vol. 485, pp. 67–85, 2003.

[87] J. Boulton-Stone and J. Blake, "Gas bubbles bursting at a free surface," *Journal of Fluid Mechanics*, vol. 254, pp. 437–466, 1993.

[88] L. Duchemin, S. Popinet, C. Josserand, and S. Zaleski, "Jet formation in bubbles bursting at a free surface," *Physics of fluids*, vol. 14, no. 9, pp. 3000–3008, 2002.

[89] Y. Zhao, H. H. Tan, and B. Zhang, "A high-resolution characteristics-based implicit dual time-stepping vof method for free surface flow simulation on unstructured grids," *Journal of Computational Physics*, vol. 183, no. 1, pp. 233–273, 2002.

[90] B. Sherman, *Scoping options for mitigating cold water discharges from dams*. CSIRO Land and Water Canberra, 2000.

[91] P. Chen, M. Duduković, and J. Sanyal, "Three-dimensional simulation of bubble column flows with bubble coalescence and breakup," *AIChE journal*, vol. 51, no. 3, pp. 696–712, 2005.

[92] E. Olmos, C. Gentric, C. Vial, G. Wild, and N. Midoux, "Numerical simulation of multiphase flow in bubble column reactors. influence of bubble coalescence and breakup," *Chemical engineering science*, vol. 56, no. 21-22, pp. 6359–6365, 2001.

[93] T. Otake, S. Tone, K. Nakao, and Y. Mitsuhashi, "Coalescence and breakup of bubbles in liquids," *Chemical Engineering Science*, vol. 32, no. 4, pp. 377–383, 1977.

[94] G. Tryggvason, R. Scardovelli, and S. Zaleski, *Direct numerical simulations of gas–liquid multiphase flows*. Cambridge University Press, 2011.

[95] M. Nobari and G. Tryggvason, "Numerical simulations of three-dimensional drop collisions," *AIAA journal*, vol. 34, no. 4, pp. 750–755, 1996.

[96] J. Feng, X. Li, Y. Bao, Z. Cai, and Z. Gao, "Coalescence and conjunction of two in-line bubbles at low reynolds numbers," *Chemical Engineering Science*, vol. 141, pp. 261–270, 2016.

[97] Y. Gui, C. Shan, J. Zhao, and J. Wu, "Wall effect on interaction and coalescence of two bubbles in a vertical tube," *AIP Advances*, vol. 10, no. 10, p. 105 210, 2020.

[98] J. Van Baten and R. Krishna, "Eulerian simulations for determination of the axial dispersion of liquid and gas phases in bubble columns operating in the churn-turbulent regime," *Chemical Engineering Science*, vol. 56, no. 2, pp. 503–512, 2001.

A. CONVERGENCE TESTS

Grid convergence tests are performed for the front tracking code in FORTRAN and the volume of fluid code in Basilisk (C) to find the optimal grid.

A.1 3D simulations using front tracking method

The grid independence is tested by simulating the rise of a single bubble in a 3D domain of size $10d \times 5d \times 5d$ at $Re = 74$, $Eo = 3.3$ and $Fr = 14.1$. The total number of points in the domain are varied between $\sim 6.5 \times 10^4$ and $\sim 3.3 \times 10^7$. The bubble rise velocity averaged in time is plotted in figure A.1a. We note that grid convergence is achieved for $\sim 4.19 \times 10^6$ points which corresponds to 25.6 points across the diameter of the bubble.

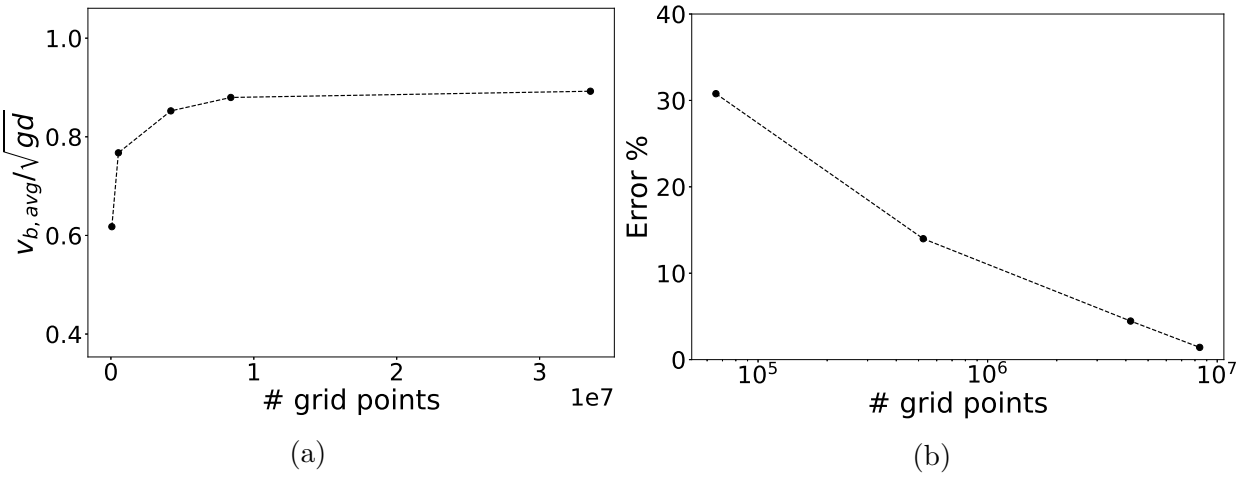

(a) (b)

Figure A.1. (a) Average bubble velocity for different number of grid points. (b) Error percentage for each grid resolution from the finest grid

The error percentage from the finest grid is also plotted for each of the other four cases on a semi-log plot in figure A.1b. The error for the grid that we use is about 4%, which is acceptable. For the highest Re of 200, we use the finest grid by doubling the grid points in each direction, with 51.2 points across the bubble diameter. This is done to ensure that the thermal and momentum boundary layers are appropriately resolved.

A.2 Axisymmetric simulations using volume of fluid method

The rise of a single bubble in an axisymmetric domain at $Re = 124$, $Eo = 5$ and $Fr = 12.5$ are tested on three different mesh sizes. Since we use an adapted grid, we modify the smallest grid size to test the grid independence, while keeping the largest grid size to be $\Delta x_{max} = 2d(20/2^8)$. The rise velocities are shown in figure A.2. They are almost co-incident on each other and we use the grid $\Delta x_{min} = 2d(20/2^{12})$ for all our calculations, after confirming that the thermal and momentum boundary layers are resolved with close to 16 points.

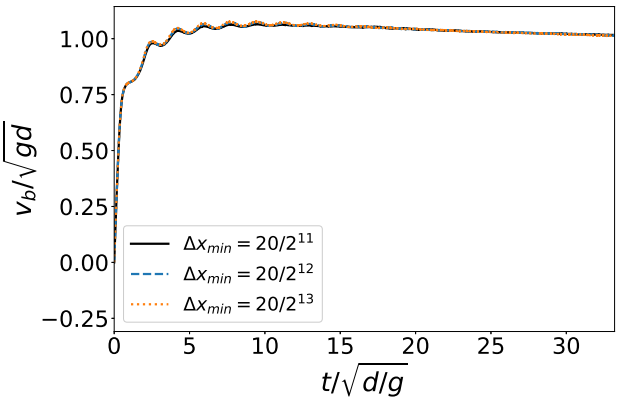

(a)

Figure A.2. Temporal bubble rise velocity for different mesh sizes

VITA

Education

- PhD in Mechanical Engineering Purdue University August 2017-May 2021
- B.Tech in Naval Arch and Ocean Engineering Indian Institute of Technology Madras August 2013 - July 2017

Awards

- *Travel Grant*, University of Maryland, 2017
- *Andrews Fellowship Recipient*, Purdue University, 2017
- *Academic Excellence: American Bureau of Shipping Prize*, IIT Madras, 2017
- *Class NK-100 Award best bachelor's thesis project*, IIT Madras, 2017
- *Summer Research Scholarship*, University of Melbourne, 2016
- *Academic Excellence: Sri Latha Sampath Srinath Prize*, IIT Madras, 2015

Journal Publications

- **Ganesh, M.** and Dabiri, S. (2021). Transient bubble dynamics in stably stratified fluids. *Under preparation*
- **Ganesh, M.**, Ardekani, A.M, and Dabiri, S. (2021). Characterization of cavitation onset in accelerated liquids. *Under preparation*
- **Ganesh, M.** and Dabiri, S. (2020). Numerical study of bubble induced mixing and pseudo-turbulence in stratified fluids. *International Journal of Multiphase Flow. Under Review*
- **Ganesh, M.**, Kim, S., and Dabiri, S. (2020). Induced mixing in stratified fluids by rising bubbles in a thin gap. *Physical Review Fluids, 5(4), 043601.*

Conference Publications and Presentations

- **Ganesh, M.**, Ardekani, A.M., and Dabiri, S. Cavitation modeling in liquids subject to large accelerations. *Proceedings of the 11th International Symposium on Cavitation (CAV2021). Accepted*
- **Ganesh, M.** and Dabiri, S. (2020). Bubble induced destratification in unconfined fluids. *73rd Annual Meeting of the APS Division of Fluid Dynamics (APS DFD 2020), Nov 22-24, 2020*
- **Ganesh, M.** Kim, S. K., and Dabiri, S. (2019). Bubble induced mixing in stratified fluids within a confined domain. *72nd Annual Meeting of the APS Division of Fluid Dynamics (APS DFD 2019), Nov 23-26, 2019, Seattle, WA, USA.*
- **Ganesh, M.** and Dabiri, S. (2019) Poster: Induced mixing in stratified fluids by rising bubbles *The Burgers Program Summer Research School on Fluid Dynamics, University of Maryland, College Park*

Teaching Experience

- ME 274 *Basic Mechanics II* - Spring 2020
- ABE 450 *Finite Element Methods in Design and Optimization* - Fall 2018
- Women in Engineering Program Outreach Activity - July 2018